UNIVERSITY OF BIRMINGHAM

Large Eddy Simulation of Turbulent Dispersed Multi-phase Flows for Engineering Applications - Development of Eulerian-Lagrangian Algorithms

by

Boyang Chen

A thesis submitted to the University of Birmingham for the degree of

DOCTOR OF PHILOSOPHY

School of Engineering

College of Engineering and Physical Sciences

University of Birmingham

July 2022

Abstract

This PhD thesis presents a numerical investigation of turbulent dispersed multiphase flows based on Large-Eddy simulation (LES). A wide range of engineering scenarios involve multiphase flow and require a fundamental understanding of the fluid mechanisms induced by different scales of motion. The numerical model is developed based on an in-house Computational Fluid Dynamics (CFD) code using a point-particle Eulerian-Lagrangian (PP-EL) algorithm and aimed for a universal numerical approach to simulate practical multiphase flows. The core of the thesis document is composed of three journal manuscripts where subsequent developments of this algorithm are applied to flows of engineering interest (i.e., chemical, ocean and environmental engineering) and validated versus experiments. The numerical results in each work remarkably agree with experimental results.

The first chapter starts by showing the first application of an Eulerian-Lagrangian strategy to the prediction of buoyancy-induced mixing with a thorough and successful validation. The aim of this research is to explore the optimal design of aerators in chemical reactors. This is achieved by quantifying the buoyancy-driven mixing produced by bubble screens and different arrangements of the individual plume, and examining the impact of gas flow rate and the depth of the reactor on the mixing time. The outcome of this work indicates a better performance provided by bubble screens, saving at least 20% of the energy usage in aeration.

The second chapter focuses on gravity currents driven by inertial particles (particle-driven currents or turbidity currents). The solver uses an Eulerian-Lagrangian point-particle algorithm to provide four-way coupling of the ambient fluid and the suspension of solid particles, with the interaction between particles being handled by a soft-sphere collision model. The results explore the dynamics of turbidity currents when compared to density-driven gravity currents, highlighting the influence of inertial particles on the propagation of the currents and the scales of motion of the coherent structures generated at the shear layer. The simulations reveal that the

dissipation rate of the turbulent kinetic energy within the current is mostly due to the contribution of the settling of solid particles. It is shown as well that the removal of the lock gate affects the early flow development whereas has little influence on the front speed of the current.

Combining the implementations made in the first two chapters, the third chapter introduces a novel modelling tool for the activated sludge process (ASP) based on large-eddy simulation and multiphase Eulerian-Lagrangian coupling. The model uses an Eulerian-Lagrangian point-particle algorithm that respects the discrete nature of both sludge flocs and air bubbles. Four-way coupling is implemented, where the interaction between solid particles is handled by a soft-sphere collision model. Subsequently, the integrated model is used to simulate a realistic scenario within the aeration basin of a wastewater plant and explore its results across a wide parameter range (aerator distribution, dissolved Oxygen levels, air flow rate, sludge size, bubble size). The results indicate that the initial dissolved Oxygen levels within the basin (related to weather conditions and aeration frequency) are critical for sludge activation, with initial anoxic conditions being very taxing. For a given flow rate, bubble screens (i.e, more aerators) provide significantly better performance.

Dedication

To Bo Xue, Yong Xue, Hongde Xue, Suisheng Liu, Zhanjiang Wei, Rongze Wei, Wenming Chen.

Acknowledgements

I would like to express my biggest thank to my supervisor Dr. Bruño Fraga for his great academic and financial support. I am grateful for his suggestion and help in encouraging my PhD work. I have been extremely lucky to have a supervisor who cared so much about my work, and who responded to my questions and queries so promptly. Very impressive communication and management in his research group (Dr. Yu Zhang and Dr. Riza Siregar) make me still work well after the outbreak of the coronavirus disease 2019 (Covid-19), where I share my work progress in the online meetings.

I would also like to express my gratitude to my parents and girlfriend Dr. Zhen Liu. Without their tremendous support and understanding in the past few years, it would be impossible for me to complete my PhD study. The chats with my family help me go through the toughest lockdown period due to COVID-19. And the discussions with Dr. Zhen Liu provide a great inspiration and encouragement for my academic research.

I also appreciate all the members of staff at the University of Birmingham who helped me with my research, particularly Dr. Mehdi Jangi who is an independent academic reviewer to assess my progress during my PhD study. I would like to extend my sincere thanks to Dr. David Soper who hosts my PhD viva, Dr. Jason Stafford who is internal reviewer for my PhD viva and Prof. Sylvain Laizet who is external reviewer for my PhD viva. Without their suggestions on my research, this work would have not been the same.

Contents

List of Figures

List of Tables

Chapter 1

Introduction

1.1 Turbulent Dispersed Multiphase Flow

Dispersed multiphase flows consist of two or more fluids in different phases of aggregation, including a continuous phase and at least a dispersed phase. The continuous phase is the fluid continually flowing in a connected region of space, such as water in a tank or air in the atmosphere. The dispersed phase refers to particles (solid), droplets (liquid) and bubbles (gas), which are discretely distributed within the continuous phase. There are many examples of dispersed multiphase flows in our everyday experience, such as raising air bubbles in boiling water, aerosols suspended in the atmosphere and smoke exhausting from a chimney. It is crucial to understand the multiphase flows encountered in engineering and environmental scenarios in order to provide a theoretical support for the optimal design of enhanced cost-effective technologies in realistic conditions and the forecasting of relevant processes and risks. This can manipulate such air flows to minimise the energy usage, while retaining a safe and comfortable environment for people to live and work. As

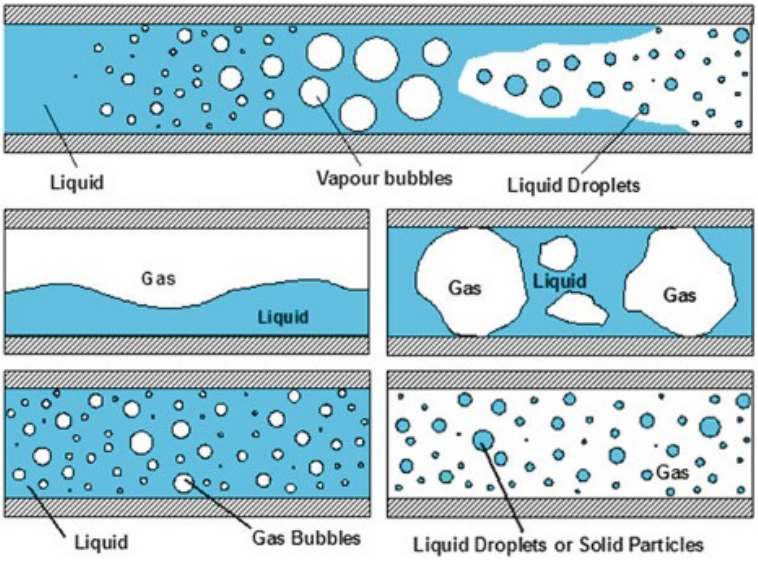

Figure 1.1: Turbulent dispersed two-phase flows [150]

shown in Figure. 1.1, gas-liquid flows where the liquid is the continuous phase and gas is the dispersed phase are naturally encountered in chemical and environmental engineering, such as buoyant plumes generated by aeration in wastewater treatment plants and chemical reactors. Gas-liquid flows are also extremely relevant in air pollution research where discrete liquid droplets (dispersed phase) are transported by gas (continuous phase). Gas-solid and liquid-solid flows are usually considered as particle-laden flows since the solid particles are denoted as the dispersed phase and interact with the surrounding flow of the carrier phase (gas and liquid). Examples with far-reaching practical implications can be found in river engineering (the sedimentation of solid particles transported by water), chemical engineering (rising suspension of solid particles in fluidized bed) and environmental engineering (activation of solid sludge particles in wastewater or micro-plastics in the ocean). Such flows exhibit turbulent or pseudo-turbulent behaviour at a wide range of scales, where the continuous phase acts as a matrix that carries or is agitated by the discrete particles (i.e., bubble, droplet and solid particles) by different material properties (i.e., density and viscosity) and the discontinuous instabilities induced by the dispersed phase have a disruptive influence on the surrounding fluid. Understanding the mechanisms of dispersed multiphase flows is a major challenge since these flows

are always unsteady, irregular and dissipative [56]. Compared to single-phase flows, one of the main difficulties in multiphase flows is that a wide range of scales of motion are triggered and driven by particles (particles in here refer to solid particles, air bubbles and droplets) rather than elements in the discrete phase in general (the patterns of single-phase turbulence). Recent research conducted by [88] has found that the energy cascade of turbulent flows is not clear in dispersed multiphase flows since the particles are an additional source of turbulent kinetic energy. Their results are different from the theory of turbulent flows based on single-phase flows where the dissipation of scales follows the memorable $-5/3$ spectral slope. In addition, the interaction between the phases is very difficult to capture, since the interface separating the liquid phase from the gas phase is extremely thin in bubbly flows, which leads to lots of challenges in studying the interfacial forces acting on each bubble [151]. Apart from that, in order to capture such interphases and the abrupt discontinuity in turbulent multiphase flows, the research normally requires extremely high resolution which is detrimental to the solution of the entire system. Extensive laboratory experiments were conducted to study the dynamics of turbulent dispersed multiphase flow and are mainly achieved by particle image velocimetry (PIV) and laser induced fluorescence (LIF) technology [95]. The researchers mostly monitored the velocity of the dispersed phase in multiphase flows and visualized the change of particles' shape. These experimental methods have been developed and established in the last two decades but are not able to investigate a wide range of design alternatives in practical engineering applications. With the fast-growth of computational resources, computational fluid dynamics (CFD) technology has been used with great success to provide applied solutions for single-phase flows. These models provide approximate solutions to the Navier-Stokes (N-S) equations (or a simplified version of them), in which the nonlinear self-advection term introduces energy transfer among different scales of motion, which are particularly challenging for modellers. This is particularly true in multiphase flows, where the dispersed phase (e.g., solid parti-

cles, bubbles, droplets) induces a wide spectrum of time-length scales requiring an accurate treatment of nonlinear instabilities.

Numerical strategies for simulating turbulent dispersed multiphase flows have been significantly developed to provide an accurate treatment of the continuous and dispersed phases as well as the coupling and interaction between the two. Regarding the turbulence closure for the continuous phase, there are three major modelling alternatives: Direct Numerical Simulation (DNS), Large Eddy Simulation (LES) and Reynolds-Averaged Navier-Stokes simulation (RANS). DNS is acknowledged as the most accurate approach, but solving all the turbulence scales prevents its application to practical scenarios due to its high computational cost for high Reynolds numbers and particle counts. LES can explicitly capture large-scale turbulent structures and model the less energetic small-scale structures through a subgrid-scale (SGS) model, being capable to solve the unsteady turbulent fluctuations in multiphase flows. On the other hand, the whole concept of large-eddy simulation is challenged by the fact that smaller scales could be relevant to turbulent kinetic energy production in dispersed flows, and sub-grid scale models seem to fail to predict so. RANS has been the most common approach to predict multiphase flows until the last decade; RANS-based simulations provide a good compromise for practical applications by introducing closure models to account for the turbulent fluctuations. However, the assumption of isotropic turbulence embedded in the most popular RANS models is rather unnatural for turbulent dispersed flows.

On the other hand, there are main three approaches to couple the dispersed phase with the continuous phase: Eulerian-Eulerian (EE), Eulerian-Lagrangian (EL), Interface-solving (IS). IS models are widely used for fundamental research on physical mechanisms of the interaction between two phases but the high computational cost limits their practical application. The main challenge for this method is to represent accurately the interphase within a reasonable computational expenditure. There are

many different approaches based on the definition of such interphases, such as Volume of Fluid and Level-Set Methods. EE approaches compute the continuous and dispersed phase in an Eulerian framework by introducing a void fraction to describe the two phases. The models have been applied in many practical multiphase flows with the great advantage of low computational cost. However, unique representation for the dispersed phase prevents EE models from forecasting the large-scale dynamics without addressing the particle disruption. EL algorithms are fundamentally different from the other two approaches in that each phase is solved on a different framework. As a result, one major challenge of this method lies in the mapping and interaction between the different phases.

In this Doctoral thesis, a LES-based Eulerian-Lagrangian model is applied to investigate the fluid mechanisms of turbulent dispersed multiphase flows. The research is firstly focused on fluid-gas interaction, where the model is applied to predict turbulent mixing by buoyant plumes and validate its accuracy with experimental measurements. Fluid-solid interaction is explored in this work by developing a novel Eulerian-Lagrangian approach to simulate particle-laden flows. The accuracy of the developed model is examined by characterising the suspension of solid particles in a carrier fluid and comparing the results against experimental data. Moreover, the interaction between the three phases (including fluid, solid and gas) is predicted by incorporating a new Eulerian-Lagrangian model with the biological kinetics model. The completed model is aimed at proposing a novel numerical strategy for simulating activated sludge process in wastewater treatment plants.

1.2 Modelling Strategies for the Continuous Phase

1.2.1 Governing Equations of Fluid

Navier-Stokes equations are a set of partial differential equations describing the mass and the motion conservation of fluid. The way to describe the flow field can be categorized into: Lagrangian and Eulerian description [7]. The former one is applied to track individual fluid particles by computing their positions and velocities as a function of time. The physical information of each particle is described by Newton's laws and conservation of mass and energy. The latter one defines a control volume and describes the flow properties as fields rather than identifying fluid particles. The fluid mechanisms can be continually calculated by pressure and velocity field within the control volume. Thus, there are mainly three approaches to drive the mass balance equation (which is usually called as continuity equation): Eulerian finite element (EFE), Lagrangian finite volume (LFV) and Lagrangian finite element (LFE). LFV method is based on the finite volume method in which the properties are integrated over a finite volume and the flux within the volume is calculated. Considering a finite volume with the volume τ and the mass m,

$$m = \int_{\tau} \rho d\tau \tag{1.1}$$

where ρ refers to the density of fluid, taking time derivative on the both side of Eq. 1.1, the equation can be written as follow based on the mass conservation and usually refers to the material derivative describing the time rate of change of some physical properties (heat or velocity),

$$\frac{Dm}{Dt} = \int_{\tau} \frac{D\rho}{Dt} d\tau + \int_{\tau} \rho \frac{D}{Dt} d\tau = 0 \tag{1.2}$$

According to the definition of divergence shown below and the Gaussian theory,

$$\frac{D\rho}{Dt} = \frac{\partial\rho}{\partial t} + u\frac{\partial\rho}{\partial x} + v\frac{\partial\rho}{\partial y} + w\frac{\partial\rho}{\partial z} = \frac{\partial\rho}{\partial t} + \vec{u}\cdot\nabla\rho \tag{1.3}$$

Eq. 1.2 can be expressed as,

$$\int_\tau \frac{D\rho}{Dt}d\tau + \int_\tau \rho\frac{D}{Dt}d\tau = \int_\tau \left(\frac{\partial\rho}{\partial t} + \nabla(\rho\vec{u})\right)d\tau = \int_\tau \frac{\partial\rho}{\partial t}d\tau + \int_S \rho\vec{u}_n dS = 0 \tag{1.4}$$

Based on the continuity assumption (mass conservation), Eq. 1.4 can be simplified as,

$$\frac{\partial\rho}{\partial t} + \frac{\partial(\rho u)}{\partial x} + \frac{\partial(\rho v)}{\partial y} + \frac{\partial(\rho w)}{\partial z} = \frac{D\rho}{Dt} + \rho(\frac{\partial u}{\partial x} + \frac{\partial v}{\partial y} + \frac{\partial w}{\partial z}) = 0 \tag{1.5}$$

which is the Lagrangian form of continuity equation. Different from finite volume method, finite element method focus on the properties integrated over a finite element and does not rely on the calculation of flux. In LFE approach, the mass conservation within the elements is applied to derive the continuity equation by identifying a finite volume element $d\tau$ with the mass dm,

$$\frac{D}{Dt}dm = \frac{D}{Dt}(\rho d\tau) = \rho\frac{D}{Dt}d\tau + d\tau\frac{D}{Dt}\rho = 0 \tag{1.6}$$

divide the both side of Eq. 1.6 by $\rho d\tau$ and based on the divergence theory,

$$\rho\frac{D}{Dt}d\tau + d\tau\frac{D}{Dt}\rho = \frac{1}{d\tau}\frac{D}{Dt}d\tau + \frac{1}{\rho}\frac{D\rho}{Dt} = \nabla\vec{u} + \frac{1}{\rho}\frac{D\rho}{Dt} = 0 \tag{1.7}$$

which is identical to Eq. 1.5. Eq. 1.5 and Eq. 1.7 indicate that relative volume change rate should be equal to relative density change rate within a volume or an element, which is shown in Fig. 1.2. Focusing on Eulerian description, a finite element is defined as shown in Fig. 1.3. The flux through the inlet face $ABCD$ can

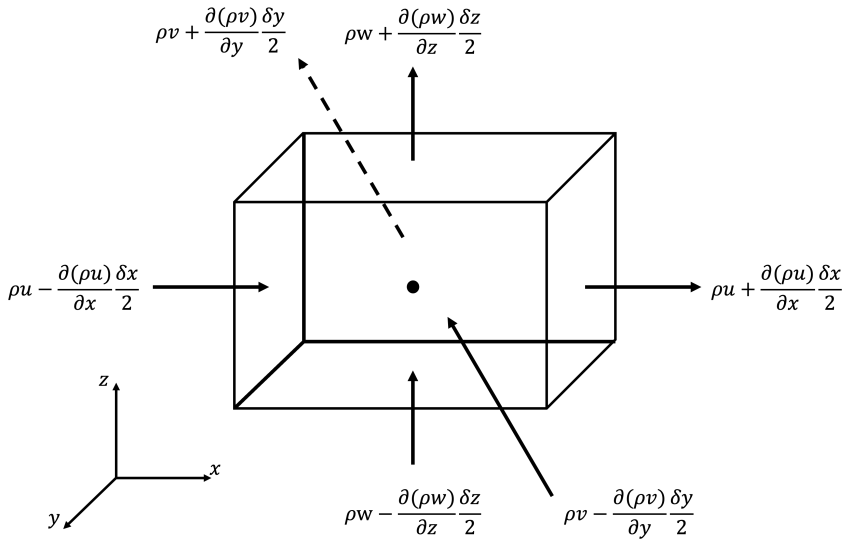

Figure 1.2: Mass conservation of a finite element

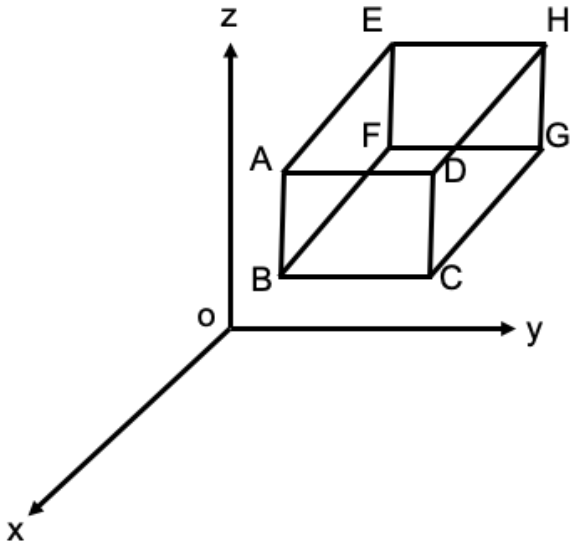

Figure 1.3: Mass conservation of finite volume in Cartesian coordinate

be written as follow,

$$\Phi_{ABCD} = \left[\rho u + \frac{\partial(\rho u)}{\partial x}dx\right] dydz \tag{1.8}$$

and the flux through the outlet area $EFGH$ is expressed as,

$$\Phi_{EFGH} = \rho u dydz \tag{1.9}$$

where Eq. 1.8 and Eq. 1.9 represent the flux in one direction (x component). To account for the other two components incorporated on the mass rate of change described as following,

$$\dot{m} = \frac{\partial \rho}{\partial t}dxdydz \tag{1.10}$$

the mass conservation can be obtained,

$$\frac{\partial \rho}{\partial t} + \frac{\partial(\rho u)}{\partial x} + \frac{\partial(\rho v)}{\partial y} + \frac{\partial(\rho w)}{\partial z} = 0 \tag{1.11}$$

On the other hand, the motion balance of fluid can be given by Newton's second law of which mathematical expression in one direction x is written as $F_x = ma_x$. Consider a finite element depicted in Fig. 1.4, F_x representing total force acting in x direction is as follow,

$$F_x = \left[-\frac{\partial p}{\partial x} + \frac{\tau_{xx}}{\partial x} + \frac{\tau_{yx}}{\partial y} + \frac{\tau_{zx}}{\partial z}\right] dxdydz + \rho f_x dxdydz \tag{1.12}$$

where τ refers to three shear stress components acting on finite element and f refers to the external force, and the mass of finite element m can be written as $\rho dxdydz$ which is combined with Eq. 1.12 and gives the balance equation,

$$\rho \frac{Du}{Dt} = -\frac{\partial p}{\partial x} + \frac{\tau_{xx}}{\partial x} + \frac{\tau_{yx}}{\partial y} + \frac{\tau_{zx}}{\partial z} + \rho f_x \tag{1.13}$$

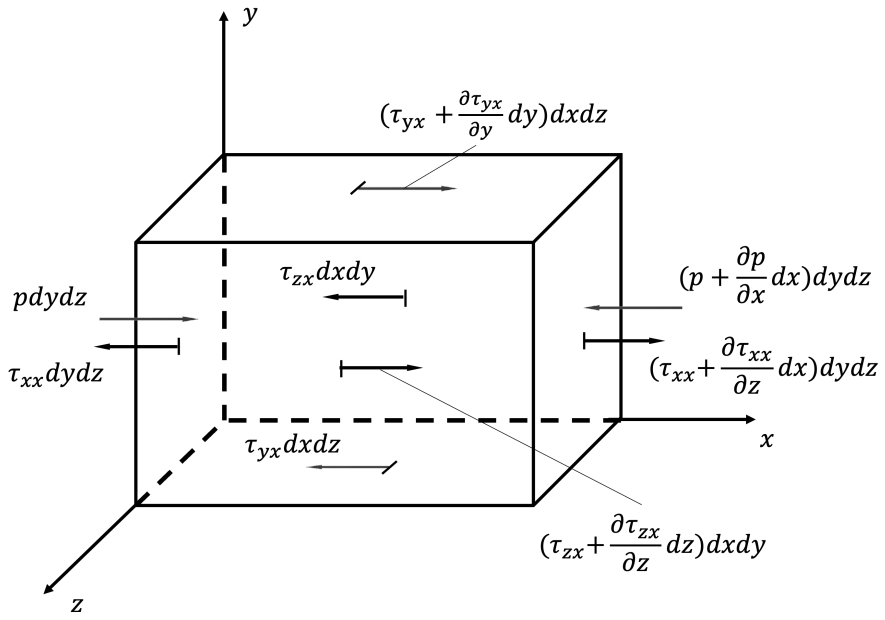

Figure 1.4: Stress components on the faces of a finite volume

where the acceleration of finite element is represented by the material derivative of velocity Du/Dt which can be separated into as follow,

$$\rho \frac{Du}{Dt} = \frac{\partial(\rho u)}{\partial t} - u\frac{\partial \rho}{\partial t} - u\nabla \cdot (\rho v) + \nabla \cdot (\rho uv) \tag{1.14}$$

where u and v represent two velocity components. Since the sum of the second and the third term in the RHS of Eq. 1.14 is zero based on the continuity equation Eq. 1.5, Eq. 1.14 is simplified as,

$$\rho \frac{Du}{Dt} = \frac{\partial(\rho u)}{\partial t} + \nabla \cdot (\rho uv) \tag{1.15}$$

and the momentum balance equation of finite element in x direction can be expressed as follow,

$$\frac{\partial(\rho u)}{\partial t} + \nabla \cdot (\rho uv) = -\frac{\partial p}{\partial x} + \frac{\tau_{xx}}{\partial x} + \frac{\tau_{yx}}{\partial y} + \frac{\tau_{zx}}{\partial z} + \rho f_x \tag{1.16}$$

Hence, the full N-S equations can be obtained from the continuity and momentum equations. The N-S equations were originally proposed by Swiss mathematician Leonhard Euler in the xviii century to describe incompressible and frictionless fluids. These equations are called Euler equations where viscosity terms are ignored. French engineer Claude-Louis Navier developed Eulerian equations for the more realistic flows by introducing the viscosity of the fluid. In the $19th$ century, Irish English physicist Sir George Gabriel Stokes improved the Euler equations and successfully applied the equations to predict two-dimensional flows, which are called Navier-Stokes equations. Considering an incompressible Newtonian flow, the momentum balance equation of Navier-Stokes equations is as follows,

$$\frac{\partial}{\partial t}u + u \cdot \nabla u = -\nabla p/\rho - \nu \nabla \times \omega + \frac{1}{\rho}f \tag{1.17}$$

where $u(x,t)$ and $p(x,t)$ represent the velocity and the pressure field of fluid, ρ and ν are the density and the kinematic viscosity. The term $u \cdot \nabla u$ describes the convection caused by material property and external forces on fluid, such as the density of fluid and gravity. The term $\nu \nabla \times \omega$ describing the diffusion process (where the fluid properties are transported by turbulent motion) can be written as $\nu \nabla^2 u$ according to the relationship $\nabla^2 u = \nabla(\nabla \cdot u) - \nabla \times \omega$ in which $\omega = \nabla \times u$ is the vorticity field. The last term in the RHS of Eq. 1.17 refers to the sum of body forces acting on the fluid, which are a function of spatial location x and time t. On the other hand, the continuity equation of Navier-Stokes equations revealing mass conservation of the incompressible fluid is as follows,

$$\nabla \cdot u = 0 \tag{1.18}$$

For a compressible flows in which Mach number $Ma = u/c$ is very high and fluid density is strongly affected by high-speed flows (gas), the perfect gas equation is

applied to describe the energy conservation of the flows,

$$PV = nRT \tag{1.19}$$

where P and V represent pressure and volume of gas, R is ideal gas constant, n and T refer to the amount of substance and temperature of the gas. And the N-S equations describing a compressible flow can be expressed as,

$$\frac{\partial \rho}{\partial t} + \nabla \cdot (\rho u) = 0 \tag{1.20}$$

$$\frac{\partial (\rho u)}{\partial t} + \nabla \cdot (\rho u \otimes u) = -\nabla p + \mu \nabla \cdot [\nabla \otimes u + (\nabla \otimes u)^T - \frac{2}{3}(\nabla \cdot u) I] + f \tag{1.21}$$

where Eq. 1.20 and Eq. 1.21 represent the mass and momentum conservation of compressible flows. In order to model the compressibility, the energy conservation is also included and expressed as follows (Eq. 1.22),

$$\frac{\partial E}{\partial t} + \nabla \cdot [(E+p)u] = \mu \nabla \cdot ([\nabla \otimes u + (\nabla \otimes u)^T - \frac{2}{3}(\nabla \cdot u) I] \cdot u - k \nabla T) + f \cdot u \tag{1.22}$$

Such systems implicate a wide range of scales, such as a characteristic velocity scale U, a characteristic length scale L and a resulting characteristic time scale L/U. In order to model and resolve all scales of motion, the solutions are commonly proposed in two frameworks: Eulerian and Lagrangian. In an Eulerian framework, the N-S equations are computed in Cartesian coordinates where a mesh is applied to divide the flow field into many elements and construct a controlled volume or element. As previously mentioned, there are three modelling alternatives: Direct Numerical Simulation (DNS), Large Eddy Simulation (LES) and Reynolds-Averaged Navier-Stokes Simulation (RANS). The fundamental difference lies in the way they resolve the myriad of scales of motion generated by turbulence. Fig. 1.5 shows the characteristic features of these three approaches to capture turbulent eddy structures.

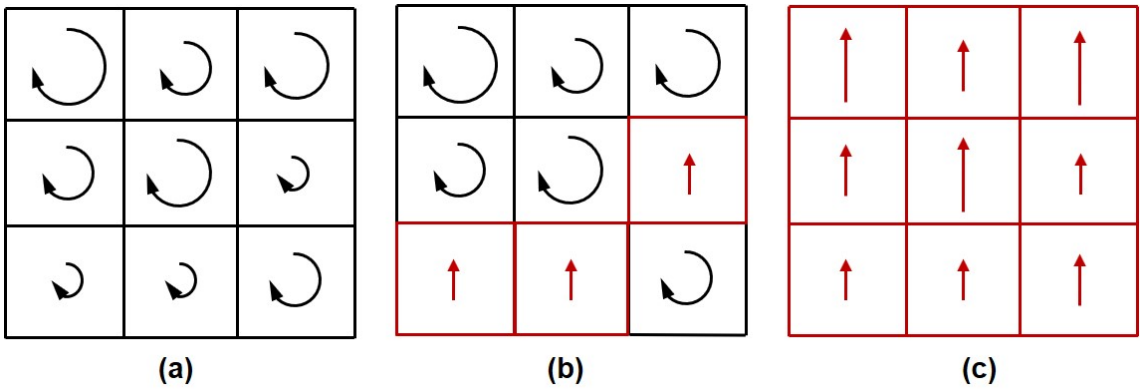

Figure 1.5: Solution of natural eddy structures by three different approaches: (a) Direct Numerical Simulation (DNS); (b) Large Eddy Simulation (LES); (c) Reynolds-Averaged Navier-Stokes Simulation (RANS); red blocks and arrows: modelled isotropic eddy structures; black blocks and arrows: natural eddy structures.

Black lines represent the eddy structures of natural turbulence and red lines represent the modelled eddy structures. DNS respects the natural physics and resolves all the scales. By filtering the scales, LES models solve the larger scales (black lines) and model the small scales (red lines) based on isotropic turbulentce assumption. In RANS models, all the scales are modelled as isotropic eddy structures. More details about these three models are explained in the following sections. Regarding the Lagrangian approach, the idea is to apply particle mechanics to describe flow field rather than solve the N-S equations. The dynamics of a discrete particle can be expressed as,

$$\frac{dr_i}{dt} = u_i \tag{1.23}$$

where r_i and u_i represent the position and velocity of particle i [78]. Two popular Lagrangian algorithms are Smooth-Particle Hydrodynamics (SPH) [36] and Lattice Boltzmann Method (LBM) [31]. Compared to a conventional Eulerian approach, SPH models have the great advantage of dealing with complex boundaries with high computational efficiency, such as free surface flows and gravity currents. Field variables in a SPH simulation can be computed by interpolation of individual Lagrangian variables. For example, the density field in SPH models can be described

as,

$$\rho(r) = \sum_j V_j \rho_j W(\mid r - r_j \mid, h) = \sum_j m_j W(\mid r - r_j \mid, h) \tag{1.24}$$

where ρ_j refers to the density of particle j, m_j and V_j represent the volume and mass of particle j. W is a weighting function that is used to interpolate the density of particles based on particle position r. h refers to the size of the influenced area in which particles interact through a kernel function. Despite the increasing application of SPH models in simulating solid mechanics and fluid flow, there are some limitations to this approach: boundary conditions (i.e. inlet and outlet conditions) are more difficult to set up and speed up the calculation of each particle is a challenging task and computationally expensive when dealing with complex flow system [156]. LBM models the fluid as particles which can interact with each other over a discrete lattice rather than solve the conservation of fluid macroscopic properties in an Eulerian framework. A potential application of this model is the simulation of multiphase flows, where the different phases are fully resolved with effective parallel computing. However, this model struggles to reproduce conservation laws in the flow field and interface between the phases, and is limited to capture the compressibility of high-speed flows [74]. In general, Lagrangian approach provide many novel concepts and possibilities of solving fluid mechanics more efficiently, while requiring further development in terms of forecasting complex flows (e.g., high-Re and non-Newton flows). In the proposed study, turbulent multiphase flows encountered in practical scenarios are investigated and involve complicated motion of scales, which compels the work to calculate the continuous phase by a conventional approach (Large-eddy simulation) in Eulerian framework. Therefore, the following sections are aimed at showing background about the modelling schemes in an Eulerian framework and the potential application of Lagrangian model explained in this section will be discussed in the Future Work section.

1.2.2 Direct Numerical Simulation

As shown in Fig. 1.5, DNS simulations respect the structures from natural flow and directly solves Eq. 1.17 and Eq. 1.18. This method is acknowledged as the most accurate computational approach by solving all the turbulence scales [88, 89, 91, 90]. Its accuracy can be assessed based on the Kolmogorov scale which is defined as the smallest scale in turbulent flow,

$$\eta = (\nu^3/\varepsilon)^{1/4} \tag{1.25}$$

where ν and ε represent kinematic viscosity and kinetic energy dissipation. In this approach, the most of the kinetic energy containing from the smallest dissipative scale to the integral scale is resolved in the computational mesh without modelling turbulent scales. It is important to consider the computational cost when applying a DNS scheme to predict complex flows. The Reynolds number $Re = UL/\nu$ appears naturally by length scale L and can be estimated by the Kolmogorov scale η,

$$\frac{\eta}{L} \approx Re^{-3/4} \tag{1.26}$$

Therefore the required grid resolution in three-dimensional DNS can be obtained as $N_{3D} = (L/\eta)^3 = Re^{9/4}$ which prevents the model's application to practical scenarios due to high computational cost (i.e. the required grid point reaches around $10^{22.5}$ when solving an actual high-speed flow with $Re = 10^5$). DNS models are applied to understand the complex mechanisms in turbulent dispersed multiphase flows. The research conducted by [88] applied DNS model to explore bubble-induced turbulence (BIT) in bubbly flows. Their numerical results highlight the difference between single-phase and two-phase flows in terms of the motion of scales induced by the dispersed phase, which has been adopted to examine the capability of other models. Moreover, J. Capecelatro et al. [25] applied high-fidelity simulation by DNS models

to examine the mechanisms of particle-induced turbulence. And researchers from the University of Florida [12] established DNS-based fully-resolved database of particle-laden flows. They proposed a novel approach to predict dispersed multiphase flows by applying a machine learning algorithm to train obtained dataset.

1.2.3 Reynolds-Averaged Navier-Stokes

RANS approach averages all scales of motion based on isotropic assumption and has been the most common forecasting approach in practical engineering until the last decade. This model is based on the Reynolds decomposition for an instantaneous velocity component,

$$u = \bar{u} + u' \tag{1.27}$$

where u refers to the instantaneous velocity in the flow field. Combining with Eq. 1.17 and Eq. 1.27, the Navier-Stokes (NS) equations averaged in time are as follows,

$$\rho \frac{\overline{D}}{Dt}\overline{u_i} = \frac{\partial}{\partial x_j}\left[\mu\left(\frac{\partial \overline{u_i}}{\partial x_j} + \frac{\partial \overline{u_j}}{\partial x_i}\right) - \overline{p}\delta_{ij} - \rho\left\langle u_i' u_j' \right\rangle\right] \tag{1.28}$$

$$\frac{\partial \bar{u}_j}{\partial x_j} = 0 \tag{1.29}$$

where μ represents the dynamics viscosity, δ_{ij} refers to the Kronecker delta and the term $\rho\left\langle u_i' u_j' \right\rangle$ is the Reynolds stress generated by fluctuation. Eq. 1.29 and Eq. 1.28 reveal an unclosed system in which there are 4 equations for $i = 1, 2, 3$ and implicit summation over index j while 10 unknowns simultaneously need to be solved, mean pressure $\overline{p}$, three mean velocity components $\overline{u_i}$ and six Reynolds stresses $\left\langle u_i' u_j' \right\rangle$. To close this system, the Boussinesq hypothesis is applied to establish the relationship

between the transient turbulent fluctuations and the steady velocity derivatives,

$$-\rho\left\langle u_i' u_j' \right\rangle + \frac{2}{3}\rho k\delta_{ij} = \rho\mu_t(\frac{\partial \bar{u}_i}{\partial x_j} + \frac{\partial \bar{u}_j}{\partial x_i}) \tag{1.30}$$

Moreover, the equation transporting turbulent kinetic energy $k = \frac{1}{2}\left\langle u_i' u_j' \right\rangle$ is introduced as follow,

$$\frac{\partial(\rho k)}{\partial t} + \frac{\partial(\rho k u_i)}{\partial x_i} = \frac{\partial}{\partial x_j}\left[\frac{\mu_t}{\sigma_k}\frac{\partial k}{\partial x_j}\right] + 2\mu_t E_{ij}E_{ij} - \rho\varepsilon \tag{1.31}$$

and the rate of dissipation $\varepsilon = \nu\overline{\frac{\partial u_i'}{\partial x_l}\frac{\partial u_i'}{\partial x_l}}$ is transported by the formulae,

$$\frac{\partial(\rho\varepsilon)}{\partial t} + \frac{\partial(\rho\varepsilon u_i)}{\partial x_i} = \frac{\partial}{\partial x_j}\left[\frac{\mu_t}{\sigma_k}\frac{\partial \varepsilon}{\partial x_j}\right] + C_{1\varepsilon}\frac{\varepsilon}{k}2\mu_t E_{ij}E_{ij} - C_{2\varepsilon}\rho\frac{\varepsilon^2}{k} \tag{1.32}$$

where E_{ij} denotes to the rate of deformation and μ_t represented eddy viscosity that relates the turbulent kinetic energy k to the rate of dissipation ε,

$$\mu_t = \rho C_\mu \frac{k^2}{\varepsilon} \tag{1.33}$$

The Eq. 1.27 to 1.33 form the most popular RANS model $k-\varepsilon$ model, while the RANS approach has developed into other models (e.g., $k-\omega$ model) to extend its application to practical scenarios. Compared to DNS approach, RANS-based simulations provide a good compromise for practical applications by introducing closure models and a set of equations to account for the turbulent fluctuations rather than capturing all scales of motion. However, Eq. 1.31 to Eq. 1.33 involve with some empirical parameters σ_k, σ_ε, $C_{1\varepsilon}$ and $C_{2\varepsilon}$, revealing that the predicted numerical results highly rely on the value of these constants. In addition, eddy structures in the whole computational mesh are assumed as isotropic, which is rather unnatural and results in an underestimation of eddy viscosity (Eq. 1.33) in complex flows. Furthermore, it is challenging to resolve the mechanisms of turbulence when simulating turbulent

multiphase flows (usually strongly anisotropic) since RANS models are dissipative and conflict with the turbulent kinetic energy (TKE) generation at particle-scale[11].

1.2.4 Large Eddy Simulation

LES models capture large-scale turbulent structures and model the less energetic small-scale structures through a subgrid-scale (SGS) model. In order to avoid the under-prediction on unsteady structures caused by time averaging, LES models filter the property in space rather than in time, the filtered Navier-Stokes equations by LES (with continuity equation $\nabla \cdot u = 0$) is,

$$\frac{\partial \bar{u}_i}{\partial t} + \frac{\partial}{\partial x_j}(\bar{u}_i \bar{u}_j) = -\frac{1}{\rho}\frac{\partial \bar{p}}{\partial x_i} + \nu \frac{\partial^2 \bar{u}_i}{\partial x_j \partial x_j} - \frac{\partial \tau_{ij}}{\partial x_j} \tag{1.34}$$

where notation $-$ represents the space averaging and τ_{ij} represents the subgrid stress that can be combined into turbulent viscosity by eddy-viscosity model,

$$\tau_{ij} - \frac{1}{3}\delta_{ij}\tau_{kk} = -\nu_{sgs}(\frac{\partial \bar{u}_i}{\partial x_j} + \frac{\partial \bar{u}_j}{\partial x_i}) = -2\nu_{sgs}\overline{S}_{ij} \tag{1.35}$$

where ν_{sgs} refers to the turbulent eddy viscosity and $\overline{S}_{ij}$ refers to the rate-of-strain tensor. According to dimensional analysis,

$$\nu_{sgs}(m^2/s) \sim U_0(m/s) \times l_0(m) \tag{1.36}$$

where the viscosity is described by characteristic velocity U_0 and characteristic length l_0. Based on the assumption that the small scale eddies in subgrid is isotropic, characteristic velocity U_0 can be computed by a general characteristic length L_0,

$$U_0(m/s) \sim L_0(m) \times \frac{\partial U}{\partial z}(s^{-1}) \tag{1.37}$$

where the velocity gradient $\frac{\partial U}{\partial z}$ can be written as follows,

$$\frac{\partial U}{\partial z} = \sqrt{2} \times \sqrt{(\frac{1}{2}\frac{\partial U}{\partial z})^2 + (\frac{1}{2}\frac{\partial U}{\partial z})^2} = \sqrt{S_{ij}S_{ij}} =\mid S_{ij} \mid \tag{1.38}$$

Thus, the eddy viscosity is described as $\nu_{sgs} = L_0^2 \mid S_{ij} \mid$. The Smagorinsky model is the most known SGS model to differentiate the length scale $L_0 = C_S\Delta$ based on Lily-approximation [44],

$$\nu_{sgs} = (C_S\Delta)^2\sqrt{2\bar{s}_{ij}\bar{s}_{ij}} = (C_S\Delta)^2 \mid \bar{s} \mid \tag{1.39}$$

where $\Delta = (\Delta_{ijk})^{1/3}$ is the filter-width taken by the local grid size, C_S is Smagorinsky constant that is calculated as,

$$C_S = \frac{1}{\pi}(\frac{2}{3C_k})^{3/4} \tag{1.40}$$

where k is wavenumber and C_k is the Kolmogorov constant which is computed from the $-5/3$ energy spectrum law equation,

$$E_k = C_k\varepsilon^{2/3}k^{-5/3} \tag{1.41}$$

Extensive experiments carried out to measure C_k indicate that the normal range of the Smagorinsky constant C_S is from 0.065 to 0.25. RANS and LES models are two popular approaches to predict turbulent dispersed multiphase flows encountered in practice. RANS models have the advantage of saving computational cost but require an accurate treatment of the interaction between the dispersed phase and continuous phase since the isotropic assumption prevents the models from simulating the scales induced by the dispersed phase [121, 105]. In addition, some RANS-based simulations rely on a coarser Eulerian grid can result in an unreasonable ratio of bubble size to computational cell size when applying Lagrangian particle

tracking algorithm to predict bubbly flow [17]. LES can explicitly capture plume-scale turbulent structures in dispersed bubbly flows, reducing the relative influence of sub-grid scale (SGS) turbulence closures upon the predictions [47]. Recent research proves that LES models are more applicable for working with Lagrangian models to solve the dispersed phase [60, 53, 59, 41, 42].

1.2.5 Numerical Scheme

Finite Difference Method

In this work, the in-house code solver is applied to discretise Navier-Stokes equations in Cartesian coordinate by finite difference method (FDM). The FDM is a popular approach to solve partial derivative equations (PDEs) and based on the Taylor series,

$$\sum_{n=0}^{\infty} \frac{f^{(n}(a)}{n!}(x-a)^n \tag{1.42}$$

where $n!$ refers to the factorial of n, $f^{(n}(a)$ refers to the nth derivative of f evaluated at the point a. Considering a second-order Taylor expansion,

$$f(x+h) = f(x) + f^{'}(x)h + \frac{f^{(2}(x)h^2}{2!} + \frac{f^{(3}(x)h^3}{3!} \tag{1.43}$$

where h denotes to the grid size and another expression can be written as follow,

$$f(x-h) = f(x) - f^{'}(x)h + \frac{f^{(2}(x)h^2}{2!} + \frac{f^{(3}(x)h^3}{3!} \tag{1.44}$$

the difference between the Eq. 1.43 and the Eq. 1.44 contributes to the central differencing scheme for the first-order derivative,

$$f^{'}(x) = \frac{f(x+h) - f(x-h)}{2h} + O(h^2) \tag{1.45}$$

where O denotes to the truncation error (second-order) of this scheme. The Eq. 1.45 can be applied to obtain the discreitisation for higher order derivative, such as,

$$f^{''}(x) = \frac{f(x+h) - 2f(x) + f(x-h)}{h^2} + O(h^3) \tag{1.46}$$

Recall a generalized momentum equations in Navier-Stokes equations (i.e., Eq. 1.17), the advection and the diffusion term can be discretised by FDM and a typical central differencing for advection (first-order derivative in space) in two dimensions can be written as follow,

$$\frac{\partial u_i u_j}{\partial x_j} = u_i \frac{u_{i+1,j} - u_{i-1,j}}{2\Delta x} + u_j \frac{u_{i,j+1} - u_{i,j-1}}{2\Delta y} \tag{1.47}$$

where subscript i and j denote to the velocity in x and y direction, Δx and Δy represent the mesh size in two directions. Similarly, the diffusion (Laplacian velocity and second-order derivative in space) can be discretised by central differencing stencil,

$$\nu \frac{\partial^2 u_i}{\partial x_j \partial x_j} = \nu \frac{u_{i+1,j} + u_{i-1,j} + u_{i,j+1} + u_{i,j-1} - 4u_{i,j}}{\Delta^2 x} \tag{1.48}$$

In the field of CFD, FDM is usually applied to solve a set of PDEs, such as Navier-Stokes equations implicating a complicated coupled system and involving non-linearity (commonly refers to advection term). Comparing to other numerical schemes (i.e., finite element method and finite volume method), this scheme requires generally less computational cost to solve the equations, but the disadvantage is

that the results have only a low order of approximation. Thus, Neumann's stability analysis is applied to assess the accuracy of the scheme before identifying differencing stencil for Navier-Stokes equations [8]. Accordingly, some novel discretisation schemes are recently developed in order to mitigate numerical error and truncation error, such as high order central differencing scheme that is applied to avoid inaccuracy of calculating advection term by low order upwind scheme; Petrov-Galerkin dissipation scheme that can be used for mitigating the oscillations when solving advection term by low order central differencing scheme [26]. Apart from the central and upwind schemes, the modellers have developed some novel high-order schemes to enhance the robustness of FDM (i.e., TENO and WENO methods to avoid the oscillation produced by traditional differencing schemes [129, 63]).

Velocity-Pressure Coupling

When solving Navier-Stokes (NS) equations, the calculation of velocity and pressure field are coupled and the solution should satisfy the momentum and the continuity equation simultaneously. Consider a set of NS equations at time step $n+1$,

$$\begin{cases} \Delta u^{n+1} = \dfrac{u^{n+1} - u^n}{\Delta t} + (u^n \cdot \nabla) u^n + \nabla p^{n+1} \\ \nabla \cdot u^{n+1} = 0 \end{cases} \tag{1.49}$$

where the solution of the velocity at the current time step $n+1$ requires the information of the velocity at the last time step n and the pressure at time step $n+1$. The Semi-Implicit Method for Pressure Equation (SIMPLE) is the most popular algorithm to solve the coupled system, which was introduced by Brian Spalding and his student Suhas Patankar in the early 1970s. The main idea of this method is the solution of the Poisson equation which is based on momentum and continuity conservation [44]. The former one (momentum equation) can be expressed as follows,

$$MU = -\nabla p \tag{1.50}$$

where U and p represent velocity and pressure field, M is a coefficient matrix that is used to discretise the momentum equation. Consider the momentum conservation in x-direction, the expression of Eq. 1.50 is,

$$\begin{pmatrix} M_{1,1} & M_{1,2} & M_{1,3} & \cdots & M_{1,n} \\ M_{2,1} & M_{2,2} & M_{2,3} & \cdots & M_{2,n} \\ M_{3,1} & M_{3,2} & M_{3,3} & \cdots & M_{3,n} \\ \cdots & \cdots & \cdots & \cdots & \cdots \\ M_{n,1} & M_{n,2} & M_{n,3} & \cdots & M_{n,n} \end{pmatrix} \begin{pmatrix} U_1 \\ U_2 \\ U_3 \\ \cdots \\ U_n \end{pmatrix} = \begin{pmatrix} (\partial p/\partial x)_1 \\ (\partial p/\partial x)_2 \\ (\partial p/\partial x)_3 \\ \cdots \\ (\partial p/\partial x)_n \end{pmatrix} \tag{1.51}$$

and the matrix M can be divided into a diagonal and off-diagonal part,

$$-\nabla p = MU = AU - H \tag{1.52}$$

where A refers to the diagonal matrix and H refers to off-diagonal matrix, and velocity U can be calculated as,

$$U = A^{-1}H - A^{-1}\nabla p \tag{1.53}$$

substitute Eq. 1.53 into the continuity equation and obtain Poisson equation,

$$\nabla \cdot (A^{-1}\nabla p) = \nabla \cdot (A^{-1}H) \tag{1.54}$$

The general procedure of SIMPLE algorithm is summarized as following,

- Step1: Set up initial boundary condition for velocity and pressure

- Step2: Calculate velocity field based on the momentum equation, which might not satisfy the continuity equation
- Step3: Calculate pressure field based on Poisson equation
- Step4: Update new velocity field by the pressure calculated from step 3 in order to satisfy the continuity equation
- Step5: Go back to step 1 if the new velocity field does not meet the momentum equation

This algorithm has been widely used to solve the Navier-Stokes equations and extended to some novel numerical strategies for solving coupled systems, i.e. Pressure-Implicit with Splitting of Operators (PISO) algorithm. On the other hand, the projection method was introduced in McCulloch (1994) and developed by Nolan and Panorska (1997) for decoupling the system (u^{n+1}, p^{n+1}) within two time steps. In the first step, the velocity field u^* in NS equations is computed without considering the continuity equation and pressure field,

$$\begin{cases} \Delta u^* = \dfrac{u^* - u^n}{\Delta t} + (u^n \cdot \nabla) u^n \\ \nabla \cdot u^* = 0 \end{cases} \tag{1.55}$$

where the convection-diffusion equation is solved based on the momentum equation. In the second step, computed velocity u^* is projected into a divergence-free field by solving the Poisson equation,

$$\begin{cases} u^* = u^{n+1} + \Delta t \nabla p^{n+1} \\ \nabla \cdot u^{n+1} = 0 \end{cases} \tag{1.56}$$

In this approach, the pressure field is described numerically and does not play a physical role in the NS equations, acting as a Lagrangian multiplier to correct the

predicted velocity from the first step. As a result, the calculation of the projection method is more efficient than solving a coupled system and the whole procedure relaxes the definition of pressure boundary condition. However, the assumption of the pressure file limits this approach to simulate compressible flows and reproduce the flow system with complex boundary conditions [13]. In this thesis, the projection method is applied in the code solver since turbulent multiphase flows are investigated and considered as incompressible flows.

Multi Grid Algorithm

Considering the Eq. 1.56 and taking a divergence for both side of the equation, the Poisson equation can be expressed as follow,

$$\nabla^2 p^{n+1} = \frac{\nabla \cdot u^*}{\Delta t} \tag{1.57}$$

discretising the equation by central differencing in 2D space and can obtain as follow,

$$\frac{p^{n+1}_{i-1,j} - 2p^{n+1}_{i,j} + p^{n+1}_{i+1,j}}{\Delta x^2} + \frac{p^{n+1}_{i,j-1} - 2p^{n+1}_{i,j} + p^{n+1}_{i,j+1}}{\Delta y^2} = \frac{u^*_{i+1,j} - u^*_{i-1,j}}{2\Delta x} + \frac{v^*_{i,j+1} - v^*_{i,j-1}}{2\Delta y} \tag{1.58}$$

where the RHS is calculated from the first step in the projection method and Eq. 1.58 can be considered as a large matrix system expressed as,

$$Ax = s \tag{1.59}$$

where s refers to the divergence of the computed velocity u^* (known variables), x represents the pressure matrix and A denotes to the coefficient matrix. Such

equations establish a diagonally dominant system of linear equations and can be solved by the Jacobi method of which iterative solution is,

$$x^{n+1} = D^{-1}(s - (L + U)x^n) \tag{1.60}$$

where A is a diagonal matrix (see Eq. 1.54), L is a lower triangular part and U is an upper triangular part. The x^n denotes to the initial guess of the solution and the x^{n+1} can be iteratively determined within convergence errors. It should be noticed that the initial guess significantly determines the speed of convergences in the Jacobi iteration (i.e., a 'bad' initial guess can result in more iterations to obtain the solution), which can raise challenges in solving a complex system [153]. Multigrid is an algorithm for solving PDEs and its idea is to accelerate the convergence of a basic iterative method (i.e., Jacobi) [159]. Specifically, this method is based on filtering short and long wavelength scales and treating them on the different resolution grids. The main steps are explained as follows (here we use the Jacobi iteration method that can be replaced with other iterative methods such as the Gauss-Seidel iteration method),

- Pre-smoothing: the initial solution is obtained by a few iterations based on the initial guess, which contributes to the residual errors ($r = Ax - s$) on the fine grid;

- Restriction: the residual errors are downsampled into the coarser grid by interpolation and calculated by iterative methods on the coarsest gird;

- Prolongation: the computed residual errors are interpolated back into the fine grid;

- Correction: the initial solution is corrected by the residual errors interpolated from the prolongation;

According to different systems, there are many options for choosing multigrid methods in terms of enhancing the speed of solving a single iteration and the rate of convergence with iterations [18]. This classifies multi-grid into the three main types, which are V-cycle, F-cycle and W-cycle [104, 153]. The proposed code solve in this thesis adopts F-cycle, where the correction (which is called as post-smoothing) is implemented between the different grids during prolongation.

1.3 Modelling the Dispersed Phase

Regarding the simulation of multiphase flows, it is a challenging task to characterise the instantaneous perturbations caused by the dispersed phase in a carrier fluid, such as the instabilities generated by the settling of solid particles in gas or liquid and the shear layer between dispersed rising bubbles and liquid (wake generated around bubble are difficult to capture). Such flow structures implicate a wide range of scales (See Figure. 1.6) and require a proper treatment of the continuous and the dispersed phases as well as the coupling and the interaction between the two. According to the relative particle size and volume fraction of particles [11], there are five ways to describe the motion of dispersed phase when interacting with continuous phase: Dusty gas approach, Equilibrium Eulerian approach, Eulerian Eulerian approach, Lagrangian point-particle approach and interface-solving approach, which are summarized in Fig. 1.7. As shown in Figure. 1.7, τ_p represents the particle scale, where particle generally refers to solid particles, bubbles and droplets in turbulent dispersed multiphase flows. And a larger particle size will contribute to a higher value of τ_p of which mathematical expression will be explained in the following section. The word 'relax' refers that the limitation of the particles scale on algorithms, where the assumptions embedded in simplified models are not able to simulate the dynamics of large-scale particles. From a physical point of view,

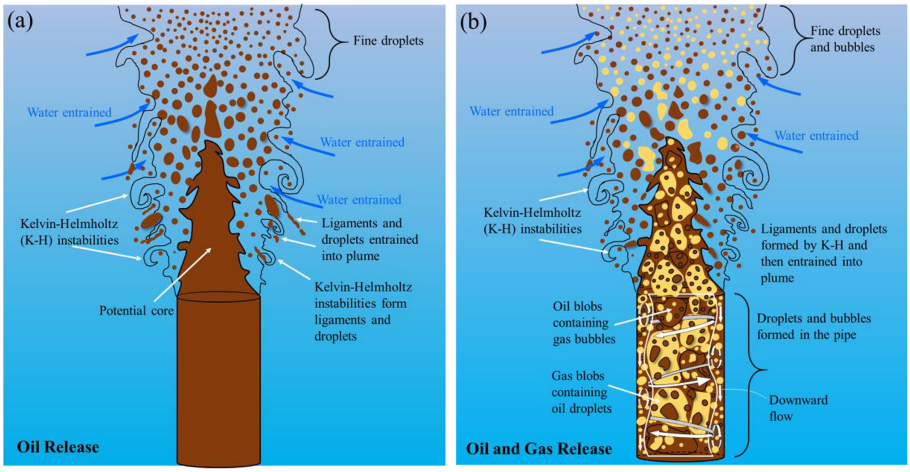

Figure 1.6: Kelvin-Helmholtz (KH) instabilities driven by turbulence within the plume for jets of fluids into water: (a) oil only release. (b) oil and gas release.[16]

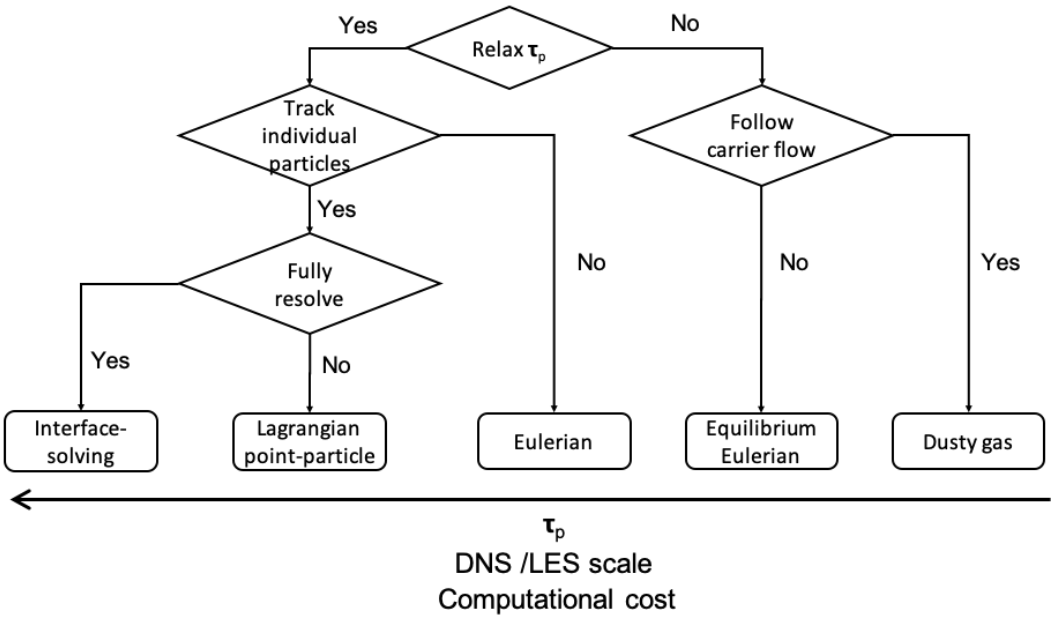

Figure 1.7: Choice of modelling alternatives for the simulation of dispersed phase

the interface-solving approach fully resolves the dynamics of the dispersed phase in turbulent multiphase flows, including the prediction of the interface between the dispersed and continuous phase. This method is considered as the most accurate model and commonly applied to simulate the particles with large scale. However, high computational cost prevents its application to the practical systems with a high amount of particles. And Eulerian, equilibrium Eulerian and dusty gas approaches solve the dispersed phase in Eulerian framework based on assumptions about particle size. These three models are mainly used to predict the flows in practical scenarios and simulate small-scale particles which do not have a disruptive influence on the surrounding fluid. A disadvantage of overlooking physical mechanisms in the dispersed phase limits the application to the system being strongly affected by particles. The Lagrangian point-particle model is a compromising approach between the accuracy and applicability by treating the dispersed phase as point-particle and calculating its dynamics in Lagrangian framework. The main principle of this scheme is based on Maxey-Riley equation [106, 37], where empirical force models are introduced to quantify the momentum exchange between the particles and a carrier fluid. This model has significantly attracted the attention of researchers and much effort has been recently made to enhance its performance [73, 72]. On the other hand, it is important as well to choose proper models solving the continuous phase when applying such algorithms [11]. The large-scale particle usually compels the modellers to incorporate the interface-solving model into direct numerical simulations, while practical flows are commonly predicted by LES models combined with the other four models.

1.3.1 Dusty Gas Approach

Dusty gas model is based on the assumption that dispersed particle size is enough small to follow the local carrier phase, which simplifies multiphase flow into a single-phase flow of which density relies on the local concentration of the dispersed phase. This approach applies the most simplified model for the prediction on the dispersed phase and adopts the concentration transport equation to describe the dispersed phase on the surrounding fluid,

$$\frac{\partial C}{\partial t} + u_i \frac{\partial C}{\partial x_i} = (D + D_t) \frac{\partial^2 C}{\partial x_i^2} \tag{1.61}$$

where C refers to the local concentration of particles, $D_t = \nu_t / Sc_t$ is the sub-grid scale turbulent diffusivity and D is the molecular diffusivity. Sc_t represents the turbulent Schmidt number. Compared to the solution of single-phase flow, the dusty gas model only requires one extra scalar equation and will not lead to a high computational cost. And this model is mostly combined with Boussinesq approximation to solve stratified flows, where density variances are assumed as the raise to buoyancy forces only acting on the source terms of momentum equation, the modified density NS equation employed with the dusty gas approach is as follows,

$$\frac{\partial u_i}{\partial t} + \frac{\partial u_i u_j}{\partial x_j} = -\frac{\partial p}{\partial x_i} + 2\nu \frac{\partial (S_{ij})}{\partial x_j} - \frac{\partial \tau_{ij}}{\partial x_j} + \frac{\rho - \rho_0}{\rho_0} g \tag{1.62}$$

where ρ_0 represents the reference density and ρ refers to the instantaneous density field depending on the local concentration C which is calculated from Eq. 1.61. With simplicity, this model is commonly applied to investigate stratified flows with a small density variance, such as density-driven gravity currents and buoyant plumes in stratified environments. However, there are some limitations on this approach: description of the scalar field is only applicable for particles with a very small size and limited to predict multiple particles; treating the dispersed phase as a passive

field ignores its influence on the carrier fluid.

1.3.2 Equilibrium Eulerian Approach

In order to capture the interaction between the particles and the carrier phase, Equilibrium Eulerian approach firstly adopts the same simplicity as dust gas approach, considering multiphase flows as a one-fluid model, and introduces the particle velocity to account for the inertia of solid particles in a carrier flow. The particle velocity u_p is expressed as follows,

$$u_p = \begin{cases} u_l - St(1-\beta)\frac{Du}{Dt} & \text{if } \mid w \mid \ll St \\ u_l + w - St(1-\beta)\frac{Du}{Dt} & \text{if } \mid w \mid \sim O(St) \\ u_l + w - St\left[(1-\beta)\frac{Du}{Dt} + w \cdot \nabla u\right] & \text{if } \mid w \mid \sim O(1) \end{cases} \tag{1.63}$$

where w is the settling velocity of particle, u_p and u_l represent the velocity of particle and liquid, β can be written as $\beta = 3/(2\rho + 1)$ and refers to the value calculated based on density ratio of particle to liquid $\rho = \rho_p/\rho_l$, St denotes the particle Stokes number representing the scale ratio of dispersed phase to continuous phase,

$$St = \tau_p/\tau_l \tag{1.64}$$

where τ_p and τ_l are the particle timescale and the fluid Kolmogorov timescale, τ_p can be written as,

$$\tau_p = \frac{d_p^2 \rho}{18\nu(1 + 0.15Re^{0.687})} \tag{1.65}$$

where d_p is the diameter of the particle, ν and ρ are the kinematic viscosity and the density of the carrier phase. Equilibrium Eulerian model is capable of simulating the motion of the dispersed phase in a different way from the carrier flow, whereas it

is noted from Eq. 1.63 that the empirical velocity of the particle is highly influenced by Stokes number. And the numerical results show that the Stokes number St of simulated flow should not beyond 0.2 to ensure an accurate prediction, leading to a limitation on predicting the system with a relatively large particle scale to the fluid scales. A typical application of this model is the simulation of turbidity currents, where the suspension of solid particles is modelled as a scalar field and moves by an empirical settling velocity. The numerical results show that the model is able to predict the influence of particles on the surrounding fluid but limited to naturally simulate the interaction between particles within a carrier fluid.

1.3.3 Eulerian Eulerian Approach

Treating multiphase flows as a two-fluid model rather than a one-fluid model, Eulerian Eulerian approach separately forecasts the continuous and dispersed phase in an Eulerian framework by introducing a void fraction variable to compute the coupling and interaction between the two, the governing equation is as follows,

$$\frac{\partial(\alpha_k \rho_k)}{\partial t} + \nabla \cdot (\alpha_k \rho_k u_k) = 0 \tag{1.66}$$

$$\frac{\partial(\alpha_k \rho_k) u_k}{\partial t} + \nabla \cdot (\alpha_k \rho_k u_k \otimes u_k) = -\nabla \cdot (\alpha_k \tau_k) - \alpha_k \nabla p + \alpha_k \rho_k \vec{g} + M_{I,k} \tag{1.67}$$

where u_k refers to a vector representing the velocity in three directions. And α_k is the volume fraction of phase k, where $k = 1$ represents the dispersed phase and $k = 0$ represents the continuous phase. $M_{I,k}$ refers to the interfacial momentum transfer terms which mainly consists of drag and lift force. Different from dusty gas and Equilibrium Eulerian approach, the accuracy of this model is not restricted by stokes number St since the scales of particles' motion and carrier flow are resolved by two separated sets of NS equations. For instance, the lift force acting on a secondary

phase m in a primary phase n can be written as follows,

$$F_L = 0.5\rho_n\alpha_m(u_n - u_m) \times (\nabla \times u_n) \tag{1.68}$$

where α refers to the volume fraction, u and ρ represent velocity field and density. The force is added to the source term of the momentum equation for both phases. Although the unique representation for the dispersed phase makes Eulerian Eulerian model applicable for multiphase flow systems with a high volume fraction of particles, it prevents the model from tracking the dynamics of individual particles. This model is widely applied to investigate turbulent dispersed multiphase flow encountered in practical engineering, such as buoyant exhaust plumes from a vehicle in the atmosphere, buoyant plumes in aeration tanks and gas-solid interactions in a chemical fluidized bed. The results show that Eulerian-Eulerian model under-estimates the turbulence induced by the dispersed phase [100], particularly bubble-induced turbulence (BIT) in the gas-liquid system, and is not able to forecast the plume's interface (i.e., wave interaction and entrainment) and the interaction between the particles [21, 20].

1.3.4 Lagrangian Point-Particle Approach

The point-particle Lagrangian algorithm has been developed over the last 30 years and used to describe the dynamics of the discrete particles individually in Lagrangian framework rather than Eulerian framework, e.g. the mass, momentum and energy of the dispersed phase. This approach is aimed at predicting the trajectory of the particles and naturally understanding the mechanisms of the interface between the continuous and dispersed phase, which has been applied at numerical investigations on bubbly and particle-laden flows. The results show that Eulerian-Lagrangian model is capable of predicting practical bubbly flows better than Eulerian Eulerian

model, accurately simulating the in-plume dynamics including the entrainment of surrounding fluid and the generation of turbulent kinetic energy within the plumes [147, 60]. The earlier developments in this model focus on one-way coupling where the discrete Lagrangian markers are considered as passive and follow the local carrier phase based on the assumption that the particles are rigid and spherical. The motion of each particle is computed by Newton's second law:

$$m_p \frac{\partial u_{p,i}}{\partial t} = F_{p,i} \tag{1.69}$$

where m_p is the mass of particles, $u_{p,i}$ is the particles' velocity in spatial direction i, and $F_{p,i}$ refers to the sum of the interfacial liquid forces acting on the particle in direction i. The integral forces acting on each particle are approximated by semi-empirical formulae, which are buoyancy, fluid stress, added mass, Basset history, drag and lift. The numerical results reveal that passive Lagrangian particles are able to visualize the flow structure of the continuous flow but limited to simulate the motion induced by particles in the flow field.

Interface Coupling Approach

To investigate the significant influence of the particles on the carrier flow, several coupling approaches have been developed to exchange the motion between the phases. A two-way coupling model was developed where the scales of motion by dispersed phase have a disruptive influence on the carrier fluid. When this model is combined with LES approach, the filtered momentum balance equation of the carrier phase is as follows,

$$\frac{\partial u_i}{\partial t} + \frac{\partial u_i u_j}{\partial x_j} = -\frac{\partial p}{\partial x_i} + 2\nu \frac{\partial (S_{ij})}{\partial x_j} - \frac{\partial \tau_{ij}}{\partial x_j} + \xi_i \tag{1.70}$$

Coupling model	One-way	Two-way	Four-way
Semi-empirical formulae	√	√	√
Liquid → Particle	√	√	√
Particle → Liquid		√	√
Particle → Particle			√
Particle's concentration	$\leq 2\%$	$2\% - 5\%$	$\geq 5\%$

Table 1.1: Comparison of Lagrangian coupling approach

where ξ denotes to the source term accounting for the contribution of disperse phase to the continuous fluid. The solution procedure is divided into forward coupling and backward coupling: the former refers that the velocity and position of particles are updated by Eq. 1.69 based on the information from Eulerian framework; the later represents that the influence of particles on the velocity field of the surrounding fluid is computed as source term ξ of Eq. 1.70. The two-way model is capable of capturing the turbulent scales of particles' motion and has been widely applied to predict multiphase flow systems with a low concentration of dispersed phase Φ_p [11]. Four-way coupling scheme is proposed to handle the system with a high volume fraction of discrete Lagrangian particles Φ_p, where the interaction between dispersed phases cannot be ignored and resolved by a proper collision model. Table. 1.1 summarizes the characteristic feature of these three coupling approaches. In general, there are two modelling alternatives accounting for the collision: soft collision and hard collision model. Considering colliding particles as rigid and spherical, the hard approach introduces impulse equations as follows for the interaction between two particles and computes a sequence of collisions to ensure instantaneous collision at a time,

$$P(t) = \int_0^t F_{ab}(\tau) d\tau \tag{1.71}$$

where P is the impulse which is the integral of the contacting force of particle a and particle b F_{ab} over the time interval t. In this model, the restitution coefficient in the normal direction and the friction coefficient in the tangential direction can be simulated with realistic values. On the other hand, the soft approach retains the same simplicity of the hard model, assuming the particles as rigid spheres, and treats the interaction between particles as a mass-spring system which can create a repulsive force when two particles come into contact, a typical system is as follow,

$$F_{n,a\to b}^{col} = \begin{cases} -\lambda\delta_{ab}n_{ab} - \eta u_{ab} & \text{if } d_{ab} < r_a + r_b + \gamma, \\ 0 & \text{else .} \end{cases} \tag{1.72}$$

where n represents the normal component of collision force, γ denotes a stiffness parameter, η is the damping parameter, d_{ab} is the distance between the centres of two particles, δ_{ab} is the overlap between two particles, λ represents influence range to generate a collision force when two particles are close, n_{ab} is the unit vector from the centre of particle a to that of particle b, r_a and r_b are the radii of particle a and b. Compared with the hard model, there is a less required computational cost in the soft model since the sequence of collision is simplified into the extension of spring-damper and the key parameters of the colliding system (restitution and friction coefficient) are modelled by empirical stiffness and damping ratio [75, 34]. A summary of these two collision models is shown in Table. 1.2.

Eulerian-Lagrangian Mapping

When exchanging information between the dispersed and continuous phase, there are two main approaches to quantify the forcing effect: Particle-Source-In-ball (PSI-ball) and Particle-Source-In-cell (PSI-cell). The characteristic of these two methods are schematically expressed in Fig. 1.8 and 1.9. PSI-cell algorithm is based on the

Model	Soft model	Hard model
Particle	Rigid spheres	Rigid spheres
Contacting scheme	One point	One point
Force	Spring-damping system	Impulse equations
Sequence	Not required	Required
Coefficient	Empirical value	Realistic value
Multiple particle	Easy to simulate	Difficult to simulate
Computational cost	cheap	expensive

Table 1.2: Comparison of hard collision and soft collision model

assumption that all the interfacial forces within one computational cell can be expressed as a cumulative force acting on the hosting cell centre or the hosting cell corner nodes. To ensure a fair distribution of forces within the associated Eulerian grid, the dispersed phase size is required to be much smaller than the computational cell. Compared to PSI-cell method, PSI-ball model is more applicable for solving the particles with a relatively larger size than the computational grid. The interphase forces in this approach are redistributed by interpolation function where the influence of forces on Eulerian grid depends on the distance from particles' position to the associated cell corner nodes. Although many novel algorithms are developed to improve the applicability of point-particle Lagrangian model, the model still faces some challenges in terms of forecasting the mechanisms of individual particles. Considering a perfect point-particle Lagrangian force model, the calculation of particles' dynamics should rely on three parts: time evolution of the motion of particle; time evolution of the motion of neighboured particle; time evolution of the surrounding fluid. The first and the third components are embedded in the most of Lagrangian models and the calculation of the second part is a challenging task for the modeller. And the researchers [12] recently realized that the current Lagrangian force models mostly compute the dynamics of one particle without considering one or more of the neighbours which can induce perturbation flow and affect the calculation of forces, particular for drag force.

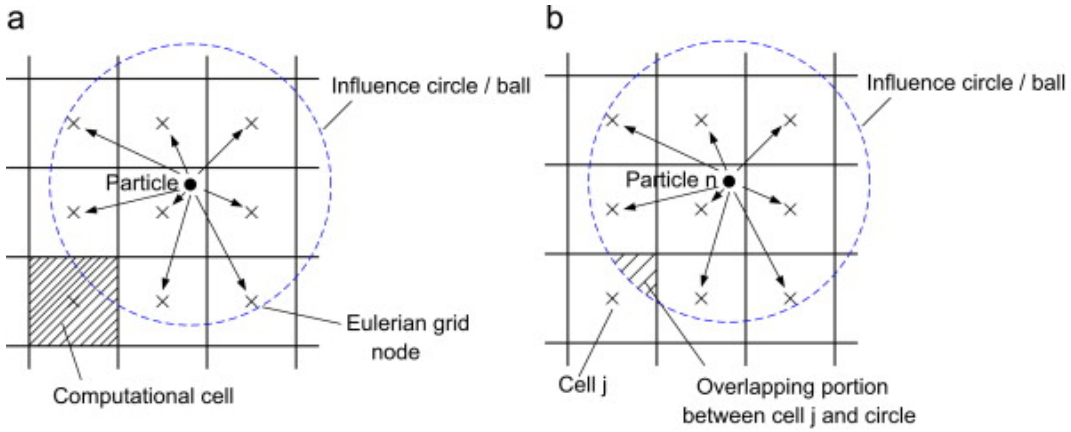

Figure 1.8: Schematic of Particle Source in Ball Method [78]

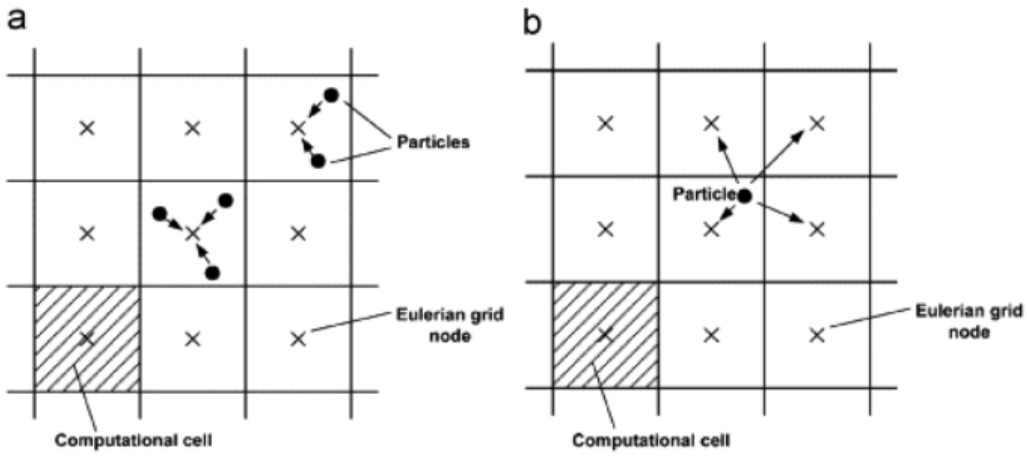

Figure 1.9: Schematic of Particle Source in Cell Method [38]

1.3.5 Interface-Solving Method

Interface-solving (IS) method fully resolves the interaction between the dispersed and continuous phases without modelling. This approach is extremely useful for fundamental research on physical mechanisms of two-phase interaction for particles with a characteristic length above the Kolmogorov scale, such as a single rising gas bubble in liquid. And several algorithms have been applied to track individual particles by IS model, such as volume of fluid (VOF), front tracking (FT) and level-set method (LSM) [155]. Since the small size of particles, these approaches mainly compel the modeller to choose DNS for the continuous phase in order to avoid a larger predicted characteristic length of the flow field. The momentum balance equation combined with IS models is as follows,

$$\frac{\partial}{\partial t}u + u \cdot \nabla u = -\nabla p/\rho - \nu\nabla^2 u + \frac{1}{\rho}f + F_s \tag{1.73}$$

where additional terms F_s is the surface force acting on the interface between the dispersed and continuous phase. When applying VOF model, F_s can be computed as,

$$F_s = 2F\sigma(n \times \nabla) \times n \tag{1.74}$$

where σ is the shear stress and n is the normal vector to the interface, which can be computed by the color function F,

$$n = \nabla F \tag{1.75}$$

IS method is considered as the most accurate approach to simulate the motion of the particles in dispersed multiphase flows. The modellers mostly apply this scheme to investigate the interface between the dispersed and continuous phases as well

as the deformability of particles. The results fundamentally exhibit flow separation, vortex shedding and wake-to-wake interaction induced by the dispersed phase, which are often adopted to validate the accuracy of the empirical forces model in point-particle Lagrangian scheme. However, the high computational cost is a challenge for the application of IS model to a practical multiphase system with a huge number of particles [12].

1.3.6 Contributions to the Numerical Model

In this work, the simulation is carried out by the in-house code solver BubLPT which is developed and incorporated on the finite difference Navier-Stokes solver Hydro3D [60]. The solver applies a two-way coupling point-particle Eulerian-Lagrangian approach to forecast the dynamics of bubbly flows and has been validated by previous research [59]. The proposed work contributes to the further exploitation of the in-house code solver on solving the dispersed phase within Lagrangian framework with regarding its fluid mechanisms and mass transfer. Specifically, the accuracy of the code solver predicting turbulent mixing by multiphase flow is validated versus experimental measurement, showing a close agreement. A multi-source approach is implemented in this work to allow the user of the code solve to set up easily several plumes/screens. These will be described in Section. 3. Moreover, the Boussinesq approximation is implemented in this work to simulate density variable flows (i.e., density-driven gravity currents) and a soft-collision model is implemented to account for the interactive dynamics between the particles, promoting the ability of the code to resolve particle-laden flows by a four-way coupling scheme. More details about numerical implementation and results will be shown in Section. 4. Lastly, Section. 5 will integrate the above implementations and numerically reproduce mass transfer between the dispersed and the continuous phase in a three-phase flow.

1.4 Aims and Objectives of the Thesis

In this Doctoral thesis, an in-house Finite Differences CFD solver has been developed to predict multiphase flows encountered in practical engineering using an LES-based Eulerian-Lagrangian (LES-EL) model. The research is aimed at developing a novel and efficient Eulerian-Lagrangian algorithm capable of predicting dispersed multiphase flows of interest in Civil and Environmental Engineering. Furthermore, this study aligns with the strategic interest in energy, health and mathematical sciences, and in particular with issues such as saving energy and initiatives such as the project Clean Air-Indoor Air Quality Emissions and Modelling System (IAQEMS) led by the University of Birmingham. The outcome of this work is applied to investigate the multi-physics of turbulent dispersed flows, with a focusing on: 1) optimal energetic strategy for distributing aeration devices in chemical and environmental engineering; 2) fundamental insight and theoretical understanding on turbidity currents; 3) mechanisms of the activated sludge process in wastewater treatment plants. These will be achieved by completing the following objectives:

- To validate the accuracy of in-house CFD solver versus experiments in terms of forecasting the turbulent mixing induced by buoyant plumes.
- To model various aeration systems in chemical reactors and determine the optimal configuration design with an efficient mixing performance.
- To develop a numerical strategy for forecasting the multi-physics of particle-laden flows (i.e., turbidity currents) and validate its accuracy versus laboratory measurements.
- To compare particle-driven currents versus continuous density-driven currents.
- To inform a integrated numerical framework capable of predicting three-phase

flows, including mass transfer and dynamic interaction between the different phases.

- To apply the aforementioned three-phase model to develop a novel modelling approach for the integral assessment of the Oxygen transfer in activated sludge process.

1.5 Contribution to Knowledge

It is challenging to simulate particle-laden flows (here particle refers to the dispersed phase and bubble flows is also a particle-laden flow) since the multiplicity of scales of motion and particle-induced turbulence [12, 11]. Extensive numerical investigations have been conducted to understand the mechanisms of turbulent multiphase flows and apply their content to engineering applications. However, the modellers are still facing challenges in terms of validating their model's accuracy and integrating existing algorithms to provide the high-fidelity simulation of practical flows, such as lots of realistic cases that were usually addressed with Eulerian-Eulerian solutions that do not respect the discrete nature of the dispersed phase. [21, 20, 163, 162, 164]. The outcome of this thesis will further validate the proposed in-house multiphase code solver and inform an integrated numerical framework for a tremendous variety of engineering and scientific applications. Turbulent mixing by buoyant plume is commonly applied in practical applications and investigated by designers in order to enhance the mixing efficiency. The recent researches reveal that Eulerian-Lagrangian (EL) algorithms have better capable of forecasting the dynamics of bubble flows [60], while such models require a further validation on predicting the homogeneity of the carrier flow induced by the dispersed phase [17, 42, 41]. This thesis contributes to a numerical solver and validates its accuracy of predicting the mixing efficiency, extending it to assist the detailed design of chemical reactors. Focusing on particle-

laden flows, the researchers intend to develop their numerical models and wish a theoretical understanding on the mechanisms of the turbulent scales driven by particles [50], which is particularly true for the simulation of turbidity currents. The strategy for simulating the dynamics of inertial particles within the currents is currently challenging to propose a compromising model between the proper treatment of the high-concentration dispersed particles and computational cost [23, 117, 11]. Hence, a novel Lagrangian particle tracking algorithm is developed by incorporating with soft-collision model in order to account for the interaction between the inertial particles and its influence on the surrounding continuous fluid. The proposed model is validated in this thesis and applied to bridge the gap between the high-resolution models and the practical, yet empirical-based models. On the other hand, the literature review indicates a lack of effort in forecasting the fluid mechanisms of activated sludge process in wastewater treatment plants, which requires a predictive and practical tool to aid the design of aeration system [84, 82]. This thesis firstly builds up a validated model solving the mass transfer between the phases in multi-phase flows and integrate all the algorithms established in this work, promoting a universal framework to pioneer and optimise the use of aeration devices in environmental engineering. To make a summary of the proposed work, the following major aspects of fluid mechanics will be highlighted and achieved in this study,

- Spatial homogeneity induced by buoyant plumes in gas-liquid flows and its quantification by numerical and experimental approaches.
- Interaction between inertial particles in particle-laden flows and its influence on the turbulent scales within the continuous fluid.
- Boussinesq assumption accounting for the mechanisms generated by density difference in density variable flows.
- Mass transfer among different phases in gas-liquid-solid three-phase flows.

The resulting numerical framework can contribute to practical engineering applications in terms of saving energy and achieving net zero strategy, such as

- Bubble aerators in chemical reactors (various aerator distribution, gas flow rates, air bubble sizes)
- Sedimentation transport in river/ocean (particles settling velocity, volume fraction of particles)
- Activated sludge process in wastewater treatment (various aerator distribution, gas flow rates, air bubble sizes, weather conditions)

1.6 Thesis outline

In general, the work is organized into three journal papers, in part one, the paper is entitled '**Large-Eddy Simulation of Enhanced Mixing with Buoyant Plumes**' and examines Eulerian-Lagrangian model applicable to predict enhanced mixing and diffusivity by bubble-induced turbulence, which is commonly used in practical applications such as chemical reactors and aerators in wastewater treatment plants. Large-eddy simulations of turbulent mixing produced by buoyant plumes and screens are analysed to assess the efficiency of bubble reactors. The solver uses an Eulerian-Lagrangian point-particle algorithm to provide two-way coupling of the liquid and gas phases. The transport of a passive tracer is simulated to visualise the homogeneity of the mixture and the speed of the process. The accuracy of the solver predicting mixing times is successfully validated versus experimental data in a bubble reactor with three different diffuser configurations, exhibiting the first validation on mixing time predicted by Eulerian-Lagrangian model. The numerical results quantify the mixing induced by bubble screens and different arrangements of discrete plumes and

explore the influence of the gas flow rate and the depth of the reactor. Our predictions show significant differences regarding mixing times and energetic efficiency for different aerator setups. For a constant flow rate, bubble screens provide a better performance than combinations of plumes. Our simulations also predict that arranging the gas diffusers as a screen is more efficient than increasing the flow rate. The paper has been published in Chemical Engineering Research and Design [30], where conceptualization, methodology, software, data analysis and writing original draft are done.

In order to extend the application of the code solver to solid particles, the study entitled '**An Eulerian-Lagrangian Approach to Simulate Gravity Currents Driven by Inertial Particles**' moves to develop a pioneering numerical model of solving particle-induced variable density flow, where the wave generated by the bulk movement of particles is resolved in a Lagrangian framework. Hence, the second paper are formulated by applying large-eddy simulation incorporated with Boussinesq approximation to investigate turbidity currents where the currents are driven by inertial solid particles. The solver uses an Eulerian-Lagrangian point-particle algorithm to provide a four-way coupling of the solid particles and the surrounding fluid, with the interaction between particles being handled by a soft-sphere collision model. The accuracy of the solver predicting the front speed of the current is validated versus experimental measurement, showing a good capability of forecasting the motion of inertial particles in the continuous fluid. Comparing with density-driven gravity currents, the numerical results exhibit that the settling of solid particles strongly influences the propagation of the currents and the motion of the coherent structures at the shear layer, as well as the dissipation on energy of the currents. The research successfully provides the application of code solver in environmental flow. The paper is going to be submitted to the Journal of Fluid mechanics, where conceptualization, methodology, software, data analysis and writing original draft are done.

Based on the accurate prediction on turbulent mixing by bubbly flows and particle-driven flows, the third paper is entitled '**A Three-phase Eulerian-Lagrangian Model for Activated Sludge Treatment**' and aimed at developing a novel approach applicable to simulate activated sludge process in wastewater treatment plants. An Eulerian-Lagrangian based on large-eddy simulation model is employed where the wastewater transport equations are resolved in Eulerian framework, suspension of solid particles and buoyant plume are represented as discrete Lagrangian particles. The transport of a passive tracer is simulated to visualize the redistribution of dissolved oxygen induced by the dispersed phases in a carrier fluid. The accuracy of the solver predicting mass transfer between the dispersed and continuous phase is successfully validated versus experimental data in a bubble column with five different superficial velocities, where mesh convergence is analysed. Simulations of solid-gas-liquid three-phase flow are carried out for a real case of the wastewater treatment plant in order to explore the impact of the analyzed factors on oxygen uptake by sludge in a aeration tank. The results show that weather condition has a significant influence on the efficiency of consuming and transferring dissolved oxygen in a carrier fluid. The prediction also presents that bubble screens provide a better performance than a single plume for a constant input energy. This work present to the community a reliable and extendable model that solves the fluid mechanics and the basic eco-hydraulics of the three-phase system encountered in wastewater treatment plants, with minimal empirical inputs. This is a valuable and precise tool to test the operation and design of activated sludge process and similar processes. The paper is submitted to International Journal of Multiphase Flows (under review), where conceptualization, methodology, software, data analysis and writing original draft are done. In conclusion, the aforementioned three papers will show a numerical investigation of particle-laden flows by a novel Eulerian-Lagrangian approach and validate the accuracy of the proposed model versus the laboratory results, while applying the outcome to a wide range of engineering applications.

Chapter 2

Methodology

In this study, the fluid flow is simulated using an enhanced version of the in-house LES-based Lagrangian particle-tracking algorithm BubLPT [59], incorporated on the finite difference LES Navier-Stokes solver Hydro3D [27, 124, 157, 123]. This code has been successfully applied turbulent multiphase flow using LES [30, 60] and DNS [88, 126]. The model has been successfully validated the bubble plume dynamics versus laboratory experiments where compressed air was injected at a constant gas flow rate through an aquarium airstone [60]. The results showed that BubLPT is capable of providing an accurate characterisation of the velocity field across the liquid entrained by the plume, as well as the second-order turbulent statistics in the shear layer at the edge of the plume. These results also reported a consistent underestimation of the vertical turbulent fluctuations at the plume's core due to the lack of the resolution of the individual bubble interface and the vorticity at its wake. Furthermore, B. Fraga et al. [59] extended that work by analysing how plume dynamics affected properties such as liquid entrainment, plume's width or mass and momentum fluxes, providing further successful comparison against a variety of experimental datasets and certifying the robustness of this methodology

against a wide parameter range (gas flow rate, diffuser area), with a particular attention to the key role of bubble size.

2.1 Continuous phase

The governing equations are the spatially filtered Navier-Stokes equations for turbulent, incompressible, three-dimensional flow are described in Eqs. 2.1 and 2.2.

$$\frac{\partial u_i}{\partial x_i} = 0 \tag{2.1}$$

$$\frac{\partial u_i}{\partial t} + \frac{\partial u_i u_j}{\partial x_j} = -\frac{\partial p}{\partial x_i} + 2\nu\frac{\partial (S_{ij})}{\partial x_j} - \frac{\partial \tau_{ij}}{\partial x_j} + \xi_i \qquad (for\ \ i = 1, 2, 3) \tag{2.2}$$

where u_i and x_i refer to the fluid velocity and position in the i Cartesian coordinate, respectively. t, p, ν and S_{ij} represent time, dynamic pressure, kinematic viscosity and strain rate tensor. The term τ is the sub-grid stress and is calculated by the turbulent viscosity ν_t, herein based on the Smagorinsky sub-grid scale (SGS) model with a constant coefficient $C_S = 0.1$. Finally, $\xi = \xi_s + \xi_g$ designates the source term that accounts for the contribution of the dispersed phases (e.g., inertial solid flocs ξ_s and buoyant gas bubbles ξ_s, see more details in Section. 5) to the flow's momentum. The time derivatives are discretised using a three-step Runge-Kutta algorithm and a second-order central difference scheme is applied to both convective and diffusive terms. The code is based on a predictor-corrector fractional step method with the solution of the Poisson pressure equation obtained through a multi-grid solver.

In order to quantify bubble-induced mixing (see Section. 3), track the heavier fluid in density-variable flows (see Section. 4) and predict the fate of dissolved oxygen

in wastewater (see Section. 5), the transport of scalar field is simulated on the Eulerian grid by solving a filtered advection-diffusion Eq. 2.3. The filtered scalar equation is solved at each time step once the continuous phase and its coupling with the dispersed phases is calculated.

$$\frac{\partial C}{\partial t} + u_i \frac{\partial C}{\partial x_i} = (D + D_t) \frac{\partial^2 C}{\partial x_i^2} \tag{2.3}$$

where C is the tracer concentration, $D_t = \nu_t / Sc_t$ is the sub-grid scale turbulent diffusivity and D is the molecular diffusivity. Sc_t represents the turbulent Schmidt number and has a value of 0.7, as adopted in similar studies [124, 87, 70]. When solving a scalar filed that can act as an active tracer influencing the continuous phase, the Boussinesq approximation is applied to induce the density variance within the current, the modified momentum equation is as follows,

$$\frac{\partial u_i}{\partial t} + \frac{\partial u_i u_j}{\partial x_j} = -\frac{\partial p}{\partial x_i} + 2\nu \frac{\partial (S_{ij})}{\partial x_j} - \frac{\partial \tau_{ij}}{\partial x_j} + \frac{\rho - \rho_0}{\rho_0} g + \xi_i \tag{2.4}$$

where ρ_0 represents the reference density and ρ refers to the instantaneous density field of the carrier fluid. The latter is a function of the local concentration field C and will be updated once the active scalar is solved. For instance, the relationship between the density and the concentration can be adopted as $\rho = 0.007587C + 0.9947(g/cm^3)$ based on saltwater at 25 Celsius, in order to simulate density-driven gravity currents (see Section. 4)

2.2 Dispersed phase: gas bubbles and sludge particles

The dispersed phase is simulated using a Lagrangian Particle Tracking algorithm in which each particle is represented by a single point that moves in Lagrangian coordinates. In this work, three-phase and two-phase flows are analysed including

liquid, gas and solid phase, where the gas and solid volume fraction is estimated as 0.06% and 2.0% respectively. Hence, a two-way coupling approach is proposed to calculate the dynamics of the dispersed gas phase and quantify the contribution of the gas phase to the carrier flow based on computing interfacial forces on the Eulerian framework. Due to the high concentration of solid particles, a four-way coupling approach is applied to predict the dynamics of the particles and particle-to-particle collision as well as the interaction with the liquid. Based on the assumption that the dispersed phase (bubbles and solid particles, henceforth 'particles') are rigid and spherical, the motion of each particle is computed by Newton's second law:

$$m_p \frac{\partial v_{p,i}}{\partial t} = F_{p,i} \tag{2.5}$$

where m_p refers to the mass of the particle, $v_{p,i}$ refers to the particle's velocity in spatial direction i, and $F_{p,i}$ refers to the sum of the interfacial liquid forces acting on the particle in direction i. The integral forces acting on each particle are approximated by semi-empirical formulae, which are buoyancy, fluid stress, added mass, drag and lift, whose expressions are shown in Table. 2.1. The subscript p denotes particle (dispersed phase) whereas l indicates liquid (continuous phase). Stokes drag is considered when very small particles move through the carrier phase at a relatively slow velocity (low Reynolds number Re < 1) where there is a laminar regime [55, 76]. This model assumes that the drag force is proportional to velocity and its mathematical expression is,

$$F_{SD} = m_p \frac{u_p - u_l}{\tau_p} \tag{2.6}$$

where τ_p refers to the particle relaxation time, which can be defined as

$$\tau_p = \frac{d_p^2}{18\mu}(1 + 0.15Re_p^{0.687})^{-1} \tag{2.7}$$

Forces	Formulation
Buoyancy	$F_G = (m_p - m_l)g$
Fluid stress	$F_S = m_l \frac{Du_l}{Dt}$
Added mass	$F_A = -C_A m_l \frac{\partial}{\partial t}(u_p - u_l)$
Drag	$F_D = \frac{1}{2} C_D \rho A_{fr} \mid u_p - u_l \mid (u_p - u_l)$
Lift	$F_L = -C_L m_p (u_p - u_l) \times \omega_l$

Table 2.1: Interfacial liquid forces acting on the particle in the PPL-LES model.

and Re_p represents the local Reynolds number for the particles $Re_p = \frac{|u_p - u_l| d_p}{\mu}$.

In order to prevent overlap between particles in turbidity currents wherever the solid fraction becomes dense, the soft-sphere collision model developed by [39] is applied in this work to predict particle-to-particle and particle-to-wall interactions. This model is based on the assumption that the particles are spherical and treats the interactions between particles as a mass-spring system which can create a repulsive force when two particles a, b come into contact. The collision force $F_{n,a\to b}$ exerted on the particle b due to the collision between the two can be expressed as follow,

$$F^{col}_{n,a\to b} = \begin{cases} -\lambda \delta_{ab} n_{ab} - \eta u_{ab} & \text{if } d_{ab} < r_a + r_b + \gamma, \\ 0 & \text{else .} \end{cases} \tag{2.8}$$

where n represents the normal component of collision force, γ denotes a stiffness parameter, η is the damping parameter, d_{ab} is the distance between the centers of two particles, δ_{ab} is the overlap between the two particles, λ represents the particle's influence range, n_{ab} is the unit vector that unites the center of particles' a and b and r_a and r_b are the radii of particles a and b. The relative normal velocity u_{ab} between two particles is defined as

$$u_{ab,n} = ((u_a - u_b) \cdot n_{ab}) n_{ab} \tag{2.9}$$

The damping parameter of the collision model η is used in this model to account for the energy dissipation in mass-spring system, which can be solved with the coefficient of restitution e (0 <e< 1) and the effective mass $m_{ab} = (1/m_a + 1/m_b)^{-1}$,

$$\eta = -2lne\frac{\sqrt{m_{ab}k}}{\pi^2 + (lne)^2} \tag{2.10}$$

The stiffness parameter γ is applied to quantify the resistance force under deformation and is expressed as

$$\gamma = \frac{m_{ab}}{\tau_{col}^2}(\pi^2 + ln(e)^2) \tag{2.11}$$

where τ_{col} refers to the collision time accounting for the resolution of collision. The collisions with the wall are modeled by treating the wall as a particle with infinite mass and zero radius. The influence range λ is defined as follows to avoid the close-packing limit and the collisions between particles with high speed,

$$\lambda_{wall} = 0.75\, CFL_{ab}^{col} d_{eff} \tag{2.12}$$

$$\lambda_{particle} = 0.375\, CFL_{ab}^{col} d_{eff} \tag{2.13}$$

where d_{eff} is the effective particle diameter ($d_{eff} = r_a + r_b$) and CFL_{ab}^{col} denotes the collision Courant-Friedrichs-Lewy (CFL) number that is typically set as 0.1 for particle-wall collisions and 0.2 for particle-particle collisions [23].

In order to simulate the friction between two particles and the rotation of particles, a simplified static fraction model suggested by [23] is employed. The tangential displacement of two particles is theoretically calculated as follow,

$$\delta_t = \delta_{t1} + \int_{t_1}^{t} u_{ab,t} dt \tag{2.14}$$

where $u_{ab,n}$ represents relative tangential velocity between two particles and δ_{t1} refers to the starting stage of the collision. The time integration from t_1 to t quantifies the displacement in tangential direction and highly requires computational resource to store the information of particles under sustained collision. Thus, the simplified model neglects this term, which has been validated in previous studies [23]. The formula can be defined as follow,

$$F_{t,a\to b}^{col} = -\mu_f \mid F_{n,a\to b}^{col} \mid t_{ab} \tag{2.15}$$

where t represents the tangential component of collision force, μ_f refers to the friction coefficient and t_{ab} refers to a tangential unit vector that can be calculated by the relative tangential velocity $t_{ab} = \frac{u_{ab}-u_{ab,n}}{|u_{ab}-u_{ab,n}|}$.

Particle-to-particle interaction is often rather prohibitive due to the necessity of tracking and checking the likelihood of collision among all particles. In this work, considering the usual particle velocities and solid fraction, we assumed that the possibility of collision is restricted to the particles within the same Eulerian cell (i_p, j_p, k_p). For each cell, the number of particles in it is stored and used for the collision loop over all particles only within that cell. In addition, each MPI block will also track the positions and velocities of the 'ghost particles' in the first few layer of cells of the neighbour block.

2.3 Interphase mass transfer

To simulate the oxygen exchange between the air bubbles (see Section. 5) and the liquid phase, the model developed by [43] is adopted. Within this model, the interphase mass transfer is driven by mass fraction gradients; the mass transfer rate of

oxygen $\dot{m}_b(mg/s)$ can be expressed as

$$\dot{m}_b = Ek_l A_b \rho_l (Y_l^* - Y_l) \tag{2.16}$$

where E designates an enhancement factor caused by chemical reactions, A_b is the surface area of the air bubble and k_l represents the mass transfer coefficient for oxygen [114]. Y_l^* and Y_l refer to the mass fraction of oxygen at the gas-liquid interface and in the liquid phase respectively. The former is obtained from the oxygen mass fraction in the bubble Y_b:

$$Y_l^* = HY_b \frac{\rho_b}{\rho_l} \tag{2.17}$$

where H represents the Henry constant accounting for the relationship between the amount of gas into a liquid and the pressure above the liquid. The oxygen is regarded as the gas phase in this work and the corresponding Henry constant is adopted as 0.0032 based on water at 25 Celsius [140]. Thus, the oxygen transfer from the liquid phase to the gas phase can be described as $m_{l\to b} = max(\dot{m}_b, 0)$ and the oxygen transfer from the bubble to the liquid phase can be described as $m_{b\to l} = max(-\dot{m}_b, 0)$.

The sludge particles consume the dissolved oxygen in the tank during activation. In ASP, the DO consumption is strongly affected by microorganism (aerobic bacteria) and sludge concentration [146]; this process mainly consists of four phases: 1) aeration-driven mixing provides a homogeneous DO for sludge growth; 2) biological degradation of the organic matter by activated sludge and continuous growth of sludge, where DO consumption rate retains a high level; 3) ends with a limitation on the growth of DO use rate by the decrease on the concentration of the organic matter since this rate highly depends on the remaining organic matter concentration and decreases until oxidisable flocks (including organic matter) settle out; 4) DO is

only consumed by the sludge since all organic matter has been removed. This work will focus on the first two phases by using the relationship between sludge concentration (S_c) and unit oxygen uptake rate (OUR). The latter is calculated using the empirical model developed by [120] (Eq. 2.18), which follows the assumption that the organism concentration is high level and therefore cannot act as a limiting factor in DO consumption.

$$OUR = 16.9492 - 0.0018 \times S_C \tag{2.18}$$

It is necessary to account for the local DO level around the solid particles (activated sludge) when calculating the DO uptake by each particle. The modified equation is,

$$OU^j_{l\to s} = \begin{cases} OUR \times \Delta t & \text{if } OUR \times \Delta t \leq OU^j_l, \\ OU^j_l & \text{if } OUR \times \Delta t > OU^j_l. \end{cases} \tag{2.19}$$

where $OU^j_{l\to s}$ refers to the oxygen transfer from the liquid phase to the sludge j at Δt time and OU^j_l refers to the oxygen levels of the fluid around sludge j at Δt time. The oxygen transfer from the sludge j to the liquid phase can be written as $OU^j_{s\to l} = -OU^j_{l\to s}$. The aim of Eq. 2.19 is to avoid the over-consumption of sludge in the area of which oxygen levels is smaller than the required amount by sludge.

2.4 Rheology modelling

Based on literature review in Section. 5, activated sludge observes a rheological, non-Newtonian behaviour. Our modelling approach does not consider sludge as a continuum, but the interaction of a dispersed solid phase (sludge flocs) and continuum water. The rheological characteristics of sludge manifest in the influence of

the particle suspension on the surrounding liquid's viscosity. The Einstein equation (Eq. 2.20) can be employed to relate the particle concentration to the overall viscosity of the mixture when the concentration of sludge is small and particle-to-particle interaction has no effect on the shear between liquids [57, 128, 51].

$$\nu = \nu_0(1 + 2.5\phi) \tag{2.20}$$

where ν and ν_0 represent the suspension and the solvent kinematic viscosities, and ϕ refers to the local volume fraction of solid particles. In order to calculate ϕ in each cell, a cube of which size depends on the particle diameter is defined for each particle,

$$d_{cube} = d_p\gamma \tag{2.21}$$

where the minimum of the γ representing the ratio of cube size to particle size is equal to $(\pi/6)^{1/3}$ to ensure that the volume of cube is greater or equal to the volume of particle [96]. And the volume fraction in each cube ϕ_{cube} is calculated as follows,

$$\phi_{cube} = \frac{V_p}{V_{cube}} = \frac{\pi}{6\gamma^3} \tag{2.22}$$

which is used to compute the volume fraction of solid particle in cell j,

$$\phi^j_{cell} = 1 - \phi_{cube} \sum_{\forall i \in cell} \Phi^i_{cell} \tag{2.23}$$

where Φ^i_{cell} refers to the volume fraction of the cell j under the consideration of cube i. Thus, the viscosity of each Eulerian cell is updated in each time step based on Eq. 2.20 and the position of each Lagrangian solid particle (sludge).

2.5 Eulerian-to-Lagrangian mapping

When applying the code solver to predict particle-laden flows, a two-way coupling mapping scheme is chosen to exchange information twice between the dispersed phase and carrier phase, which has been successfully validated by previous works [59]. First, the particle velocity is updated using Eq. 2.5 and the new position of each particle can be obtained. This is called forward coupling. Second, the contribution of the particles to the velocity field of the surrounding fluid is computed and represented as source terms ξ of Eq. 2.2, while density field of the carrier fluid is simultaneously calculated based on the information of each particle. This is called backward coupling. In order to accurately define the Eulerian area influenced by particles, the PSI-ball approach developed by [78] is combined with the smoothed delta functions developed by [167] to transfer Eulerian-to-Lagrangian quantities, as proposed by [59]. And the delta function is expressed as follow and with a variable interpolation stencil dependant on the bubble size to Eulerian mesh size $D_p/\Delta x$ ratio as described and tested in detail [60]. ,

$$\delta(x_p - x_j) = \frac{1}{h^3}\phi(\frac{x_p - x_j}{h})\phi(\frac{y_p - y_j}{h})\phi(\frac{z_p - z_j}{h}) \tag{2.24}$$

where δ refers to the delta function and h represents the filtered size, the subscript j denotes to the node in Eulerian framework and p refers to the particles. One demonstration case about this approach will be explained in Section 4, where the general solution procedure for particle-driven gravity currents is summarized as follows,

- Step1: Calculate the density field based on volume fraction ϕ^n at the current time step n using the positions of particles from the previous time step $n-1$
- Step2: Obtain the Eulerian velocities by Eq. 2.4 for each particle at the current time step n by Eulerian-Lagrangian interpolation (see Eq. 2.24)

- Step3: Update the Lagrangian velocities of the particles at current the time step n based on interfacial liquid forces
- Step4: Collision model accounting for particle-to-particle interaction
- Step5: Apply updated Lagrangian velocities to calculate reaction forces being added as the source terms of Eq. 2.2 and obtain the new Eulerian velocity for the next time $n+1$
- Step6: Obtain the new local solid fraction ϕ^{n+1} to update new density field for the next time step $n+1$ once particle movement is updated

By considering interphase oxygen transfer (see Section. 5), the step1 can be tweaked as calculating the oxygen content of each particle by Eqs. 2.16-2.19 in each time step (forward coupling). And dissolved oxygen concentration of the carrier fluid is simultaneously calculated by Eqs. 2.16-2.19 in the Step5 (backwards coupling).

2.6 High performance computing

In this code solver, the calculation procedure for every time step is split among several cores using Message Passing Interface (MPI) parallelisation that also uses a master-slave algorithm to track the Lagrangian particles [123]. All the simulations carried out in each section are supported by several high performance computing (HPC) systems. The HPC Midlands Plus is a Tier-2 high performance computing centre with a focus on Engineering and Physical Sciences, funded by EPSRC in late 2016. This HPC system is consisted of 512 compute nodes in Huawei X6000 quad-node chassis, each with 28 cores. The BlueBEAR is the University supercomputer applied for high performance computing and high throughput computing. This system is mainly consisted of 60 compute nodes with 72 cores, 70 compute nodes with

40 cores and 50 compute nodes with 20 cores. The ARCHER2 is the national supercomputer and a world class advanced computing resource for UK researchers. This system is consisted of 5,860 compute nodes with 64 cores. In Section. 3, the simulations are undertook by HPC Midlands Plus with 150 cores (6 nodes and 25 cores per node), which took four days (physical time) to run half an hour (computational time). In Section. 4, the simulations are performed in BlueBEAR/HPC Midlands Plus with 192 CPU cores (12 nodes and 16 cores per node), costing two days (physical time) to run 10 seconds (computational time). In Section. 5, the simulations are conducted by BlueBEAR/ARCHER2 with 128 cores (8 nodes and 16 cores per node), costing 10 hours (physical time) to run 10 minutes (computational time).

Chapter 3

Large-Eddy Simulation of Enhanced Mixing with Buoyant Plumes

The work is presented in UK Fluid Conference 2019 and UKACM Conference 2020.

Chemical Engineering Research and Design

Submitted 23 July 2021

Accepted 7 November 2021

Available online 12 November 2021

CRediT authorship contribution statement:

1. Literature review on experimental research with the aim of validating the accuracy of code solver to predict mixing time.

2. Implement the code that allows users to simulate bubble screen in water tank.

3. Design numerical simulations for validation of mixing time and sensitivity analysis on mixing efficiency.

4. Post-process numerical results and compare them wih experimerntal measurements.

5. Draft the original manuscript, review and edit it.

3.1 Introduction

Buoyancy-driven gas bubbles are capable of entraining surrounding liquid during their rise, establishing plumes and causing agitation. Many industrial applications use bubble plumes to promote mixing of species in chemical or biological reactors and separators. Thermal diffusion driven by bubbly flows is of key importance in the design of light-water nuclear reactors and thermal power plants. In environmental engineering, aerators and bubble mixers are employed to avoid stratification and algae blooms and break stratification in lakes and reservoirs. Secondary treatment of activated sludge systems consists on pumping air into large basins filled with wastewater, promoting the mixing and redistribution of the dissolved oxygen to facilitate the microbial growth, forming flocks which can easily settle out [28]. Aeration accounts for 60% of total energy consumption in activated sludge systems [131, 54], being the largest operational expense [137, 101].

Turbulent mixing driven by buoyant plumes is a complex multiphase flow phenomenon implicating a wide range of scales of motion [119]. It is necessary to predict accurately the shear layers generated by the individual plumes in order to describe the formation of recirculation cells within the mixing tank, column or reactor, while simultaneously forecasting the in-plume dynamics in order to predict the entrainment of surrounding fluid and the generation of turbulent kinetic energy within the bubble swarm. It is important as well to characterise instantaneous flow properties since unsteady plume wandering and in-plume intermittency contribute to the mixing process. These features make overall physical and mathematical modelling of these processes challenging. Extensive laboratory experiments have been conducted to study the dynamics of mixing induced by buoyant plumes, and mostly monitored velocity field by Particle Image Velocimetry (PIV) and visualized the mixing by injecting a dye tracer [144, 130]. Such experiments were mainly implemented in

chemical reactors where water was used as the continuous phase and air bubbles were released from the bottom through porous aeration pads [170]. The mixing time was determined by allocating probes in bubble reactors and monitoring the evolution of the tracer (dye) concentration [168, 102, 5]. Overall, experimental results show a quick homogenisation of the tracer caused by bubble-induced turbulent mixing. These real-scale mixing experiments investigate a limited number of design alternatives, and are often used by modellers to validate their predictions [135].

From a modelling perspective, an accurate treatment of the continuous and dispersed phases as well as the coupling and interaction between the two is critical to provide accurate predictions. Regarding the turbulence closure for the continuous phase, there are three fundamental modelling alternatives: Direct Numerical Simulation (DNS), Large Eddy Simulation (LES) and Reynolds-Averaged Navier-Stokes simulation (RANS). DNS is acknowledged as the most accurate approach, but to solve all the turbulence scales involved in bubble plumes prevents its application to practical scenarios due to its high computational cost, that strongly limits the gas flow rates that can be investigated [141]. RANS or Unsteady-RANS have been the most common approach to predict aerated flows until the last decade; RANS-based simulations provide a good compromise for practical applications by introducing closure models to account for the turbulent fluctuations [8]. However, the assumption of isotropic turbulence embedded in the most popular RANS models is rather unnatural for dispersed bubbly flows, resulting in a higher gas hold-up and liquid velocity in the plume's core and leading to an underestimation on eddy structures near the wall [17]. Specific models for bubble-induced turbulence exist, yet their wide-range application has not proven to be significantly better than isotropic models [100]. LES can explicitly capture plume-scale turbulent structures in dispersed bubbly flows, reducing the relative influence of sub-grid scale (SGS) turbulence closures upon the predictions [59, 47].

Regarding the dispersed gas phase, the prediction of bubble motion and their interaction with the liquid can be compartmentalised within three approaches: interface-solving methods (IS), point-particle (PP) Eulerian-Lagrangian (EL) algorithms and continuous Eulerian-Eulerian (EE) models. IS models are extremely useful for fundamental research on physical mechanisms of two-phase interaction for particles with characteristic lengths d_p above the Kolmogorov scale η [11]. Several families of algorithms have been applied to investigate the behavior of a single rising gas bubble, such as volume of fluid (VOF), front tracking (FT) and level-set methods (LSM) [155]. For milimiter-sized bubbles, IS methods often compel the modeller to use DNS on the continuous phase, due to their relatively small size compared to the characteristic lengths of the plume/jet [148]. Hence the high computational cost of IS limits its practical application [169, 99]. EE approaches compute the continuous and dispersed phase in a common Eulerian framework, introducing a void fraction variable to simulate the interaction between the two [93], and has been applied successfully to many multiphase flows [53, 48]. Recent investigations reveal that EE models can generally capture the dynamics of bubbly flow at the liquid level [138, 152, 93, 46], while the lack of physical details of the bubble dynamics and liquid-bubble interaction should be considered, since the assumption that the dispersed phase can be represented by a unique field prevents EE models from tracking individual bubbles and their effect on the carrier phase [77]. Moreover, EE models struggle to simulate the effect of polydispersed distributions with a wide range of sizes [11]. PP-EL models respect the discrete nature of the dispersed phase and do not impose additional assumptions on the size distribution of the bubbles or the particle Reynolds number Re_p by treating each phase under different paradigms. The continuous liquid matrix is calculated on an Eulerian framework, whereas the dispersed phase is computed as discrete Lagrangian markers [149]. EL models have been widely applied in the research on multiphase flows [59, 60, 20, 46] and are able to describe the mass, momentum and energy of each dispersed element rather

than throughout a concentration variable. The way in which the interaction between both phases is modelled depends on the particle size and concentration (i.e., the bubble diameter and void fraction for gas bubbles). Due to the high density ratio between air bubbles and water, these flows can rarely be represented through one-way coupling (where the advection of the carrier flow is dominant and the dispersed phase behaves in a nearly passive manner). Bubble buoyancy has a rather disruptive effect on the surrounding liquid, requiring a two-way coupling approach. This is acceptable for dilute bubble concentrations, while very high void fractions require considering bubble-to-bubble interaction (four-way coupling) [77, 109].

Several works have applied three-dimensional non-hydrostatic CFD to investigate applications of bubbly flows to mixing, e.g. aerobic tanks and chemical reactors. Such works were concerned with buoyancy-driven mixing, the turbulence generated by the dispersed phase and the optimal design of the aeration system [136, 164, 163, 69, 111]. The research conducted by [17] tested the ability of RANS models to predict the mechanical mixing in anaerobic digester. By comparison with experimental measurements, the calculated overall power consumption shows to be strongly affected by the choice of turbulence closure. In order to obtain more insight into the mechanisms of mixing, B. Wu et al. [162] used RANS to estimate the mixing time in a cylindrical tank with four baffles agitating water. The comparison on the mixing efficiency achieved by different design of system exhibits that the design of system is of great importance for the mixing performance. Moreover, the author validated the simulated mixing time with experimental measurements, which shows that the mixing time is under-predicted by the turbulence model and the model requires more validations on velocity field to prove the accuracy. Furthermore, V. V. Buwa et al. [21] explored mixing by buoyant plumes in chemical reactors by using a RANS-based EE algorithm. The authors initially compared predicted dynamics of bubble plume with experimental measurements, exhibiting a under-prediction on

gas-hold-up and liquid velocity. They simulated the evolution of passive tracer to predict the mixing time within the reactor, finding that it was highly reliant on the turbulence model. D. D. McClure et al. [107] used the same EE-RANS approach to study mixing in a bubble column reactor and analyse the factors influencing the predicted mixing time. They validated their numerical results with experimental measurements and found that EE-RANS under-predicted the effect of gas flow rate on mixing time. In addition, the results indicated an overall over-prediction of the mixing time, which they attribute to lack of detail reproducing the entrainment within the bubble swarm. The investigation by [83] optimised a EE-RANS model to predict mixing by comparing the liquid's velocity field, air velocity, gas-hold-up and air volume fraction in an aerated tank between numerical and experimental datasets. This work discusses limitations of the turbulence closures and modelling assumptions adopted and concluded that current numerical models need to enhance the interaction between the dispersed phase and the generation of turbulence. In addition, the results showed that the treatment of the dispersed phase is the major factor affecting the prediction of hydrodynamics in bubbly flow - parameters such as bubble size and phenomena such as bubble coalescence and breakup. Two recent numerical studies by [42, 41] applied PP Eulerian-Lagrangian algorithms based on RANS to predict mixing in anaerobic digesters. They modelled one plume in the tank to forecast the velocity magnitude and average shear rate and compared their predictions to experimental results. The comparisons showed how flow patterns are highly influenced by the bubble size and the gas flow rate. Based on these results, they suggested a new arrangement of diffusers to improve mixing quality. These prior studies reveal a wide application of EE-RANS to buoyancy-driven mixing, and how their accuracy highly relies on the turbulence model, often resulting in under-predictions of the velocity field and the mixing performance [65, 49]. Furthermore, recent research has demonstrated that bubble-induced turbulence is not well captured by standard nor specialised turbulence closures, taxing modelling approaches

with heavy reliance on them [100]. Comparison between EL and EE frameworks concluded that the former provide better predictions of the bubble swarm dynamics and the mixing [94, 2] within RANS models. In addition, a critical analysis of the literature focused on the modelling of buoyancy-driven mixing reveals how current validation primarily focuses on the time-averaged velocity fields, without considering the mixing performance itself, which is affected by the instantaneous properties and turbulence structure.

In this paper, an in-house point-particle Eulerian-Lagrangian LES solver developed by [60] is used to gain insight on buoyancy-driven mixing, using a scalar concentration field driven by a convection-diffusion transport equation to simulate the fate of a passive tracer in the tank. The solver's accuracy predicting bubble plume dynamics has been validated in the past, exhibiting a very close prediction of the velocity field, entrainment and second-order statistics [60, 59]. This work will further validate the ability of the model to accurately predict the mixing time of the passive tracer. The paper also analyses the effect of different bubble sizes, bubble-to-grid ratios and gas flow rate on the tracer's mixing. Moreover, it investigates how different setups of the air supply system (diffuser spacing and arrangement) affect the quality of the final mixing and the efficiency of the process.

3.2 Experimental validation of the mixing time in a bubble reactor

The ability of this model to predict turbulent mixing induced by aerators is tested against the experimental measurements performed by [3]. The experiments were carried out in a 0.3 m diameter cylindrical glass column filled with water. The height of liquid is set to 0.53 m at the beginning of each experiment. Concerning air

injection, three types of distributor plates have been considered. They were built on a plane plate of 0.25 m of diameter, drilled with 36 holes of 0.001 m diameter equally spaced following a gap of 0.04 m. The first configuration tested uses the entire plate with all its holes. In the second distributor, 30 holes have been clogged up using tape to allow air flow only through a central ring of 6 holes. The third distributor involves only 15 holes on one half of the plate. A dye tracer is injected after flow stabilisation at the centre of the column, 0.09 m above the perforated bottom plate. More experimental details can be found in [3].

In the experiments, colorimetric method was used to measure mixing times [4]. After flow stabilisation, dye volumes of 0.025% of the total volume are introduced by an injection device located at the centre of the column and the releasing point is at 0.09 m above the perforated bottom plate [3]. A camera is used to record the dye injection and its mixing. The pictures are divided into 6 windows, whose size is 1 cm^2 [3]. The mean grey level inside each window is computed and normalised between 0 and 1. The variance can be expressed mathematically,

$$log\sigma^2_{RMS} = -log\{\frac{1}{np}\sum_{i=1}^{np}(S_i - 1)^2\} \tag{3.1}$$

where np is the number of probes and S_i is the normalised tracer concentration measured at the probe i. Mixing was considered when $log\sigma^2_{RMS} = -2.6$, representing an average standard deviation of 5% from the final concentration [64].

In order to validate the ability of our algorithm predicting mixing time, the experiment has been replicated in numerical simulations whose details are shown in Tab. 3.1. The computational domain is a cylindrical tank; the prescribed initial gas flow rates range, as they do in the experiments, between 0.1 and 2.0 m^3/h. Bubbles are initially distributed over the area of the diffuser where the wholes are, according to the three types of distributor in the experiment, and they are removed

Number of holes in the diffusers	6, 15, 36
Reactor height	0.53 m
Reactor diameter	0.30 m
Gas flow rates	0.1, 0.25, 0.5, 1.0, 2.0 m^3/h
Average bubble size	5.6 mm monodisp., 5.2-6.0 mm polidisp.
Numerical time step	10^{-3} s
Numerical grid size	3.125, 5, 6.25 mm
Number of numerical probes	5, 50

Table 3.1: Range of simulation parameters numerically tested following the experiments by [3].

from the computational domain once they reach the water surface. No-slip boundary condition is applied at the solid walls and the bottom of the tank and a rigid lid is set at the water surface with a free slip condition on the velocity field. The passive tracer is injected at the same point in space and time and with the same concentration specified in the experiments.The numerical probes are located in the middle plane of the tank and monitor instantaneous tracer concentrations on a 1 cm^2 area each. Following the experimental approach, the variance of the tracer's concentration (Eq. 3.1) is computed at each of the probes for every time step and normalised by the average tracer concentration in the tank. Unless specified otherwise, all the results were obtained with the medium 5 mm uniform numerical grid, 50 numerical probes and a monodispersed distribution of bubbles with a diameter of $D_p = 5.6mm$.

Fig. 3.1 shows the time evolution of Eq. 3.1 predicted by the numerical model at five gas flow rates for the 6-hole distributor. In general, the variance of the tracer concentration experiences an abrupt decrease at the start of the simulation. This close-to-vertical decrease relaxes very quickly for high flow rates and more gradually for the lower ones, after which the trend becomes nearly horizontal with a mild negative slope. The black dot line represents the theoretical homogeinity threshold that is used to define the mixing time $log\sigma^2_{RMS} = -2.6$. The point at which the

curve obtained from averaging all the probes readings crosses the -2.6 threshold for the last time (in case it fluctuates around this value) is taken as the mixing time. The final predicted mixing time is obtained by deducting the first 4 seconds of flow stabilisation before the tracer injection and shown in Fig. 3.1.

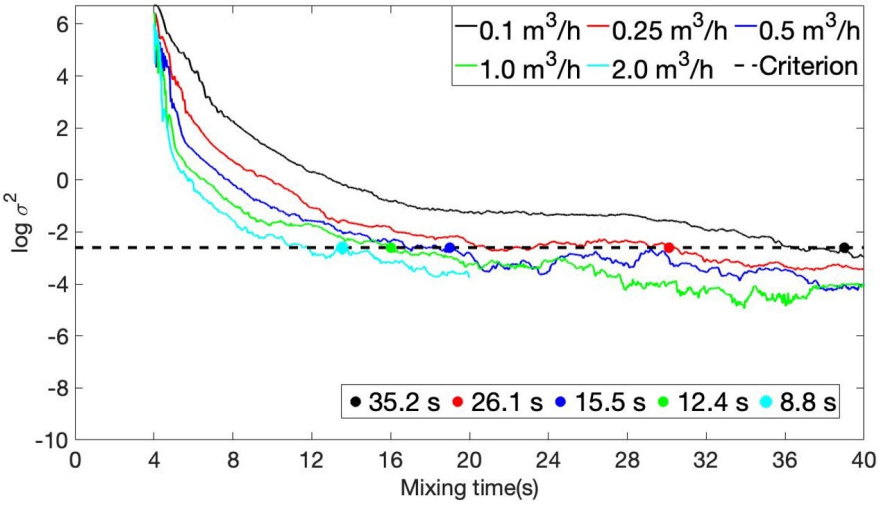

Figure 3.1: Time series of the tracer concentration for 6-hole distributor in the cylindrical tank.

Fig. 3.2 compares numerical and experimental predictions of mixing times for each distributor and flow rate, with triangles representing the mixing time measured in the experiments, including a ±3s margin of error reported by the authors (which might appear at first glance skewed due to the logarithmic scale), and circles correspond to the numerical simulation. The layout of the hole distribution for each blower is shown above the results. There is a very close agreement between the experimental measurements and BubLPT predictions for the three types of distributor and five different gas flow rates. The numerical predictions always fall within the experimental accuracy range and are consistent across the range of parameters considered (flow rate and hole distribution). For each distributor, increasing the gas flow rate induces higher entrainment, liquid velocities and agitation. This results in a sustained reduction of the mixing times. The presence of more holes also contributes to a faster mixing, despite the fact that number of bubbles in the simulations is exactly the same for a given flow rate.

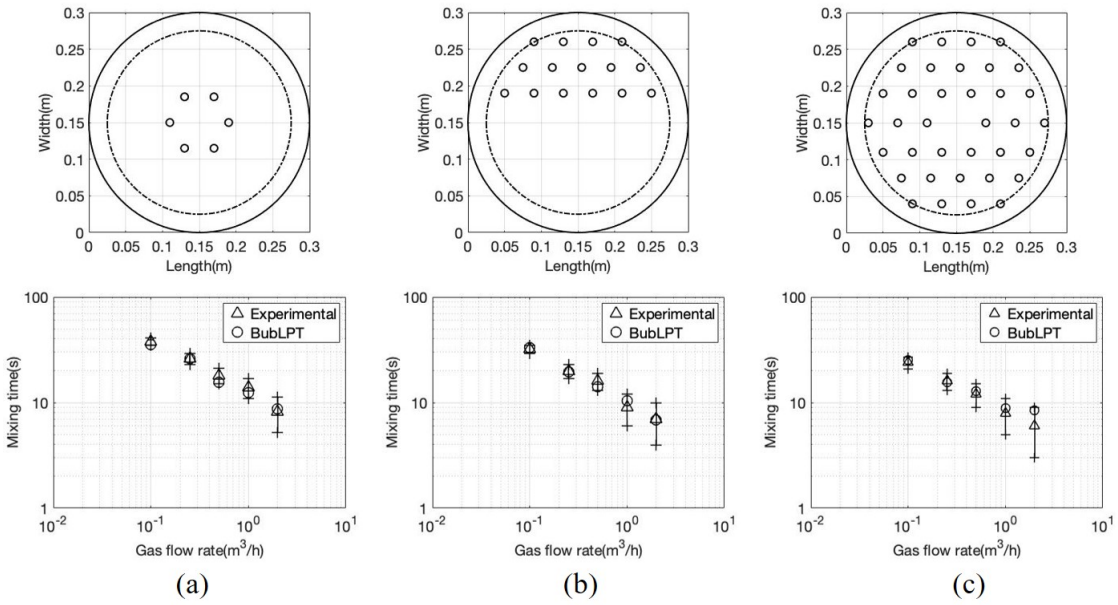

Figure 3.2: Mixing time estimated by our numerical simulations (circles) versus experimental data (triangles) [3] for three different setups: (a) 6-hole distributor (b) 15-hole distributor (c) 36-hole distributor.

Fig. 3.3 depicts the sensitivity of the predicted mixing time to the bubble size distribution, Eulerian grid size and numerical probes sampling density. These results are obtained for the 15-hole distributor. Compared to the 6-hole distributor shown in Fig. 3.1, the variance exhibits strong oscillations at early stages. This is due to the asymmetric distribution of the holes across the difusser plate; the resulting plume is not aligned with the centerline of the reactor and the flow is not axisymmetrical. Thus, the early development of the plume pushes all the tracer to one side of the reactor. A homogeneous mix starts building up only once the returning flow and the plume are established. Fig. 3.3a shows the response of tracer concentration to a monodispersed bubble-size distribution with an uniform diameter (5.6 mm) and a polidispersed distribution where bubbles have different diameters around the same mean value (5.6 mm) following a Gaussian distribution which ranges from 5.2 to 6.0 mm. Interestingly, the predicted mixing time does not seem to be influenced by the bubble size distribution, indicating that local effects are not critical in this case, perhaps due to the confinement of the computational domain. Fig. 3.3b exhibits

the evolution in time of the tracer concentration for three different grid resolutions: 3.125 mm, 5 mm and 6.25 mm. Despite some differences on the time evolution, the mixing time predicted by the medium grid size used for the validation is close to that found out by the finer mesh. However, the coarse grid simulation predicts a slight longer mixing time than the other two, probably due to lack of smaller-scale fluctuations. In order to prove that the sampling resolution is not critical to the model's predictions, the results provided by two significantly different numbers of numerical probes are compared by the medium mesh size and the monodispersed bubble distribution. On one hand the results for fifty numerical probes - that were employed for the validation - are depicted and compared to the mixing time estimate of five numerical probes which are located at the central section of the cylindrical tank; one of them is distributed in the middle point of the central section and rest four are allocated at the central point of each side. Fig. 3.3c shows that the time series obtained from five numerical probes fluctuates more acutely within the first seconds, whereas the estimation from fifty numerical provides a smoother evolution. However, the effect on the mixing time estimation is almost negligible.

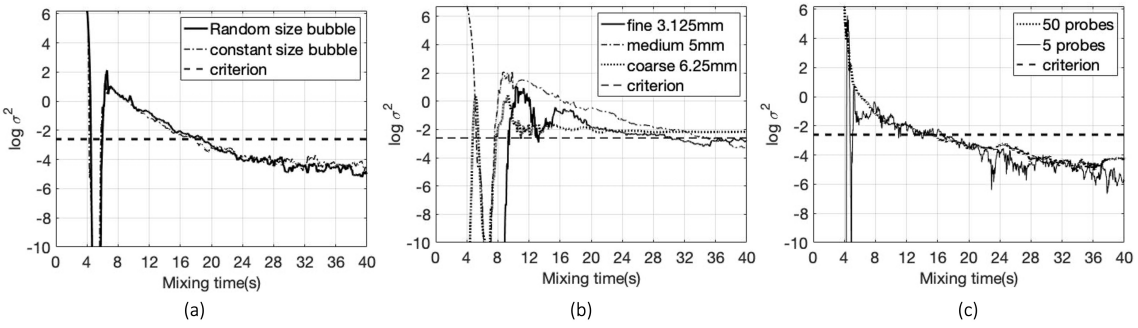

Figure 3.3: Tracer concentration time series across different parameters for 15-hole distributor: (a) bubble size, (b) mesh resolution, (c) number of numerical probes.

3.3 Analysis of buoyancy-driven mixing in a reactor

Once the ability of the model to accurately predict mixing time under a range of numerical and physical parameters has been validated, numerical simulations are carried out to quantify the mixing efficiency of different aeration designs in a large tank. In the context of this work, 'screen' refers to setups where multiple subsequent plumes occur simultaneously, in such proximity that the volumes of liquid entrained by their vertical currents overlap. In particular, the setups with 10 and 30 diffusers aligned at the centre of the tank do comply with this definition and will be referred to as bubble screens. The horizontal section of the numerical tank is rectangular, 1 m wide and 3 m long, and two water depths were simulated, 1 and 3 m. Bubble size was modelled as 2 mm and gas flow rates were tested at 0.125, 0.25, 0.5 and 1 L/min. The boundary conditions for the Eulerian field are non-slip condition at the bottom and a rigid lid at the water surface with a free slip condition for tangential velocities; all the lateral boundaries are periodic. Two mesh resolutions 5 and 6.25 mm were tested with $D_p/\Delta x$ ratios 0.4 and 0.32, informed by prior tests reported in [60] and [112]. Instead of being injected, as in the validation case, the passive tracer is accumulated at the top 25% of the tank's depth, as depicted in Fig. 3.4. With regards to air injection, four different designs of the aeration system are modelled: a single plume (SP), two plumes (TP) with a separation of 1 m, a bubble screen consisting of 10 blowers (BS10) and a bubble screen consisting of 30 diffusers equally spaced (BS30). All the blowers are located along the the central y plane. These configurations are tested at a total constant gas flow rate to prove their relative efficiency. To quantify the mixing homogeneity the whole tank is divided into 500 z equidistant planes. For each plane, the threshold representing the normalised standard deviation of the passive tracer's concentration (CV) can be expressed as:

$$CV = \frac{\sqrt{\frac{\sum_{i=1}^{N}(S_i-\bar{S})^2}{N}}}{\bar{S}} \tag{3.2}$$

where S_i refers to the averaged concentration of the -ith z plane, $\bar{S}$ is the average concentration in the entire tank and N refers to the total number of z planes. A more homogeneous mixing produces a smaller CV.

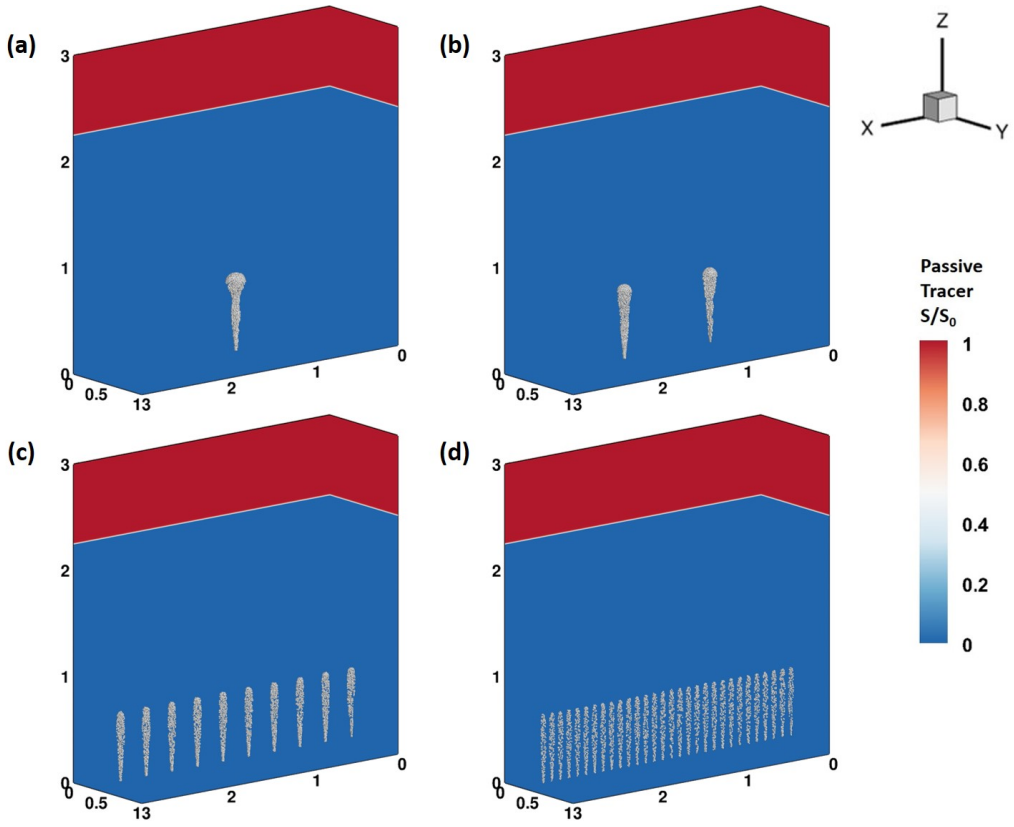

Figure 3.4: Initial conditions for the four aerator designs tested: (a) single plume (b) two plumes (c) bubble screen with 10 sources (d) bubble screen with 30 sources.

Figs. 3.5 and 3.6 offer a qualitative insight on the dynamics of the forced turbulent mixing in the tanks and the influence of the depth, the flow rate, the computational mesh and the blower distribution. Fig. 3.5 matrix shows the instantaneous normalised tracer concentration contours at the central plane of the tank depicted in Fig. 3.4. This figures compares SP and BS30 at a constant gas flow rate of 0.5 L/min in the smaller 1 m deep tank for two different mesh resolutions. The initial stratified tracer distribution is broken and mixed. Regarding the mixing rate, the bubble screen achieves a homogeneity faster than the single plume. SP initially breaks the upper layer, pushing the tracer to the sides of the tank, and effective mixing initiates

when the returning flow is entrained by the plume after hitting the tanks bottom. The screen, on the other hand, achieves a rather homogeneous mixture by 200 s, since the 30 blowers prevent tracer accumulation and minimise dead spaces. With regards to mesh sensitivity, there are small differences on the instantaneous tracer dispersion between the coarser and finer mesh in the SP case, although they do not affect in a meaningful way the mixing time estimation. The medium mesh seems to slightly overestimate the tracer's recirculation; this is most notable at 100 s. BS30 exhibits less significant differences between the two mesh resolutions, which does not seem to influence at all the overall mixing time. For both blower setups, the mixing patterns are unaffected by the mesh resolution.

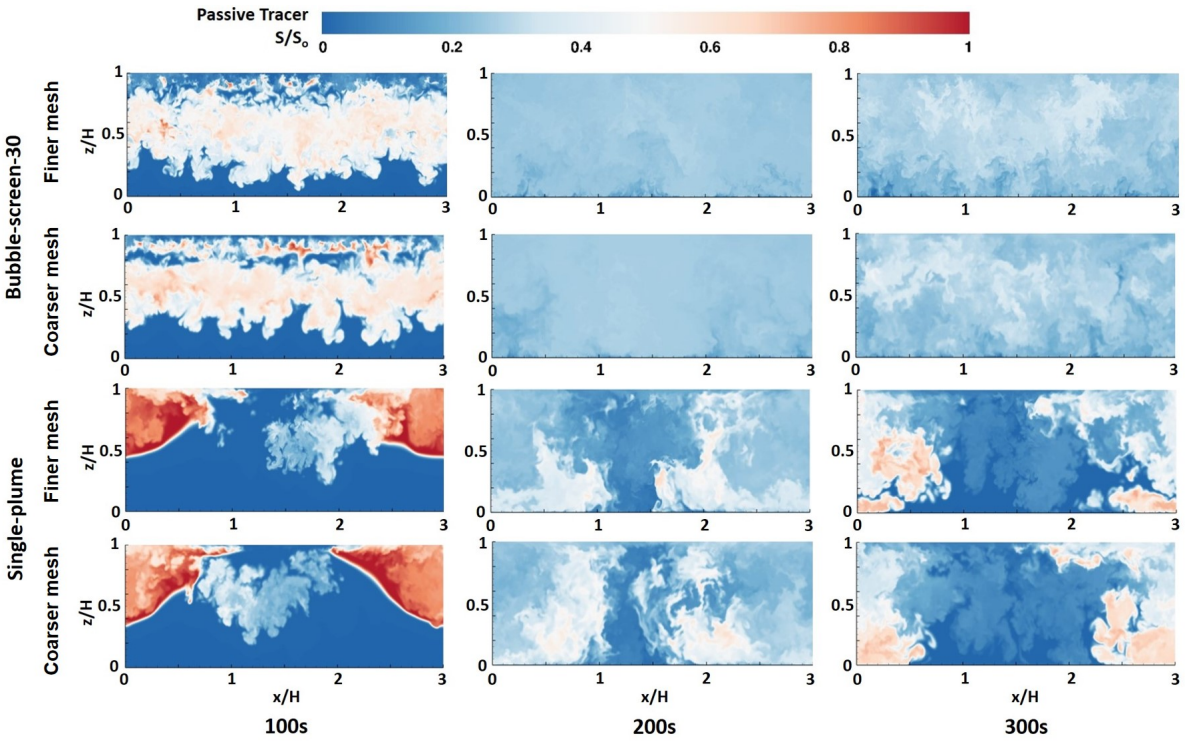

Figure 3.5: Instantaneous contours of normalised tracer concentration at three different instances for two different mesh resolutions.

Fig. 3.6 shows a matrix of results comparing instantaneous normalised tracer concentration contours in the central plane of the tank depicted in Fig. 3.4 for SP and BS30 sources under two different gas flow rates, 0.5 L/min and 1.0 L/min for the large 3 m deep tank. Again, there is a significant difference on the tracer dispersion

pattern between the single plume and the bubble screen design. For BS30, the initially stratified tracer is entrained in the recirculation currents of the 30 small plumes simultaneously and moves towards to the bottom rapidly and uniformly; for SP, as observed in the shallower tank, the tracer is advected towards the sides. Hence, the bubble screen achieves homogeneous mixing faster than the single plume also in the large tank. As expected, a higher gas flow rate produces faster mixing, albeit interestingly this effect appears to be less critical than the spatial distribution of blowers. Also, the gas flow rate increase seems to be significantly more effective for the bubble screen than the single plume. Compared to the mixing observed in the 1 m deep tank depicted in Fig. 3.5, the significant increase in volume in the deeper tank results in slowing down the mixing process, however this delay is not proportional to the volume increase. While the larger tank has 3 times the volume of the smaller one, the results show a similar qualitative level of mixing at 300 s for the shallower tank and 400 s for the deeper one operating in the same conditions (0.5 l/min gas flow rate). It is not expected that this would be necessarily true if the tank's volume is increased in width or length, but the buoyant plumes are particularly effective against increasingly deeper liquid columns.

Fig. 3.7 represents the tracer concentration against the tank's depth at four different simulation times. Each plot corresponds to a different blower design (SP, TP, BS10, BS30); the gas flow rate (0.5 L/min) and the tank's depth (3 m) remain constant. The black lines in each sub-figures refer to the vertical concentration profiles at four different instances in time ranging from 100 to 800 s and the grey dotted line indicates the initial tracer distribution. For all designs, the predictions tend to converge to a relatively homogeneous concentration of $S/S_0 = 0.25$, providing a rather similar final picture in all cases. However, the pace at which the mixing occurs is rather different. In general, the more blowers, the faster homogeneity is achieved, being the 200 and 400 s lines quite representative of this. The tracer transport

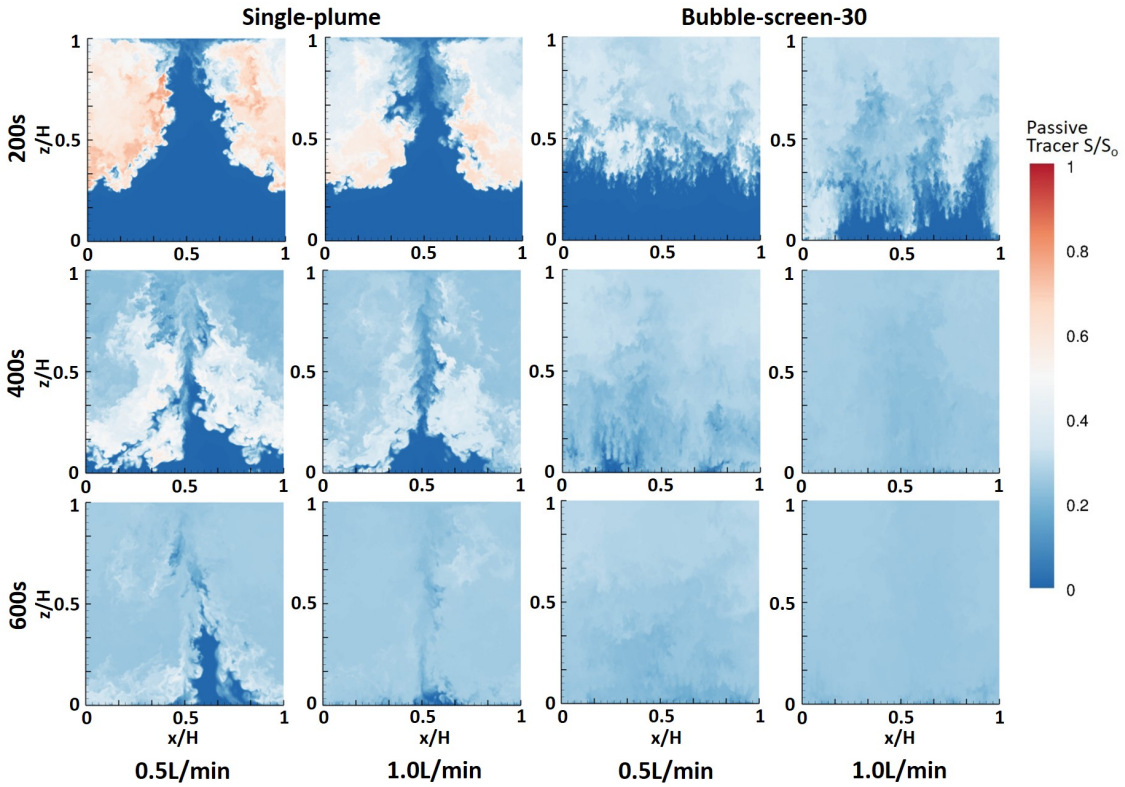

Figure 3.6: Instantaneous contours of normalised tracer concentration at three different simulation times (200, 400 and 600 s) for two different gas flow rates (0.5 and 1 l/min) in the 3 m deep tank.

mechanism consists fundamentally in trapping the accumulated virtual dye at the top 25% of the tank in the recirculation current travelling downwards, something that is effectively achieved around 400 s. In fact, BS30 shows a near final and complete mixing from 400 s on. This is almost the case for BS10 as well, but the tracer is not yet completely spread out across the bottom of the tank. Since SP consists of a solitary plume, the recirculation current requires longer to advect the tracer across the tank's bottom, and this is reflected in its 400 s profile. Interestingly, for TP there is a strong indentation in the tracer's concentration profile at 400 s but is not by the bottom but at $z = 1\ m$ instead; with all probability the result of a trap layer originated by the interaction of both plumes' recirculation. The early evolution (100-200 s) is quite different between the different designs, with the bubble screens showing a more effective mixing. On the other hand, SP and TP achieve a very homogeneous final state (800 s), while the screens mantain a small concentration gradient between the bottom and the surface. Overall, there is not clear advantage for the TP design compared to SP.

Fig. 3.8 shows the time series of the normalised standard deviation (see Eq. 3.2) of the tracer's concentration for each blower design at a constant gas flow rate of 0.5 L/min in the shallower tank. Solid lines correspond to the coarser computational mesh while dashed lines represent the finer mesh. CV=0.25 is marked with a horizontal line as a threshold that indicates good mixing (relative variation across the reactor below 25%). The results for each setup exhibits that the normalized tracer concentration deviation increases within the first 50 seconds and then enters a decrease pattern. This pattern is almost linear for SP and increasingly non-linear (more so with more blowers) for multi-plume designs, with a steep decrease in the 100-200 s range followed by a gradual relaxation as equilibrium is approached. BS30 mixes the liquid phase faster than the other three designs, reaching the threshold before 200 s, followed by BS10 which reaches CV=25% at 250 s. TP and SP reach

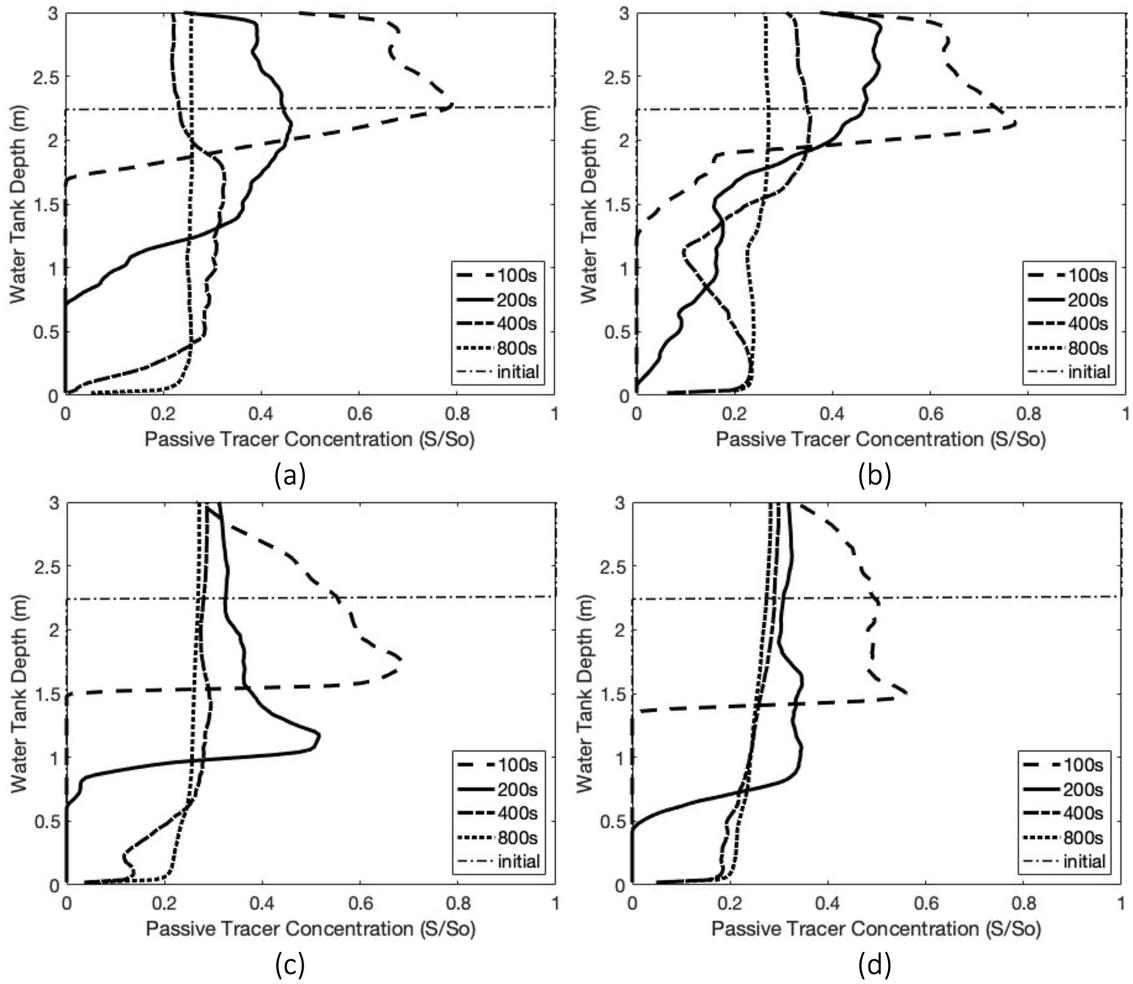

Figure 3.7: Simulated tracer concentration profiles at four different times of the simulations for a constant total gas flow rate in the 3 m depth tank: (a) single plume (b) two plume (c) bubble screen 10 (d) bubble screen 30.

the threshold show rather similar mixing times, approx. 350 s. Regarding the mixing quality, SP, BS10 and BS30 reach a similar final state around CV=0.15, whereas TP remains in the 20-25% range. In addition, the differences observed in the prediction for the two computational grids are negligible. It is for bubble screens, in particular BS10, that more deviation is found between the coarser and finer grids. Whilst such disagreements do not affect the trend nor final predictions, they suggest a slower progression of the mixing process, in agreement with the observations made in Fig. 3.5.

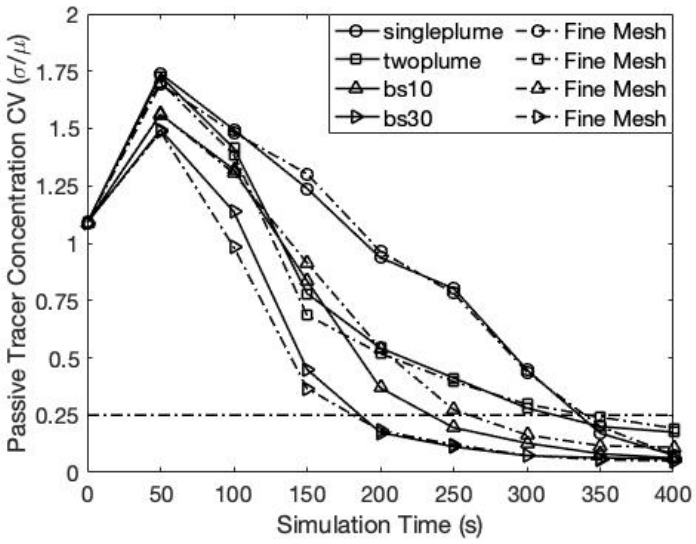

Figure 3.8: Time evolution of the normalised standard deviation of the tracer's concentration for two mesh resolutions and four blower designs at a constant gas flow rate in the shallow tank. Solid lines: medium mesh size; Dashed lines: fine mesh size.

The influence of gas flow rate on the mixing efficiency in the deeper tank is shown in Fig. 3.9. Each sub-figure corresponds to a blower design; the lines represent the four different gas flow rates. CV=0.25 is marked with a horizontal line as a threshold that indicates good mixing (relative variation across the reactor below 25%). These results clearly state how the contribution of gas flow rate is critical to the mixing efficiency, particularly for SP and TP (Fig. 3.9a and Fig. 3.9b). Lower flow rates (0.125 and 0.25 l/min) see a very low decrease in the CV or even a slight increase at early stages. Perhaps the most remarkable effect of flow rate on the mixing trend is

how, after 1000 s, it affects the homogeneity of the mixture, i.e., the final CV value. This is particularly notable for the plumes (SP and TP) and the lowest flow rate. In general, the changes in flow rate do not affect the curves' shape, aside from their gradients. Lower flow rates exhibit less abrupt reductions in CV, whereas higher flow rates trigger rapid CV decrease at the early stages (up to 400 s), followed by a gradually asymptotic behaviour approaching the equilibrium concentration. Only for SP and 0.125 L/min a change of concavity is observed.

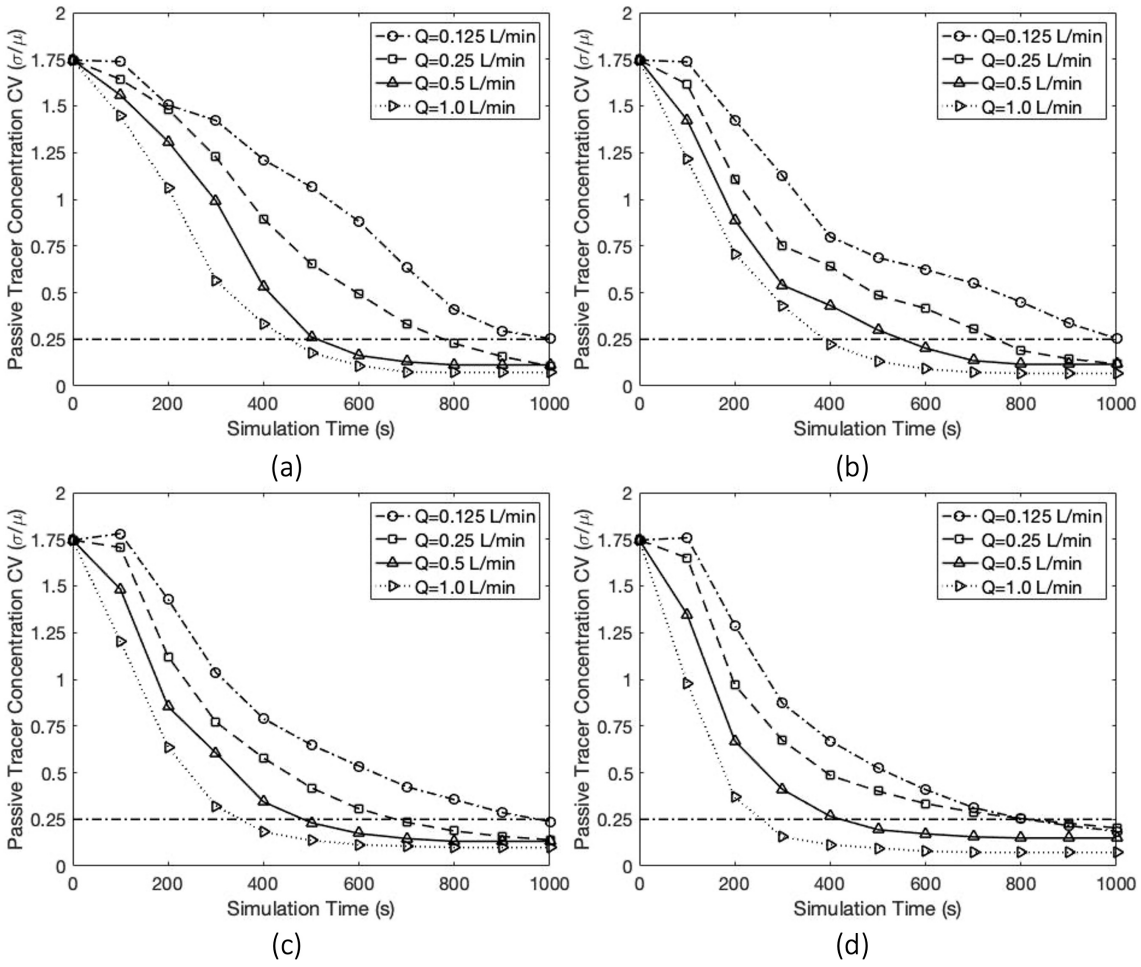

Figure 3.9: Time evolution of the normalised standard deviation for different flow rates and the following blower designs: (a) single plume (b) two plumes (c) bubble screen with 10 blowers (d) bubble screen with 30 blowers.

Fig. 3.10 provides a different perspective to the same dataset displayed in Fig. 3.9. Each subfigure shows the evolution in time of CV to compare the mixing efficiency of four different aerator designs at a constant gas flow rate. This plot corroborates

some of the observations discussed for Fig. 3.9, e.g., the flow rate determines the final homogeneity (measured via CV) of the mixture, but the blowout distribution has a more critical effect on the mixing time, i.e., the point at which a homogeneity threshold (CV=0.25) and the equilibrium concentration is reached. Figs. 3.10a and 3.10b, corresponding to 0.125 L/min and 0.25 L/min respectively, show how SP exhibits a remarkably different behaviour to the other three designs. Such difference is reduced as the flow rate increases (Figs. 3.10c and 3.10d). Based on the same criterion mentioned in Fig. 3.9, bubble screens are superior regarding mixing time than single or dual plumes for the same flow rate. However, over this parameter range, TP shows a comparable performance to BS10, qualitatively superior to SP. The different designs do not appear to alter significantly the final state, but the speed at which the systems gets to it.

The simulation results presented thus far clearly state the relevance of the blower distribution and flow rate on the mixing process and the differences between them. However, it is difficult to determine which setup would be optimum merely based on this. Fig. 3.11 compares the mixing efficiency of the four blower designs and four gas flow rates for the deeper tank in terms of the consumed gas volume required to achieve completed mixing (this is, to reach $CV \leq 25$. Overall, increased gas flow rates contribute linearly to the required gas volume. This means that the speed up achieved with a higher flow rate does not compensate the extra energy required to pump it. BS30 demands a significantly inferior amount of air than the other three setups for any given gas flow rate. In order to quantify the energy consumption, the input power required to pump air at a certain rate is calculated like follows:

$$P(w) = \rho Q g H \tag{3.3}$$

where ρ refers to the density of liquid in the tank, Q is the gas flow rate, g represents the gravity acceleration and H represents the tank's height. Based on the calculations

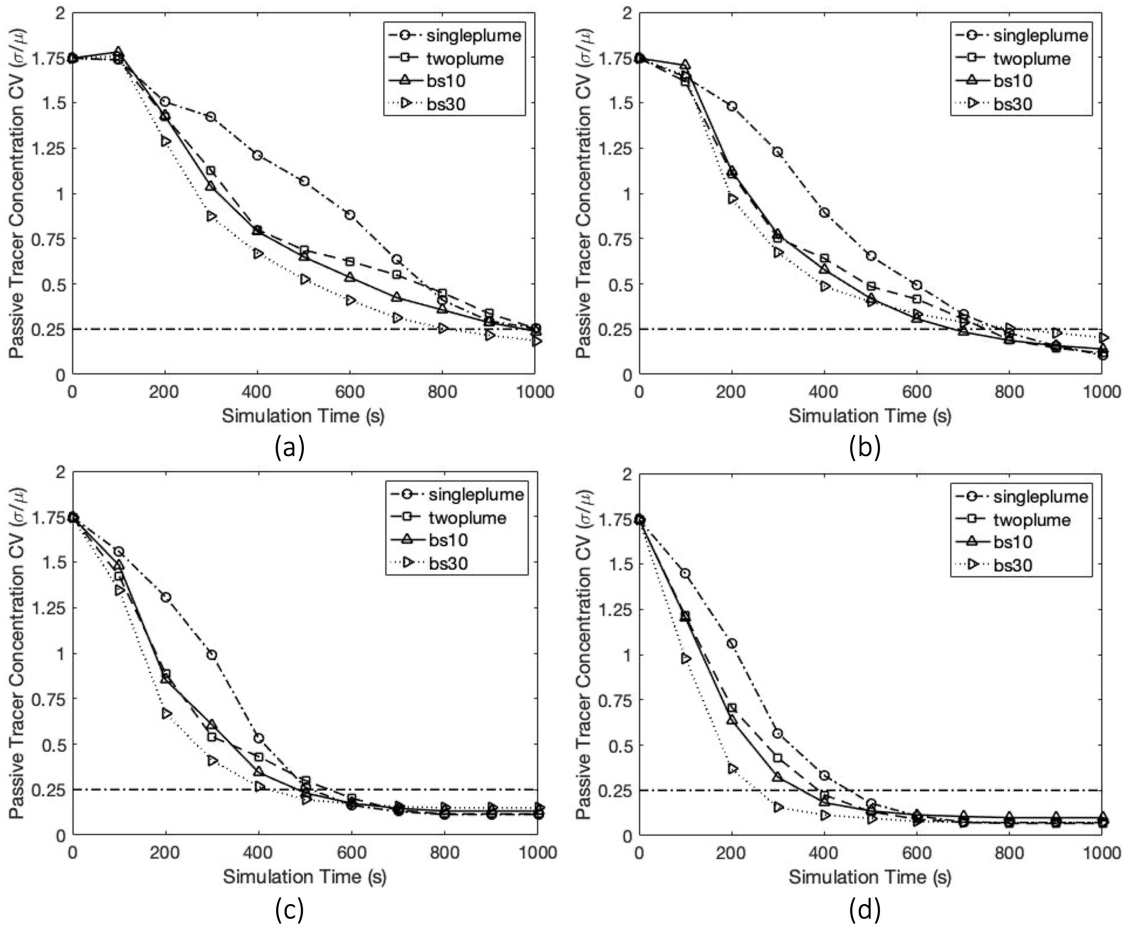

Figure 3.10: Time evolution of the normalised standard deviation for four different flow rates: (a) 0.125 L/min (b) 0.25 L/min (c) 0.5 L/min (d) 1.0 L/min.

shown in Fig. 3.11. the energy consumed by each configuration that was investigated is presented in Table 3.2.

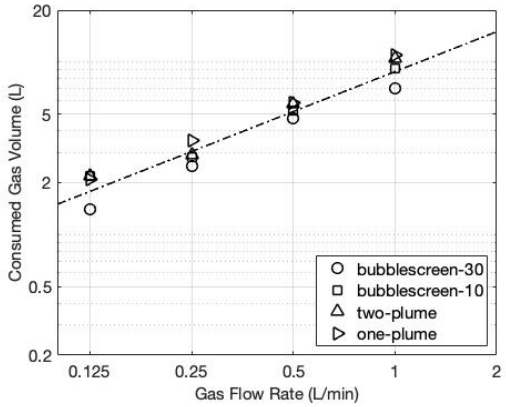

Figure 3.11: Comparison of total gas consumption versus gas flow rate for the four blower designs in the deep tank.

Table. 3.2 reveals that complete mixing requires 150-250% more energy in the larger tank. It is interesting to note that the increase in required power is clearly below the increase in volume from one tank to another (300%), supporting the qualitative analysis provided by Fig. 3.6. Bubble screens are more energetically efficient for a given flow rate; BS30 is capable of an energy save of 19.4-37.7% compared to SP. The energy consumed by BS10 and TP is relatively similar, exhibiting less than a 12% difference. An anomaly in this general trend was found for the lowest flow rate (0.125 L/min), at which the energy consumption of a single plume is slightly below TP and BS10, and only BS30 provides a clear enhancement. This suggest that low flow rates are less sensitive to the spatial distribution of the buoyancy sources. The results also suggest that increasing the gas flow rate is less effective than optimising the blower distribution in terms of cost-effectiveness. However this analysis is only made considering the desired final state; if time is a constrain, it might be preferable to accelerate the process with higher flow rates.

Input Power		Energy Consumption until mixing time (J)			
Q(L/min)	converted power(w)	single plume	two plumes	bubble screen 10	bubble screen 30
1m Depth Tank					
0.5	0.0818	24.9	22.7	20	14.7
3m Depth Tank					
0.125	0.0613	62.2	65.1	65.7	40.5
0.25	0.1226	103	84.8	81.2	73.6
0.5	0.2453	170	166.6	154.3	137
1.0	0.4905	320	308.4	271.5	207

Table 3.2: Energy consumption required to achieve full mixing for all the scenarios considered in the simulations.

3.4 Conclusions

A point-particle LES model incorporating scalar transport is applied to predict buoyancy-driven mixing time and optimal combinations within a parameter range focused on the spatial distribution of blowers, the gas flow rate and the tank's depth. The in-house CFD solver had already been validated in terms of the hydrodynamics of the bubble plume [60]. This paper provides further validation of its ability to predict mixing in a bubble reactor by simulating three different types of gas distributor and five flow rates and comparing the mixing times to experimental data [3]. The results exhibit a remarkable agreement with the experiment. The influence of the bubble size distribution is analysed and does not reveal significant differences with regards to the mixing time. Moreover, the grid independence of the model is proven by comparing different mesh resolutions.

To the authors' knowledge, this work presents the first comparison on mixing efficiency between bubble screens and plumes in a turbulence-solving simulation. The results show significantly different mixing times between plumes and bubble screens. Bubble screens provide superior mixing efficiency for a given gas flow rate. By considering the energy expenditure, the results suggest that the bubble screen with 30 blowers can save at least 20% of the energy required by the other setups. Quantitative results also show that implementing a bubble screen-based layout is more effective in terms of energy consumption than increasing the gas flow rate.

The sensitivity analysis on the gas flow rate reveals that a higher gas injection velocity improves the mixing speed and has an impact on the final homogeneity, while the blower design does not affect the final result but has a critical impact on the efficiency of the process. The results also prove that, if time is not a constrain, it is more energetically efficient to use lower flow rates. Increased tank depth implies a significantly higher gas expenditure, but in a much lower proportion that the volume increase (up to 50%), hence deeper reactors are more efficient. There is a qualitative difference between the single plume case and the others, revealing that, at a constant flow rate, combining recirculation currents and distributing the gas release across several smaller plumes provides more efficient and faster mixing.

Acknowledgements

The authors would like to thank the University of Birmingham, the HPC Midlands consortium and EPSRC for their support providing computational resources for this research in their BlueBEAR and HPC Midlands+ systems.

Chapter 4

An Eulerian-Lagrangian Approach to Simulate Gravity Currents Driven by Inertial Particles

The work is presented in UK Fluid Conference 2021

Ready to submit to the Physics of Fluids

CRediT authorship contribution statement:

1. Literature review on experimental research with the aim of validating the accuracy of code solver to predict density-driven and particle-driven gravity currents.

2. Implement the Boussinesq approximation to solve density-variable flows.

3. Implement the soft collision model to solve particle-to-particle interaction.

4. Design numerical simulations of density-driven and particle-driven gravity currents.

5. Post-process numerical results and compare them with experimental measurements.

6. Draft the original manuscript, review and edit it.

4.1 Introduction

Gravity currents are density variable flows that develop primarily in the horizontal axis as a result of a heavier fluid propagating into a lighter one [154]. Forecasting the dynamics of gravity currents is crucial for many applications in nature and engineering, such as sea breezes, airborne snow and sedimentation transport in the oceans [145]. Under the influence of gravity, these flows are driven by the density variation within a fluid or between two fluids and considered as density-driven gravity currents (DGCs) or conservative currents [29]. Particle-driven gravity currents (PGCs) are instead generated by spatial variations in suspended particle loading; these are commonly non-conservative since the density difference constantly evolve as particles settle.

Extensive experimental and numerical researches have been performed around the world to gain insight into gravity currents [116, 118, 81].These real-scale experiments investigate a limited number of conditions, and are often used by modellers to validate their numerical model [117, 97]. The researchers [134] performed lock-exchange experiments in a rectangular-section channel where the two fluids were salt and fresh water, and successfully captured features of gravity currents such as the Kelvin-Helmholtz instabilities at the interface between the lighter and heavier fractions. C. Adduce et al. [1] presents a series of lock-exchange experiments performed under a range of different lock positions, initial current heights and induced gravity. To understand the effect of suspended particles on gravity currents, turbidity currents were investigated in experiments by the release of a fixed volume of the suspended particle into a lighter ambient fluid in rectangular water tanks [15, 67, 45]. Overall, experimental results focus on the suspension of solid particles and the propagation of current fronts as well as the sedimentation layer in turbidity current.

From a modelling perspective, two simplified modelling approaches, box model and shallow water model, were the early attempts to predict gravity current based on the assumptions that viscous forces are negligible and the fluid inside the current is at rest [134, 15, 68, 71]. The results validated by the experimental measurements indicate that the simplified numerical models are able to generally simulate the propagation of gravity currents albeit their inherent assumptions imply necessarily some shortcomings: their reliance on empirical parameters prevents the application to all conditions and results in poor robustness of numerical model (e.g. the coefficients in front speed formulation are determined by experiments) [80, 134]; steady state assumption under-predicts the instabilities of gravity currents (i.e. the entrainment of ambient fluid and the friction induced by the suspension of solid particles) [40]. Upon the availability of three-dimensional transient computational fluid dynamics (CFD) technology and computational resources to run it, the earlier numerical works evolved into high-resolution simulations by considering gravity currents as a multiphase density variable flow phenomenon implicating the scales of motion driven by the suspension of solid particles and density variance within ambient fluid [52, 143, 119]. Providing reliable predictions through high-resolution CFD is challenging given the need for an accurate treatment of the shear layer at the interface between the denser and lighter fluid and the importance of characterising the turbulence of the continuous (ambient fluid) and dispersed (suspended particles) phases in turbidity currents as well as the coupling and interaction between the two. Regarding buoyancy effects, the Boussinesq approximation is often used to account for the influence of density variance on gravity currents by assuming that the contribution of density variations is negligible in the flow field and can described as the raise to buoyancy forces [29]. As the turbulence closure for the ambient fluid, there are three fundamental modelling alternatives: Direct Numerical Simulation (DNS), Large Eddy Simulation (LES) and Reynolds-Averaged Navier-Stokes simulation (RANS). DNS is acknowledged as the most accurate approach to

solve all the turbulence scales involved in gravity currents but its high computational cost prevents its application to real and laboratory-scale cases with high Reynolds numbers [62]. RANS or Unsteady-RANS have been the most common approach to predict density variable flows until the last decade. RANS-based simulations provide a good compromise for practical applications by introducing closure models to account for the turbulent fluctuations [8] and are able to simulate large-scale gravity currents [66]. However, the assumption of isotropic turbulence embedded in most popular RANS closures is rather unnatural for stratified flows, leading to an underestimation on unsteady structures (i.e. Kelvin-Helmholtz vortexes at the interface and wall-bounded turbulence [6]. LES can explicitly capture large-scale turbulent structures and model the less energetic small-scale turbulent structures through a subgrid-scale (SGS) model, reducing the relative influence of turbulence closures upon the predictions, with a significantly lower computational cost than DNS [35], yet still bounded by high Reynolds numbers.

Regarding to the prediction of dispersed phase (suspended particles) for turbidity currents and their contribution to the ambient fluid, the most common approaches are Dusty-Gas (DG), Equilibrium-Eulerian (EE) and Point-Particle-Lagrangian (PPL) [33, 23, 86]. DG models are the most common approach to simulate density-driven gravity currents (DGC) by assuming that the particles are fairly small and can follow the local carrier fluid. When DG methods are applied, the denser and lighter fractions are simplified as a single fluid whose density only relies on the local volume fraction of suspended particles, which is modelled as a concentration field transported by a convection-diffusion equation. Hence DG models struggle predicting the effects of the dynamics of individual suspended particles, e.g. small-scale turbulence, settling and particle-to-particle interactions. EE models also establish a relationship between density field and the local mass fraction of suspended particles in a single fluid but introduce particle settling velocity. Comparing to DG, EE mod-

els can simulate the natural physics of solid particles in an Eulerian framework and predict their contribution to the surrounding fluid (i.e. slow down the propagation of the currents and generate instabilities within the interface between the denser and ambient flow) in turbidity currents [117]. EE models are constrained when it comes to simulate polydisperse distributions with a wide range of particle sizes since the empirical introduction of particle settling velocity assumes that density and size of all particles are unique [11]; and the trajectory of individual particles is not accounted for in this model, leading to a lack of producing the local interaction between suspended particles. PPL models respect the discrete nature of the dispersed phase and do not further impose limitations on the size distribution of the particles or local particle Reynolds number Re_p [46, 59], by describing the particles in a Lagrangian framework. The way in which the interaction between both phases is modelled depends on the particle size and concentration. Due to the high density ratio between particles and water, the interaction and coupling can be calculated by a two-way coupling approach to characterise the disruptive influence of the dispersed phase on the surrounding fluid. This is acceptable for dilute particles concentrations, while very high solid fractions require considering particle-to-particle interaction (four-way coupling) [77, 109].

There are several recent examples of application of the DG methodology to investigate DGCs under complex conditions that provide a remarkable insight into the fluid mechanisms of gravity currents, e.g. current head and tail motion, entrainment generated by the interaction between heavier fluid and surrounding fluid [125, 171, 122, 61]. The numerical strategy for simulating PGCs still faces important challenges to solve the turbulence scales induced by the suspension of solid particles. F. Necker et al. [117] implemented a high-order mixed spectral-element simulation based on the EE approach to predict the fate of the suspended particles during the propagation of turbidity currents. They employed a continuum equation

for the particle concentration field to track the suspension of solid particles, with the size of the particles represented by an empirical settling velocity. The results obtained initially indicate significant differences caused by the suspended particles: DGCs travel faster than PGCs without the influence of settling particles on the front speed of the current. It is revealed as well that the velocity of the particles are only accounted for in the direction of gravity and not sufficiently tracked by EE model, requiring a further investigation on the trajectory of individual particles and the interaction between particles. S. An et al. [6] explored three-dimensional PGCs by using Equilibrium-Eulerian approach based on a RANS (EE-RANS) solver and validated their results with experimental measurements. The comparison on the front speed of the current indicated that their EE-RANS model was capable of predicting the flow field driven by solid particles within turbidity currents. However, their results exhibit that the RANS models struggle to gain the instabilities induced by particles when incorporating with EE approach (i.e. isotropic assumption averages small scales generated by settling velocity), which can be further investigated and improved by applying transient CFD model for the ambient fluid (i.e. LES and DNS model) and calculating the coupling between the particles and carrier fluid in Lagrangian framework (i.e. PPL approach). In order to solve all the turbulence scales within turbidity currents, [62] and [52] used an EE method based on DNS (EE-DNS) model to simulate PGCs in a lock-exchange configuration. The results show that this model is capable of reproducing the mechanics of the carrier fluid: Kelvin-Helmholtz vortices generated by the entrainment of heavier fluid into the lighter one and lob-and-cleft structures formed at the currents' interface. However, the treatment of the suspension in their model highly depends on the empirical setting velocity. And the concentration field only indicates the volume fraction of particles but cannot describe the natural dynamics of particles (i.e. collision between them and their interaction with the wall). M. I. Cantero et al. [22] developed their own formulation based on an EE-DNS model to include the contribution of the

particles' inertia within turbidity currents, where the inertial response of particles is related to the time scales of the flow field. The authors tested their new model in a two-dimensional case and showed how PGCs differ from DGCs in integral aspects due to the four-way multiphase interaction, e.g., increased current's front speed in slumping phase and leading to instabilities within the boundary layer near the bottom. Their results highlight that the Eulerian approach is limited to simulate the system with multiple particles and can be further explored by adopting Lagrangian algorithm to avoid the unique description of the particles. To relax the reliance on empirical estimations of the particle settling velocity [71, 132], a recent research conducted by [33] adopted point-particle Lagrangian (PPL) approach to forecast the dispersed particles in turbidity currents. The authors applied force model to predict the interaction between the particles and ambient fluid, and implemented collision model to account for particle-to-particle interaction. Their results firstly gain the insight on the dynamics features of particles, such that the particles settled down at the bottom and are entrained by the local flow field. However, their model requires a further validation with the experimental measurement with regards to the froude and Richardson number [142].

Despite the prolific body of research on experimental and numerical investigation of gravity currents, there are very few LES-based studies of gravity currents based on a critical analysis of the scientific literature [110]. In the particular case of turbidity currents, there is the extra challenge of modelling the dispersed phase; EE models are the usual choice due to its cost-effectiveness and overall good depiction of integral properties, albeit they struggle to find simulate non-negligible effects of particle inertia and particle-to-particle interaction. In addition, the boundary condition of concentration field in EE models usually assumes that the particles are supposed to leave the computational domain with the settling velocity, which is limited to predict the resuspension of particles from the sedimentation layer [115].

Point-particle Lagrangian model can be a wise choice to simulate the particles in turbidity currents since this approach has been widely applied to forecast multiphase flows with higher accuracy than EE model (i.e. discrete air bubbles in water and solid particles in liquid) [24, 78]. The great advantage of tracking the particles in a separated framework can help the modeller understand the interaction between the suspended particles and settled particles in turbidity currents. However, the simulation of PGCs is rarely adopted by this algorithm since the high computational effort on the calculation of particles.

This paper focuses on the differences between density-driven and particle-driven gravity currents. Our aim is two-fold, to elucidate the physical features that separate the dynamics of these processes and explore how this translates into different modelling approaches for an accurate forecasting. In the first part of the paper, density-driven gravity currents (DGCs) in lock-exchange experiments will be numerically simulated using a LES-based Dusty Gas (DG) approach and validated versus experimental data. The results also analyse the impact of selected parameters such as induced gravity and the lighter-to-heavier fluid ratio on the propagation of DGCs. In the second part of the paper, a LES-based PPL solver developed by [60] is used to explore turbidity currents (PGCs). This solver incorporates a soft-sphere collision algorithm to provide four-way coupling. Numerical results will be also validated versus experiments. Finally, on its third part, this paper will analyse comparatively the flow features exhibited by DGCs and PGCs under otherwise identical circumstances (computational domain, boundary conditions, density ratio) and discuss the contribution of inertial particles to the energy budget of turbidity currents. It is noteworthy that, despite sharing the same Navier-Stokes solver in the background, the driving mechanisms of PGCs and DGCs within our LES are completely different. While the flow generated by the latter is the result on a density field driven by convection and diffusion, the turbidity current is driven by the joint

action of each individual particle's inertia and the consequent entrainment of the surrounding fluid.

4.2 Model performance assessment

4.2.1 Density-driven gravity currents: DG-LES model

The ability of our DG-LES model to predict buoyancy-driven gravity currents is tested against the experimental measurements performed at the Hydraulics Laboratory of the University Roma Tre, Rome (Italy) by [1]. A series of lock-exchange experiments were run in a transparent plexiglas tank shown in the Fig. 4.1. The tank's depth is $h_0 = 0.3\ m$, length $L = 3\ m$ and width $b = 0.2\ m$. A sliding gate is placed at a variable distance x_0 from the left wall of the tank. The right hand side of the gate is filled with fresh water with a density $\rho_2 = 1,000\ kg/m^3$, and the left hand side is filled with salted and dyed water with a density $\rho_{01} > \rho_2$. Both sides of the tank are filled to the same depth h_0 at the beginning of each experiment that starts when the sliding gate is quickly removed. The simulations of density-driven gravity currents (DGC) in this paper are carried out under analogous conditions to the experiment. No-slip boundary conditions are applied at all solid walls, the free surface is a rigid lid with a symmetry condition and the water in both compartments is initially quiescent. The salt concentration in the experiments is modelled as active tracer linked to the density field within the computational domain. A passive tracer is employed to visualise the flow field. The grid size is chosen as 3.125 mm according to the mesh convergence where a coarser mesh size 6.25 mm and a finer mesh size 0.125 mm are analysed in terms of the current front speed. And time step is adopted as 0.001s. Based on the cases tested in the experiments, all numerical simulation layouts are summarized in Table. 4.1.

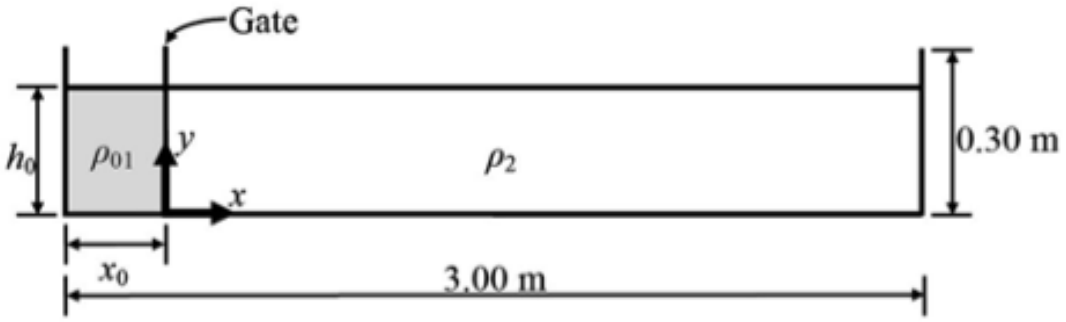

Figure 4.1: Experimental lock-exchange setup for density-driven gravity current [1]

Case	x_0 (m)	h_0 (m)	ρ_{01} (kg/m^3)	$g_0^{'}$ (m/s^2)	Fr	Ri
1	0.10	0.30	1,034	0.32	0.65	2.4
2	0.10	0.30	1,063	0.58	0.38	6.8
3	0.10	0.30	1,089	0.80	0.25	16.7
4	0.20	0.30	1,036	0.34	0.39	1.9
5	0.20	0.30	1,059	0.55	0.49	4.1
6	0.20	0.30	1,087	0.79	0.3	11
7	0.30	0.30	1,037	0.35	0.93	1.7
8	0.30	0.30	1,064	0.59	0.53	3.5
9	0.30	0.30	1,090	0.81	0.37	7.5

Table 4.1: Simulation parameters for the density-driven gravity current

Fig. 4.2 compares the evolution of the gravity current predicted by experiments and mathematical models by [1] (left) with our DG-LES (right). The figure shows four instantaneous snapshots at identical times; superimposed on the experimental results there are a dotted line indicating the position of the free surface and solid and dash-dotted white lines depicting the DGC's profile prediction based on the two-layer shallow-water model proposed by [1] for miscible (k=0.48) and immiscible (k=0) fluids, respectively. The simulation inputs correspond to case 9 as described in Table. 4.1. To replicate the dye tracer employed in experiments to track the evolution of the heavier fluid, a passive tracer was included in the PPL-LES to visualize the initial locked flow field before removing the gate and its concentration field is shown in Fig. 4.2 (right). The position and shape of the current's front predicted by PPL-LES closely resembles that of the experimental data. The vortical structures at the shear layer between the heavier and lighter fluid are better defined in the visualisation obtained from the numerical simulations, whereas the current's tail is more faded.

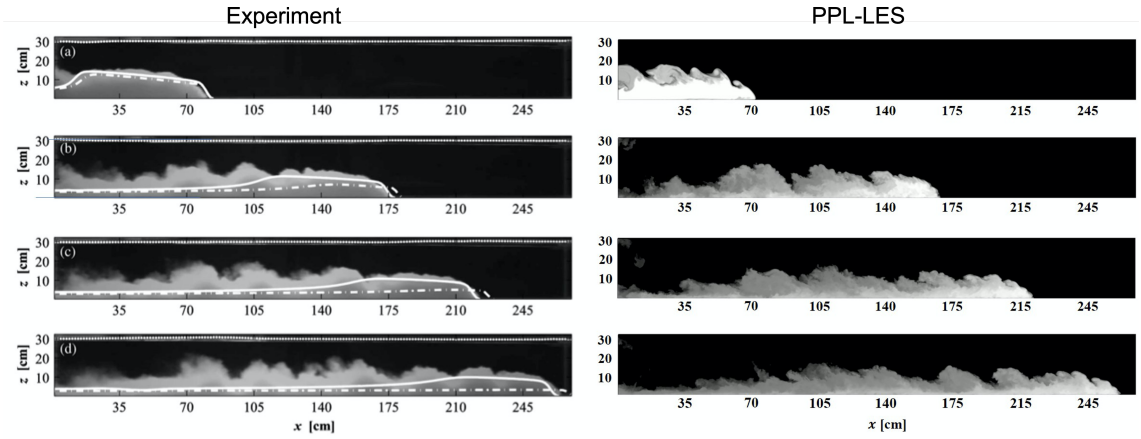

Figure 4.2: Evolution of DGC traced with dye in laboratory experiments [1] (left) and with a passive scalar concentration field in PPL-LES simulations (right) at times (a) 3s, (b) 7s, (c) 9s and (d) 11s.

Fig. 4.3 presents the temporal evolution of the DGC's front position for both the PPL-LES (curves) and experiments (symbols) across the nine cases described in Table 4.1. A remarkable agreement with the experimental measurements is exhibited

for all cases. The numerical predictions are always consistent across the line of the experiments. In addition, the comparison between the parameters summarized in Table. 4.1 reveals that a higher induced gravity is able to significantly accelerate the propagation of gravity current.

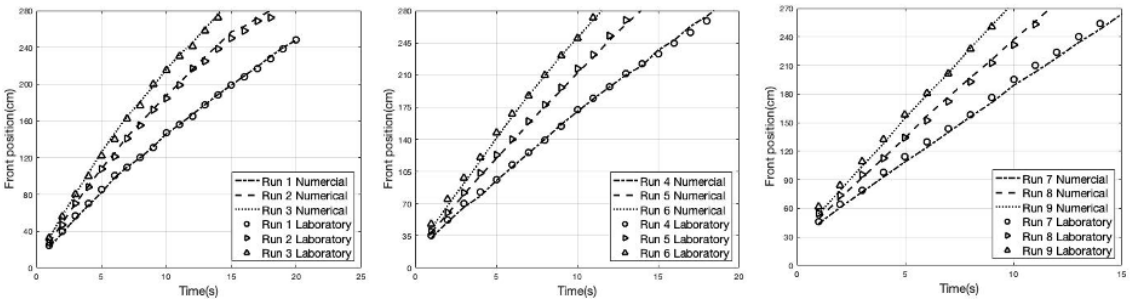

Figure 4.3: Comparison of the temporal evolution of the DGC's front position for: curves, numerical results; symbols, experimental results.

To visualise the current's head, the area is defined as 0.4 m length starting from the front position. Fig. 4.4 and Fig. 4.5 shows iso-surfaces of salt concentration by the current's head at 3s and 18s for case 9, describing the qualitative evolution of loft-and-cleft structures. The iso-surfaces at two times correspond to the same concentration value normalised by the maximum concentration. At t=3s the interface is dominated by the evolution of Kelvin-Helmholtz vortices at the boundary layer which interact with wall-bounded turbulence in the spanwise direction. The smooth interface between shows that the concentration field remains rather homogeneous and the current has not transitioned into turbulence. At a later stage (18s), the DGC's head depicts a wrinkled interface showing the growth of small-scale turbulent perturbations and inhomogeneous mixing. As shown in Fig. 4.5, the 2D views clearly show how the loft-and-cleft structures exhibit symmetric features along the spanwise direction at an early stage (3s) in which the current is smoothly driven by density variance. As these structures are gradually entrained by shear-induced turbulent flux, the symmetry and the large/medium scale structures are broken by non-linear interactions.

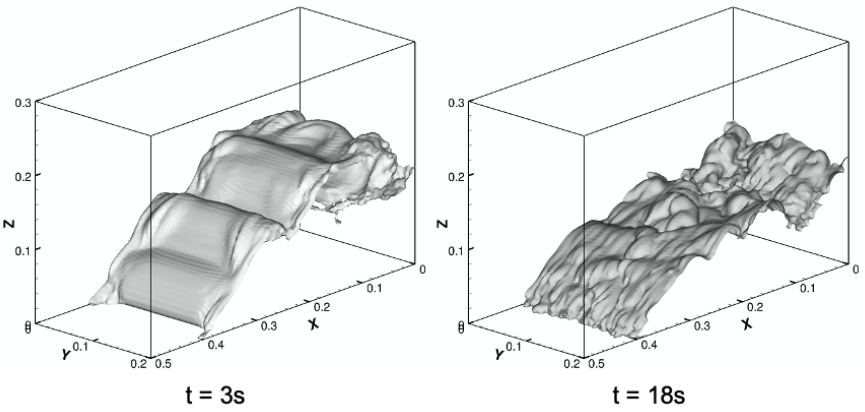

Figure 4.4: 3D view of the iso-surfaces of concentration fields at the DGC's head at 3s (left) and 18s (right). Results are obtained from case 9 shown in Table. 4.1.

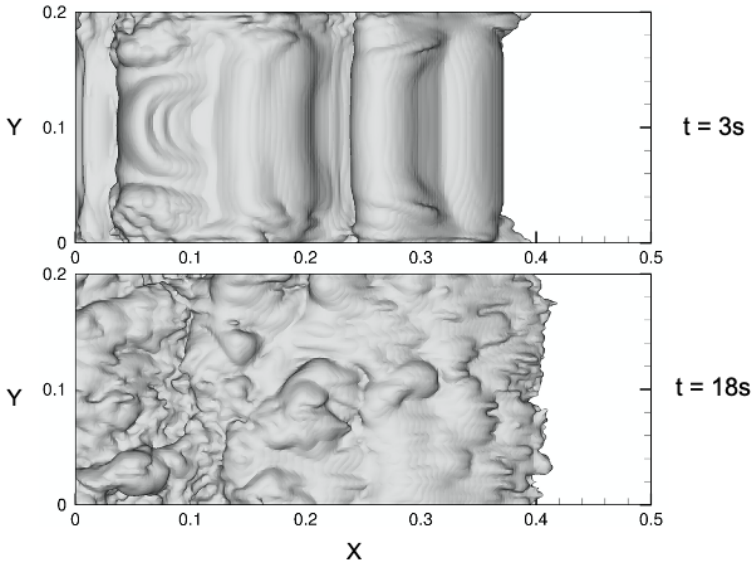

Figure 4.5: 2D view of the iso-surfaces of concentration fields closed to density-driven gravity currents (DGC)' head: top, at 3s; bottom, at 18s. Results are obtained from case 9 shown in Table. 4.1.

4.2.2 Particle-driven gravity currents: PPL-LES model

The performance of the PPL-LES model simulating particle-driven gravity currents (PGCs) is evaluated versus the experimental data gathered by [15]. The experiments were performed in a glass flume $10m$ long, $26cm$ wide and $48cm$ deep. Initially, the tank was filled to a height of $30cm$ with tap water. A lock gate is located $15cm$ away from the left wall. Non-cohesive silicon carbide particles were used as suspended particles, originally immersed within the water behind the lock gate. The average particle size was 9-53 μm and the density was $3217\,kg/m^3$. The initial suspended particles occupied the total mass from 100 to 800g (corresponding to 4×10^8 to 3.2×10^9 particles in total). And their volume fraction was always less than 2%, indicating that the influence of particles concentration on the flow field can be neglected. During the experiment, the gate is swiftly removed to release the turbidity current after a well-mixed suspension of particles in the locked area of the tank. Our PPL-LES numerical simulations reproduce these experiments by scaling them down, due to the disproportionate computational expense that simulating all particles would require. Two key parameters were carefully considered for the scaling, Froude and Richardson numbers (see Eq. 4.1).

$$Fr = \frac{V_{fm}}{\sqrt{h_0 g_0^{'}}} \tag{4.1}$$

where V_{fm} refers to the mean front velocity, h_0 represents the initial depth of water and $g_0^{'}$ is the induced gravity. The Richardson number is computed through Eq. 4.2.

$$Ri = \frac{\Delta\rho g h}{\rho u^2} \tag{4.2}$$

where $\Delta\rho$ represents the initial difference on density, u refers to the front velocity of currents and h is the initial depth of water. Several simulations are carried out

to examine the sensitivity of the current dynamics to the Froude and Richardson number. As shown in Table. 4.2, two cases (case 1 and case 2) are experimentally tested in the full-scale flume. By sliding gate, Case 1 is carried out by introducing the suspension of solid particles in the flume and case 2 adopts salt water without particles.

Case	L (m)	W (m)	H (m)	D_p (μm)	$g^{'}$ (m/s^2)	Fr	Ri	Gate removal
1	10	0.26	0.3	53	0.023g	0.23	37.8	Yes
2	10	0.26	0.3	None	0.023g	0.34	17.3	Yes

Table 4.2: Global experimental parameters for the particle-driven gravity currents [15]

As depicted in Table. 4.3, case 3 to 8 are conducted to simulate PGCs in a scaled flume with a different induced gravity by adjusting the weight value in Eulerian-to-Lagrangian interpolation function (See Eq. 2.24). Based on Eq. 4.1 and 4.2, the Froude and Richardson number can be computed for each case and compared with the laboratory-scale measurement (case 1 shown in Table. 4.2). On the other hand, three cases (case 9 to 11) simulate the saline water without particles and compare the Froude and Richardson number with the case 2 which is performed by [15] and shown in Table. 4.2. Moreover, case 9 and 10 are simulated in the same scaled flume as the case 3 to 9 with two different initial salt concentration, and case 11 is tested in the same full-scale flume as the experiments, which will be applied to discuss the influence of scaling computational domain on the prediction. In addition, sliding gate is not modelled in all the cases exhibited in Table. 4.3. In the following discussion, particle case refers to the case with particles and saline case refers to the salty water case without particles.

No-slip boundary conditions are imposed at all solid walls and the free surface is implemented a rigid lid with a symmetry condition, while the water on both sides of the lock gate is initially quiescent. The dispersed phase is composed by particles with

Case	L (m)	W (m)	H (m)	D_p (μm)	$g^{'}$ (m/s^2)	Fr	Ri	Gate removal
3	0.02	0.01	0.025	53	0.28g	0.28	25.5	No
4	0.02	0.01	0.025	53	0.276g	0.23	37.8	No
5	0.02	0.01	0.025	53	0.25g	0.22	41.3	No
6	0.02	0.01	0.025	53	0.20g	0.20	50	No
7	0.02	0.01	0.025	None	0.276g	0.30	22.1	No
8	0.02	0.01	0.025	None	0.25g	0.29	23.8	No
9	10	0.26	0.3	None	0.023g	0.35	16.3	No

Table 4.3: Global numerical parameters for the particle-driven gravity currents

a diameter of $D_p = 53\ \mu m$, which is the upper end of the size range used in the experiments. The inertial particles are initially distributed in the volume enclosed by the lock gate at the left of the flume, whose dimension is $0.02(L) \times 0.025(H) \times 0.01(W)$. The particle count is approx. 500,000, to match the experimental volume fraction and much less than less than 2%. The grid size in Eulerian framework is chosen as 0.3125mm to meet Milelli's particle-to-grid size recommendations. The time step is chosen as 0.0005s. The basic simulation parameters for the PGC validatios are summarized in Table. 4.4.

Parameter	Experiment	Simulation
Water Depth H(m)	0.3	0.025
Characteristic Length $L* = H/2$ (m)	0.15	0.0125
Flume width W(m)	0.26	0.01
Flume length L(m)	3.0	0.4
Particle size $D_p(\mu m)$	53	53
Particle density kg/m^3	3217	3217
Buoyancy velocity $u_b(m/s^2)$	0.18	0.18
Particle amount	1.6e9	500,000
Volume fraction	<2%	<2%

Table 4.4: Basic simulation parameters for the particle-driven gravity current [15]

Fig. 4.6 depicts a 3D view of particle propagation for the turbidity current defined in case 4 (Table. 4.3). It is important to note that the modelling approach within PPL-LES does not impose any sort of condition on the continuous phase, hence the only driver for the turbidity current is the fluid entrainment within the

particle-laden flow. The current is driven by the settling of inertial particles and the local density variations induced by the particle concentration. Half a million particles were initially clustered and uniformly distributed within a 15 cm length at the left end of the flume. The combined weight of all these suspended particles produces a down-burst that rebounds against the flume's bottom generating the characteristic current's head, which resembles a breaking wave. This vertical motion is accompanied by a rapid horizontal propagation towards the undisturbed end of the flume. All throughout the process some particles settle on the flume's bed creating the tail of the current, while others, particularly at the head, are advected forward and upwards by the entrained liquid.

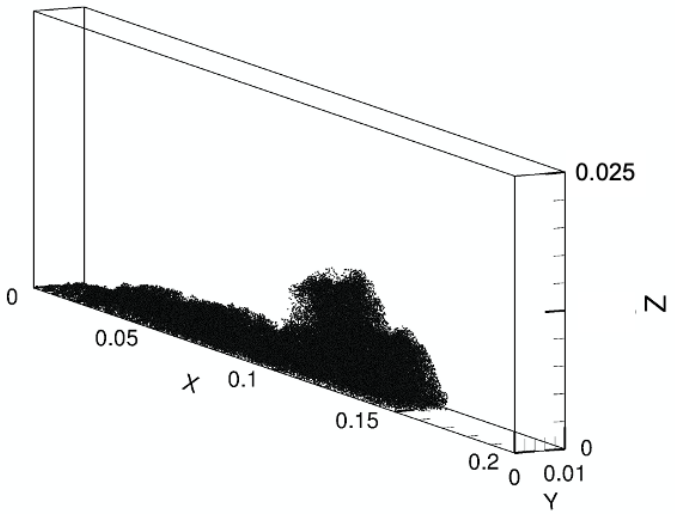

Figure 4.6: PGC produced by lock exchange in an Eulerian-Lagrangian framework: particle size $53\mu m$; particle count 500,000; initial induced gravity 0.19g m/s^2.

Fig. 4.7 offers a comparison between the PPL-LES prediction and the experimental results by [15], where red crosses and squares represent saline and particle case in the experiments respectively. These two cases' numerical results are represented by dotted lines (saline case) and solid lines (particle case). The graph tracks the front position versus time. The characteristic length $L*$ calculated as the half of water depth ($L* = H/2$) is used to normalise both axes, where non-dimensional front position is computed by $xf^* = xf/L*$ and non-dimensional time is calculated by $t* = tu_b/(L*)$ (see Table. 4.4). The circles linked by dotted line refer to the

real-scale numerical simulation and the rest of them represent scaled down numerical simulations of which froude and Richardson number have been validated with the experiments (see Table. 4.3). In general, the results depict a good agreement between the experimental measurements and the PPL-LES predictions for the two types of case. With regards to the saline case, real-scale simulation (case 9) exhibits a more closer to the experimental results than the two scaling numerical cases (case 7, case 8) which have a similar under-prediction on the front velocity at later stage ($t* = 60$ to $t* = 100$). These slight differences suggest the influence of scaling issues on the prediction of gravity currents. As discussed in Section 3, it is impossible to numerically reproduce all particles in the experiments and scaling simulation is a good option to simulate particle-driven gravity current. The cases 3 to 6 present the numerical results predicted by different Froude number, 0.28 (case 3), 0.23 (case 4), 0.22 (case 5) and 0.2 (Case 6). It can be observed that the front velocity for 4 cases predicted by the code solver is a bit slower than the experimental measurements at earlier stage ($t* = 10$ to $t* = 30$). And the time from $t* = 30$ to $t* = 60$ exhibits a very well agreement with the experimental results for 4 cases. The case 3 (Fr = 0.28) shows the predicted front arrives at a similar distance but terminates at earlier time comparing to the experiments. The predicted fronts in case 4 to 6 (Fr=0.23, 0.22 and 0.2) depict a more closer agreement with the experiments than the case 3. The results suggest that Froude number is a crucial parameter in the scaling simulating of gravity currents driven by inertial particles and a higher value is able to result in an under-estimation on the front velocities.

4.3 Particle-driven gravity dynamics

In this part, the case 4 shown in Table. 4.3 is used to analyse the hydrodynamics of particle-driven gravity current and other cases shown in the table are applied for the

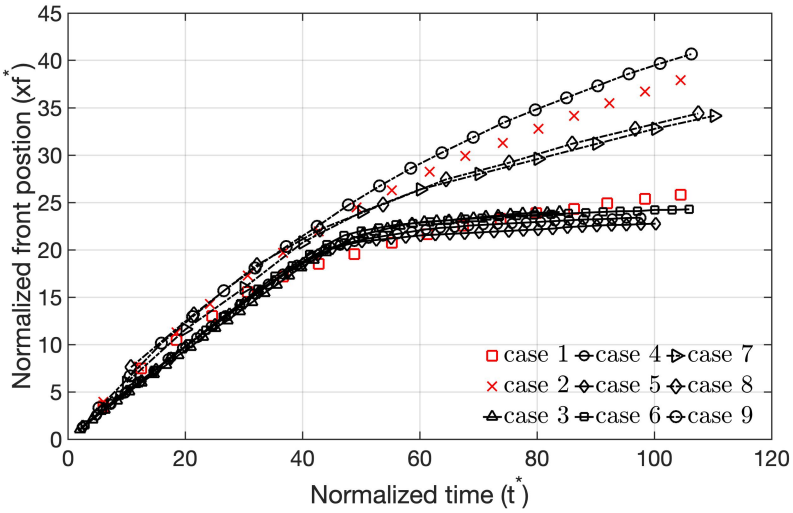

Figure 4.7: Comparison on temporal evolution of the normalized front position for particle-driven gravity current: symbols, experimental results [15]; symbols linked by lines, numerical results.

comparison and validation. Fig. 4.8 presents the results of PPL-LES for the particle-driven gravity current (case 4) superimposed on the normalized vorticity field at simulation times 0.2s, 0.8s, 1.2s, 1.6s and 2.0s. These five times are normalised as 2.94, 11.77, 17.66, 23.55 and 29.43. The results at t=0.2s illustrates how the release of the inertial particles after the lock gate is removed results in the formation of the head of gravity current, while Kelvin-Helmholtz vortexes form at the interface with the unladen liquid matrix. Since the particles form the turbidity current, the unladen liquid occupies the space that was initially behind the gate and hit the flume's left wall ($t*$=11.77 and $t*$=17.66). The vorticity field at the tail becomes rather complex due to the interaction of the aforementioned flow running leftwards through the top and the wake of the vorticity originated at the shear layer. At $t*$=11.77 and $t*$=17.66, the ambient fluid rolls up and strong vortexes are generated on the interface between the fluid driven by inertial particles and the unladen liquid due to the shear instability. A very notable feature is the gradual sediment trail left by the current, where the higher vorticity field is observed near the sedimentation layer. At $t*$=23.55 and $t*$=29.43, the vorticity magnitude gradually drops due to the loss of inertia as particles settle and the viscous forces; such decrease is reflected

in the PGC's head.

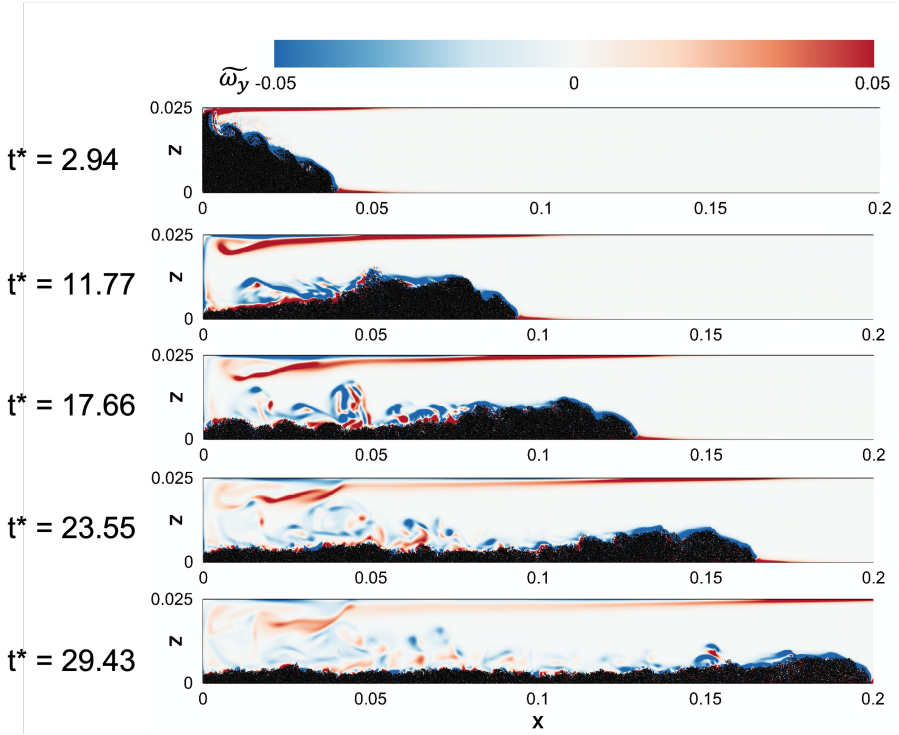

Figure 4.8: Evolution of the particles driving the PGC (case 4 in Table. 4.3) superimposed on the normalized vorticity in the middle plane of the flume at non-dimensional simulation times 2.94, 11.77, 17.66, 23.55 and 29.43.

Fig. 4.9 provides a qualitative insight on the dynamics of particles at early stage of the current's development. Fig. 4.9(a) presents the vertical profile of the ensemble density $\Psi(z,t) = \frac{1}{L_x}\int_0^{L_x} \rho(x,z,t)dx$ induced by the suspension of particles across the entire length and width of the flume. The solid and dotted lines signal $t* = 2.44$ and $t* = 4.88$ respectively, which are calculated by $t* = tu_b/(L*)$. Figs. 4.9(b) and (c) show the cross-sectional distribution of inertial particles and the isolines of induced density $\rho(x,z,t)$ at those very same times. Fig. 4.9(a) shows four significant peaks of at $t* = 2.44$, whose magnitude decreases from bottom to top. Those peaks correlate rather closely with the presence of Kelvin-Helmholtz vortices, as observed in Fig. 4.9(b). At $t* = 4.88$, two peaks at approx. $z = 0.005$ and $z = 0.01$ seem to be related to the current's head and the fluctuations at its top, since the structure of the original vortices has been disspated in its majority (Fig. 4.9(c)).

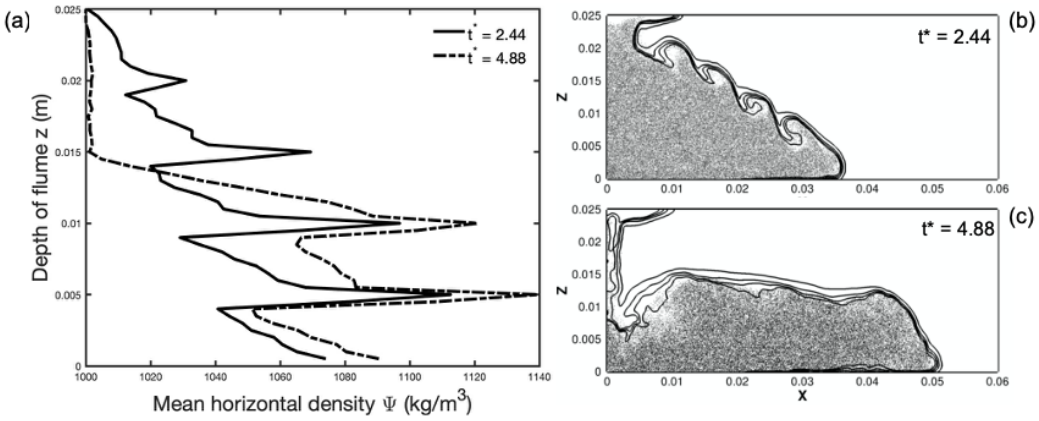

Figure 4.9: Results for case 4 shown in Table. 4.3: (a) Mean vertical density profile Ψ: solid line, $t* = 2.44$; dash line, $t* = 4.88$. (b) Particles distribution superimposed by isolines of density at $t* = 2.44$. (c) Particles distribution superimposed by isolines of density at $t* = 4.88$

4.3.1 Density versus Particle-Driven Current

Figs. 4.10 and 4.11 compare the density iso-surface that defines the interface between heavier/particle-laden fluid and lighter fluid for PGCs (left) and DGCs (right), respectively. Both simulations (case 4 and 7 shown in Table. 4.3) share the same computational domain and induced gravity, i.e., density ratio. The front velocity of the DGC is faster under the same conditions. And the 3D view presented in Fig. 4.10 shows how the DGC depicts a smooth and symmetric interface at the head of the current, whereas the PGC triggers more small scale perturbations. These instabilities are even more notable as we move towards the current's tail, where the wakes of the successive vortices interact non-linearly.

The top down view provided by Fig. 4.11 shows symmetric loft-and-cleft structures in the DGC where the concentration field remains rather homogeneous and the flow within the currents is in a more stable regime than PGC. Whereas the symmetric features are not shown in the particle case due to the presence of the inertial particles triggering the flow field into a turbulent regime very quickly.

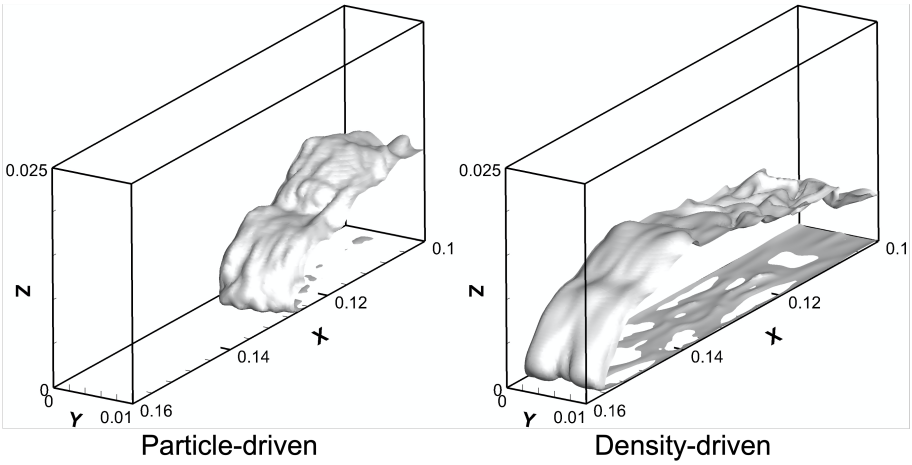

Figure 4.10: 3D view of the gravity current's head for PGC (left) and DGC (right) at $t* = 30$. Results obtained from case 4 and case 7 shown in Table. 4.3.

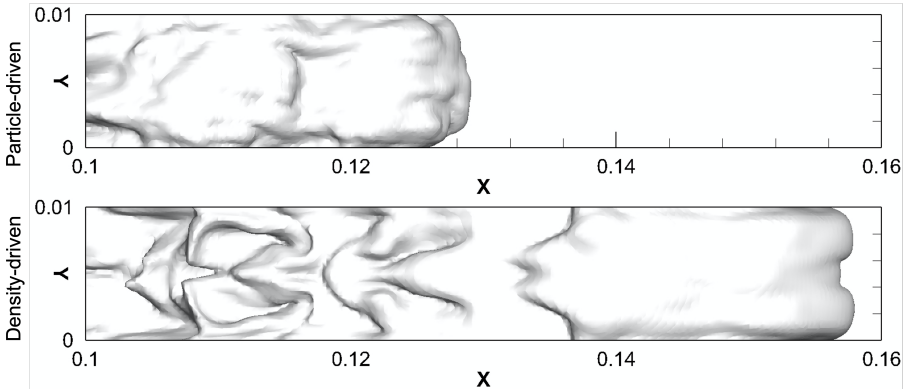

Figure 4.11: 2D view of the gravity current's head for PGC (top) and DGC (bottom) at $t* = 30$. Results obtained from case 4 and case 7 shown in Table. 4.3.

4.3.2 Particle settlement and re-suspension

Fig. 4.12 shows the map of the final deposited particles for three cases with different induced gravity, which are 0.20g m/s^2, 0.25g $m/s^2$and 0.276g m/s^2, corresponding to case 4 to 6 in Table. 4.3. For clarity, one point in the figure represents five solid particles in the simulation. It is noticeable that the particles accumulated with the propagation form the tail of the current and the other particles move forward under the gravity and forms the head of the current, which finally establishes a sediment layer in the streamwise direction for each case. A heavier suspension (i.e., higher induced gravity) results in the PGC travelling further. Also, the 0.20g case seems to produce intense banding in the spanwise direction. This can also be appreciated in the other cases but the symmetry is lost.

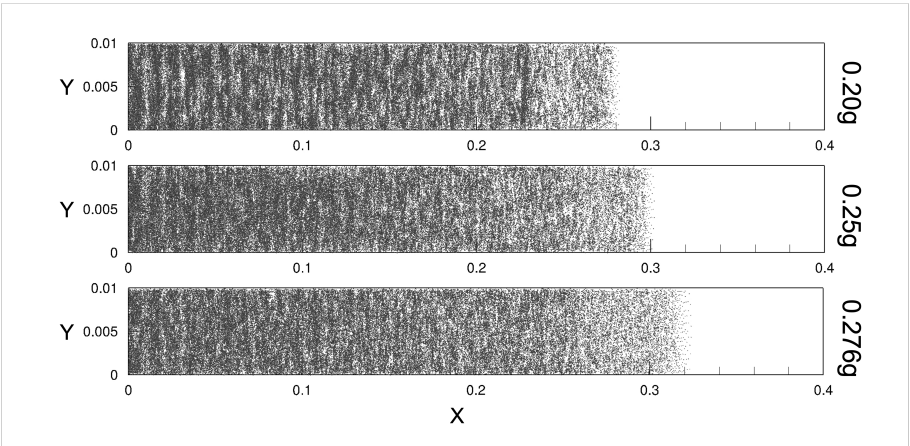

Figure 4.12: Top down view of the final sedimentation map at $z = 0.001$ for three simulations with different induced gravity: top, 0.20g m/s^2; Middle, 0.25g m/s^2; bottom, 0.276g m/s^2.

The sedimentation profile in the streamwise direction is calculated and presented in Fig. 4.13. The red circles represent the experimental measurements [15] and the three curves refer to the PPL-LES predictions for 0.2g m/s^2, 0.25g m/s^2 and 0.276g m/s^2 respectively, which corresponds to the three cases depicted in Fig. 4.12. Numerical and experimental results share the basic same trend; the experiments however report the maximum of settled particles at x/L approx. 7.5, whereas the

numerical results predict a plateau in the range 0-10. Beyond x/L=10, the density of settled particles falls more abruptly for the experiments, whereas the numerical model predicts another short plateau near the current's head followed by a sudden decrease. Such slight differences could be attributed to prior stirring of the particle suspension before the gate removal in the experiments, among other factors [110, 117].

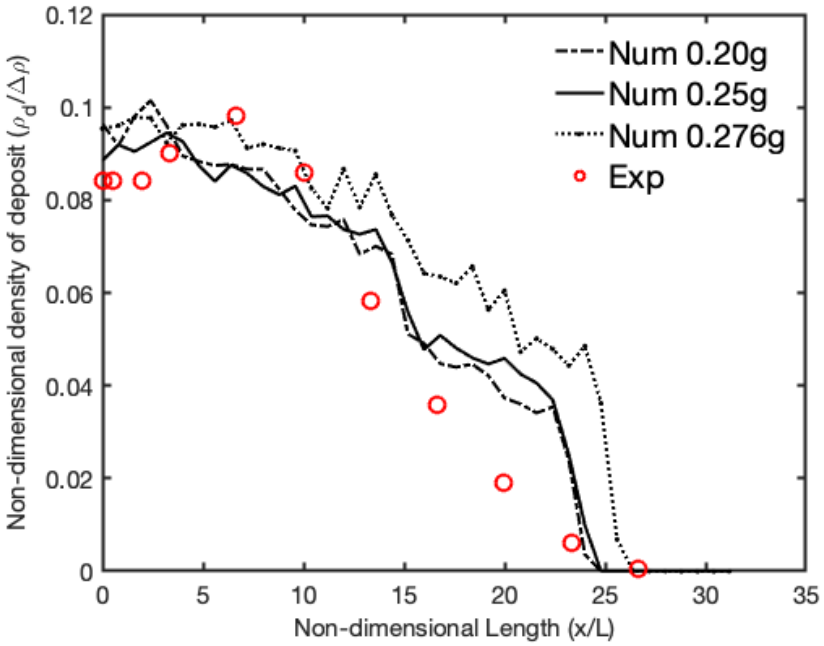

Figure 4.13: Final particle deposition profile for PPL-LES (lines) and experimental measurements (red circles).

To investigate the dynamics of near-wall region, local friction velocity at the bottom of the tank is computed as follows,

$$u_\tau = \frac{\tau_w}{\rho} \tag{4.3}$$

where τ_w represents the wall shear stress, which can be calculated,

$$\tau_w = \mu \sqrt{\left(\frac{\partial u}{\partial z}\right)^2 + \left(\frac{\partial v}{\partial z}\right)^2}\Bigg|_{z=0} \tag{4.4}$$

where μ refers to dynamic viscosity, u and v represent the velocity in streamwise

and spanwise direction.

Fig. 4.14 offers insight on the dynamics of the local friction velocity u_τ on the bottom wall of the flume during the PGC's propagation at dimensionless times 15, 30 and 60. The results correspond to case 4 shown in Table. 4.3. The left column shows contours of friction velocity at the bottom wall, where darker contour represents larger friction velocity, and the right column indicates the spatial distribution of the friction velocity at the flume's centreline. Larger friction velocities are located at the head of the currents during earlier stages ($t* = 15$ and $t* = 30$), with the maxima reaching around u_τ=0.01 m/s. These maximums seem to propagate backwards transported by the vorticity, where loft-and-cleft structures are generated within the interface between the heavier and lighter fluid.

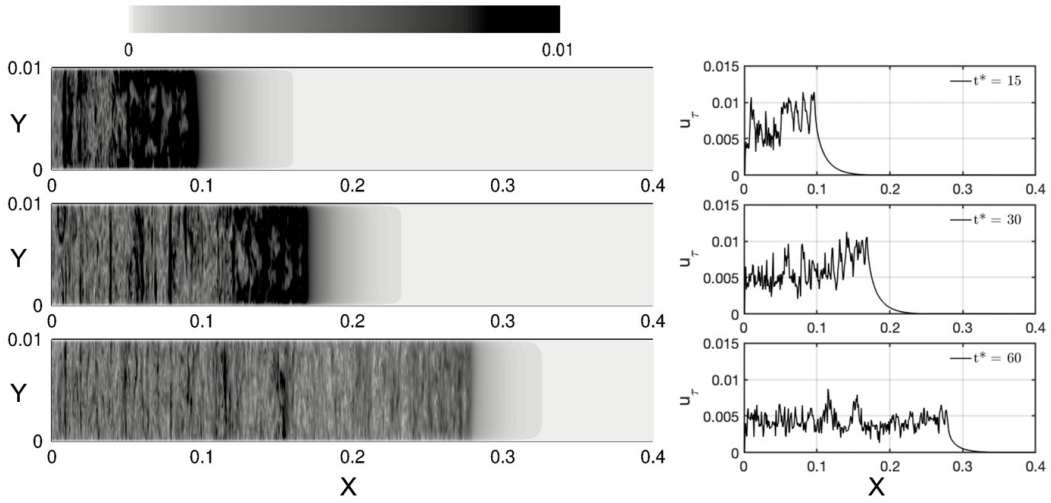

Figure 4.14: Left: Local friction velocity u_τ at the bottom wall contoured by gray-scale: top, $t* = 15$; middle, $t* = 30$; bottom, $t* = 60$. Right: Local friction velocity u_τ in the streamwise direction at $y = 0.005$: top, $t* = 15$; middle, $t* = 30$; bottom, $t* = 60$

Fig. 4.15 exhibits the time history of the u_τ maxima at each time step over the flume's bottom for case 4 in Table. 4.3. The results show a general decreasing trend with several particular features. The friction velocity reaches the maximum value

at about $t* = 5$ and drops between $t* = 5$ and $t* = 10$, and the second peak is reached at about $t* = 40$ after a slight fluctuation. To analyse the possibility of resuspension of particles quantitatively, the criterion proposed by [103] is considered in here. A dimensionless wall shear stress θ usually called as the Shields parameter and the Reynolds number for particles Re_* are computed as follows,

$$\theta = \frac{\rho u_\tau^2}{(\rho_p - \rho) g d_p} \tag{4.5}$$

$$Re_* = \frac{u_\tau d_p}{\nu} \tag{4.6}$$

where ρ and ρ_p refer to the density of ambient fluid and particles, d_p represents the diameter of particles and g refers to the gravitational acceleration. The parameter θ quantifies the ratio of the fluid force on the particles to the weight of particles. For a particle Reynolds number, the higher value of θ indicates that the particles are more likely to be entrained by the local flow field. According the maximum of the friction velocity u_τ, θ and Re_* can be obtained as 0.43 and 1.1 for the first peak, 0.39 and 1.1 for the second peak, which slightly beyond the limit and exhibit that the settled particles may experience the entrainment and resuspension.

4.3.3 Dissipation rate budget in a turbidity current

The fluid motion of gravity currents is challenging to understand since the turbulence is not only generated by density variance in carrier fluid but induced by the dispersed particles. The energy budget of the turbulence is of importance to study how a wide of scales travel in gravity currents fundamentally. In this paper, the dissipation rate of turbidity currents driven by inertial particles is discussed by considering the time evolution of the dissipation rates for: a) the kinetic energy of the ambient fluid

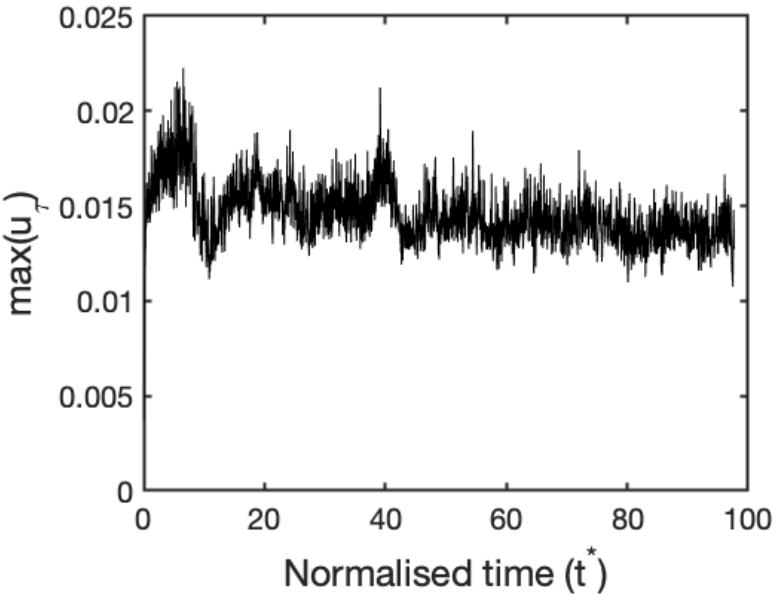

Figure 4.15: Time evolution of the global friction velocity maximum over the flume's bottom.

(Eulerian phase) ϵ_k, b) the particle-induced kinetic energy (Lagrangian phase) ϵ_{kp}, the particle-laden region of the domain ϵ_{pl}, the un-laden region of the domain ϵ_{ul} and the entire system ϵ_t. Each of them was computed as follows:

$$\epsilon_k = -\frac{dE_k}{dt} = \frac{\int_\Omega \frac{1}{2}(u_l^2 + v_l^2 + w_l^2)dv}{dt} \tag{4.7}$$

$$\epsilon_{kp} = -\frac{dE_{kp}}{dt} = \frac{\frac{1}{np}\sum_{p=0}^{np} \frac{1}{2}(u_p^2 + v_p^2 + w_p^2)}{dt} \tag{4.8}$$

$$\epsilon_{pl} = 2\nu \int_0^{x_{pl}} \int_0^{x_2} \int_0^{x_1} S_{ij} S_{ij} dx_1 dx_2 dx_3 \tag{4.9}$$

$$\epsilon_{ul} = 2\nu \int_{x_{pl}}^{x_3} \int_0^{x_2} \int_0^{x_1} S_{ij} S_{ij} dx_1 dx_2 dx_3 \tag{4.10}$$

$$\epsilon_t = 2\nu \int_\Omega S_{ij} S_{ij} dV = \epsilon_p + \epsilon_{ul} \tag{4.11}$$

where the velocity represented by the notation l and p refer to the velocity of the ambient fluid and particles, S_{ij} represents the mean strain-rate tensor and ν refers to kinematic viscosity. Fig. 4.16 displays the time evolution of the aforementioned dissipation rates for case 4. Two sets of trends are observed: the dissipation rates of kinetic energy (ϵ_k and ϵ_{kp}), calculated from the Eulerian and Lagrangian velocity fields respectively, exhibit negative values until approx. t^*=10, reflecting a positive growth of kinetic energy in the early development of the lock exchange and the current's acceleration. Overall, ϵ_k and ϵ_{kp} present lower magnitudes than the ones modelled through the strain rate tensor (ϵ_{ul} and ϵ_{pl}), and alternate dissipation and production throughout the simulation. These two share a similar trend, ϵ_{pl} being the main contributor to the total dissipation ϵ_t. The t^*=0-10 range is characterised by a plateau of high values with a peak preceding a sharp downfall (and another one at the very start for ϵ_{pl}). From that point on, the magnitude of the dissipation gradually decreases as the current settles, with several characteristic peaks:

- t^*=15-30: two very notable peaks in ϵ_{pl} aligned with two kinetic energy production events reflected by ϵ_k<0 and a wide peak in ϵ_{ul} at t^*=20.
- t^*=35-45: another two-peak event on ϵ_{pl} aligned with a strong fluctuation in ϵ_k and a single peak in ϵ_{ul} inbetween them. Compared to the previous one, the magnitude of the peaks in ϵ_{pl} has decreased heavily but increased slightly and narrowed for ϵ_{ul}. This is in agreement with the observation made in Fig. 4.14: settled particles resuspend and trigger perturbations from the particle-laden region into the far field, exchanging energy between the two fractions.

The comparison between ϵ_{ul} and ϵ_{pl} indicates that the kinetic energy dissipation rate is mostly contributed by particle motion. In addition, ϵ_{field} indicates a hump-shaped response occurring near $t* = 40$, corresponding to a lowland-shaped tendency in the response of ϵ_{sed}.

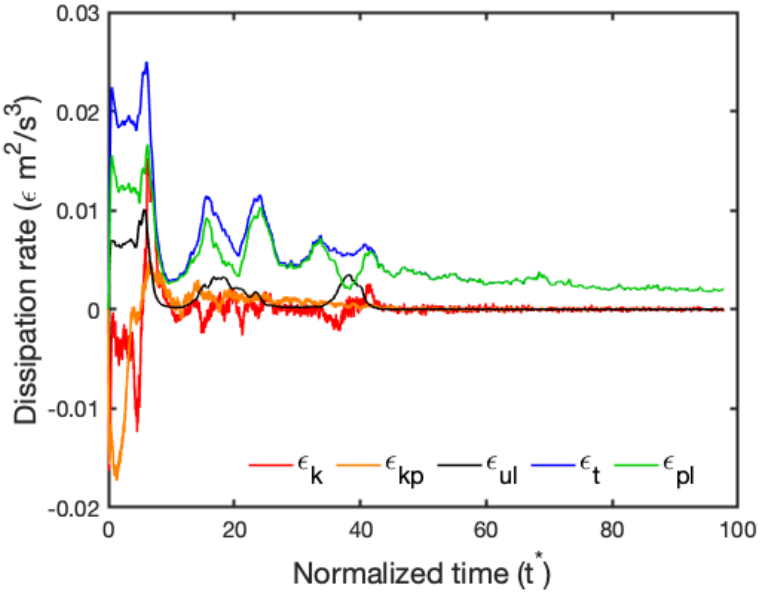

Figure 4.16: Temporal development of energy dissipation rates: whole system ϵ_t (blue); particle-laden region ϵ_{pl} (green); unladen region ϵ_{ul} (black); kinetic energy of ambient fluid ϵ_k (red); kinetic energy of particles ϵ_{kp} (orange).

4.3.4 Effect of lock gate removal

Commonly in lock-exchange simulations, the initial velocity field of the ambient fluid is assumed at rest, which is not the case in laboratory setups[110]. We simulated the effect of the gate removal on PGCs using a sliding immersed boundary gate that moves upwards at a non-zero velocity inducing shear on both sides. Fig. 4.17 shows a mid-flume lateral view of the vorticity field at the point the gate is about to be completely lifted. Superimposed on the left side of the gate the density of intertial particles, colour-coded by their Lagrangian density, can be appreciated. The gate slides upward at 1.0 m/s velocity and generates two significant symmetrical vortexes near the top of the tank. These eddies seem to contribute to the inertia of the particle-laden fraction whereas prevents the initial intrusion of clean water in the locked area.

The effect of the velocity of the lock gate was tested comparing two sliding ve-

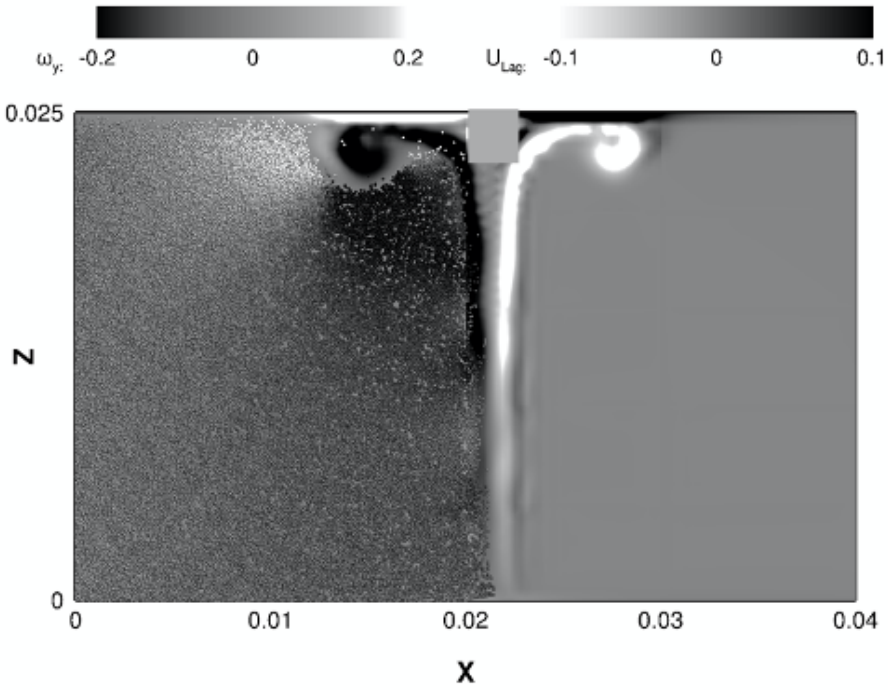

Figure 4.17: Normalised vorticity of the ambient fluid and particle distribution at the initial stage of the PGC, with the lock gate almost completely lifted. Results are obtained at the slice $y = 0.005$.

locities (0.25 and 1.0 m/s). The results are collected in Fig. 4.18. Three parameters are examined, including the kinetic energy generated by the fluid matrix and particles (k_{Eul} and k_{Lag} respectively), the dissipation rate in system (ϵ_t) and the density profile Ψ at $t* = 2.44$. Fig. 4.18a shows the response of kinetic energy for three cases: no gate, gate sliding up at 0.25 m/s and gate sliding at 1.0 m/s. The lines representing the sliding gate cases exhibit a significant increase on k_{Eul} and k_{Lag} at the initial stage ($t* = 0$ to $t* = 5$) compared to the case without removing gate. This initial peak in kinetic energy relaxes and the trends of all cases become very similar, yet there are long term effects. The Lagrangian kinetic energy remains slightly higher across the whole simulation for the sliding gate cases. Regarding k_{Eul}, the faster sliding gate has a long-lasting effect in the long term. As shown in Fig. 4.18b, the dissipation rate (ϵ_t) before $t* = 5$ experiences a sharp increase in the sliding gate cases, particularly for the faster case. There are significant differences in the long-term evolution of ϵ_t among the three cases, with a particularly

more accentuated evolution of the faster case. The results depicted in Fig. 4.18a and Fig. 4.18b suggest that the gate removal has a distinctive effect on the energy budget of PGCs at an earlier stage, with non-negligible long term effects. Fig. 4.18c depicts the contribution of the sliding gate to the density profile Ψ at $t* = 2.44$, mirroring the prior discussion for Fig.4.9. The comparison highlights the differences in the region z =0.015-0.025, suggesting that the sliding gate can potentially contribute to the generation of Kelvin-Helmholtz vortices near the top of the tank.

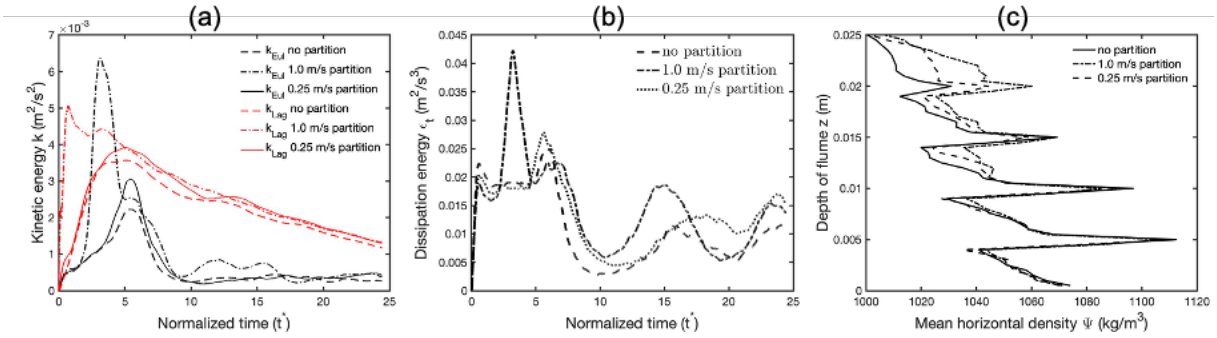

Figure 4.18: Contribution of the sliding gate velocity to PGCs: (a), kinematic energy of ambient fluid (k_{Eul}) and particles (k_{Lag}); (b) dissipation rate ϵ_t; (c) density profile Ψ at $t* = 2.44$.

4.4 Conclusions

This paper uses two different LES-based modelling approaches to simulate two different types of gravity currents. The main focus is the description of the mechanisms of propagation of particle-driven or turbidity currents, for which a point-particle Eulerian-Lagrangian algorithm was developed, introducing a soft-sphere collision model and four-way coupling. To provide an element of comparative analysis and prove further the robustness of our solver, density-driven gravity currents were also simulated throughout a dusty gas approach incorporating the Boussinesq approximation.

Our model was validated by comparing the predictions for both cases with the experimental data provided by [1] and [15]. Such validations were centered, but not restricted, to the analysis of both density-driven and particle-driven currents' front velocity. Additionally, current profiles and particle distribution and deposition profiles were also compared in detail. This is the first systematic validation of an Eulerian-Lagrangian approach to investigate the influence of the inertial particles on turbidity currents. The results predicted by these two approaches exhibit a remarkable agreement with the experimental measurements across a comprehensive parameter range. Our Eulerian-Lagrangian simulations are capable of capturing the formation and evolution of Kelvin-Helmholtz vortices at the currents' shear layer, the consequent entrainment of ambient fluid and the progressive settlement of particles as the turbidity current progresses.

The next step consisted on comparing analogous cases (same domain and density ration) of particle- and gravity-driven currents to analyse differences in their dynamics that can only be attributed to the nature of the suspended particles in the former case, and therefore only captured by a modelling approach that respects the discrete nature of the individual particles. Notable differences were found: turbidity currents are significantly slower than gravity currents, they are less persistent, they transition to turbulence faster and develop increased multi-scale and asymmetric loft-and-cleft structures.

Motion in turbidity currents is governed by the transfer of potential and kinetic energy from the dispersed phase to the ambient fluid. Liquid entrainment and particle re-suspension oppose particle settlement. The latter is responsible for the non-conservative nature of turbidity currents and governs the bed shear stress. The particle deposit maps provided by our simulations agree with experimental measurements, although the numerical predictions show a slightly more homogeneous distribution of particles along the current. Slumping and rebound events were

identified and related to the generation of transient flow structures and particle resuspension. The quantification of the dissipation rate of the kinetic energy shows that the current is set in motion via transfer of turbulent kinetic energy from the dispersed phase to the continuous phase, albeit the resolved turbulent scales of the ambient liquid govern the entrainment. Within the sub-grid scales, dissipation is mainly produced in the particle-laden region, which leads to an interesting question: are current sub-grid models suitable for these types of flows?

Finally, the influence of the physical removal of the lock gate on the current propagation is analysed. Such effect was simulated using an immersed boundary sliding gate. Our results reveal that little to no difference was found between an unrealistic instantaneous disappearance of the gate and a slow removal. However, fast removal of the gate has a critical effect in increasing the kinetic energy at the beginning of the simulation and triggering water intrusion in the lock region. This influence is mostly relevant in the early stages of development of the current, albeit non-negligible long-term effects on the agitation were observed along its propagation.

Acknowledgements

The computational works described in this paper were performed using the University of Birmingham's BlueBEAR HPC service and the Athena at HPC Midlands+ which is funded by EPSRC. The authors are grateful for the support provided by the University.

Chapter 5

A Three-phase Eulerian-Lagrangian Model for Activated Sludge Treatment

The work is presented in $39th$ IAHR World Congree 2022

Submitted to International Journal of Multiphase Flows (under review)

CRediT authorship contribution statement:

1. Literature review on experimental research on activated sludge process.

2. Implement the mass transfer in the code to solve evolution of dissolved oxygen in wastewater.

3. Design numerical simulations of wastewater treatment plants.

4. Post-process numerical results and compare them with experimental measurements.

5. Draft the original manuscript, review and edit it.

5.1 Introduction

The largest expense in wastewater treatment occurs in secondary treatment, particularly for activated sludge process (ASP) [101]. ASP is based on forced aeration, promoting the redistribution of dissolved oxygen to facilitate the microbial growth. The activated microbial feeds on organic material, forming flock which can settle out and be removed in the final clarifier. This process is designed to speed up the rate of decomposition in wastewater and improve the quality of effluent, and has been extensively applied in wastewater treatment plants (WWTP) around the world. Aeration is the major contributor to energy expenditure in wastewater treatment, accounting for 60% of total energy consumption in ASP [131, 54]. In practice, there are two main types of aeration system, including diffused air and surface aerator. The latter one is simply implemented by installing turbines on the surface of aeration tank and injecting air into wastewater. The former one generates buoyant plumes at the bottom of tank and performs more efficiently than the latter one in terms of mixing and increasing DO levels [139]. A well-designed aeration system is critical to an effective and sustainable wastewater treatment [19]. However, engineers are often forced to rely on empirical guidelines due to the lack of accurate models and an overall design tool [58].

Extensive laboratory experiments were conducted to investigate ASP, mostly focusing on the biological characteristics of activated sludge and the dissolved oxygen (DO) concentration in wastewater [161, 172]. Some experimental research was carried out in full-scale WWTP and continuously monitored the sludge concentration for months, exposing a remarkable influence of DO levels on the decomposition of organic material and the respiration of aerobic bacteria [160, 79]. In order to shorten the length of the experiments and test more efficiently the factors affecting the activated sludge's growth, some researchers sampled the wastewater flowing into the

aeration tank and measured the activated sludge concentration in a laboratory-scale tank [120]. Overall, the experiments focus on the general performance of ASP and often explore that under a limited number of design alternatives. There are many complex flow phenomenons encountered in ASP, including the suspension of sludge in wastewater, sediment transport near the bottom of aeration tank and mixing of dissolved oxygen by buoyant plumes, that received less attention. With the rapid growth in computational resources, computational fluid dynamics (CFD) technology capable of simulating the behavior of such flows is increasingly available to analyse the flow properties in activated sludge process and improve the design of ASP from a fluid dynamics perspective.

ASP is a complex gas-liquid-solid three-phase flow involving the raise of bubble swarms and the settling of solid particles within a liquid matrix, requiring a thorough understanding on the fluid mechanisms of buoyant plumes and particle-laden flows. The biochemical kinetics encountered in this process require an accurate prediction of the dissolved oxygen distribution. DO concentration is heavily dependant on the turbulent mixing triggered by bubble plumes, the superficial transfer occurring at the individual bubbles and the adsorption by the sludge [82]. With a wide range of scales of motion implicated, it is necessary to predict accurately the shear layers generated by the individual plumes in order to describe the formation of recirculation cells within the aeration tank while simultaneously forecasting the in-plume dynamics in order to predict the entrainment of surrounding fluid and the generation of turbulent kinetic energy within the bubble swarm. It is important as well to characterise instantaneous flow properties since instabilities caused by dispersed phases (plumes and solid particles) and plume-wandering contribute to the mixing process, hence a steady modelling approach naturally tends to overlook these mechanisms.

An accurate treatment of the continuous (liquid) and dispersed (bubbles and solid particles) phases as well as the coupling and interaction between the three phases is

critical to provide a reliable prediction for ASPs. Regarding the turbulence closure for the continuous phase, there are three fundamental modelling alternatives: Direct Numerical Simulation (DNS), Large Eddy Simulation (LES) and Reynolds-Averaged Navier-Stokes Simulation (RANS). LES is an usual choice to obtain the simulation of realistic and high-Re multiphase flows since this model can explicitly capture the instantaneous large-scale turbulence structure and model the less energetic small-scale structures through a subgrid-scale (SGS) model [47]. Moreover, LES-based simulations respect the anisotropic and transient nature of the dispersed phase [60, 17] and have extensively applied to solve practical multiphase flows (i.e. buoyant plumes and particle-laden flows) [78, 14].

Regarding the dispersed gas and solid particle phases, the fundamental modelling choices are: do we preserve their discrete nature? And do we resolve the interface between the bubble/particle and the liquid matrix? Consequently, modelling the dynamics of rising gas bubbles, falling inertial particles or suspended solids can be compartmentalised within three basic approaches: interface-solving (IS) methods, point-particle Lagrangian (PPL) algorithms and continuous Eulerian-Eulerian (EE) models. Interface-solving involves a number of algorithms that define and track the boundary between the dispersed and continuous phase, such as volume of fluid, front-tracking algorithm, immersed boundary method or level-set method. These models are extremely useful for fundamental research on multiphase flow dynamics for particles with characteristic lengths d_p above the Kolmogorov scale η [11]. When IS methods are applied to particles such as air bubble or suspended sludge of flocs in wastewater, their relatively small size compared to the characteristic scales of the surrounding fluid compels the modeller almost inexorably to use DNS on the continuous phase. The resulting high computational cost of limits therefore the application of interface-solving strategies to flows of industrial interest [169, 99]. EE approaches compute the dispersed phase on a continuous Eulerian framework, in-

troducing a void/solid fraction variable to calculate the coupling and the interaction between the two phases [93]. EE has been applied successfully to bubbly flows and particle-laden flows of practical interest [53, 48, 138, 152, 46, 85, 10]. However, the recent research exposes some drawback of this model: fraction field cannot naturally forecast the physics of the dispersed phase and its interaction with the continuous phase (i.e. entrainment between the different phases and settling of the particles of which density is higher than the carrier flow [22]); the treatment of boundary condition for the particles overlooks their reaction to the boundary, such that the particles rebound from the solid wall [115]; concentration field struggles to simulate the effect of polydispersed distributions with a wide range of sizes [11] since the particle size often modelled indirectly through single-value parameters such as the terminal velocity, which characterise all the particles within the continuum mixture. PPL models do not need to impose artificial assumptions on the bubble/particle size distribution nor the Reynolds number Re_p [149, 60, 59, 20, 30]. Within this approach the dispersed phase is described in a Lagrangian manner, whereas the continuous one corresponding to the liquid matrix is calculated in an Eulerian framework, i.e. a computational grid fixed in space. The interaction between both phases is modelled depending on the particle size and concentration [50]. One-way coupling is employed where the advection of the carrier flow is dominant and the dispersed phase behaves in a nearly passive manner. With bubbly flow, due to the high density ratio between air bubbles and water, bubble buoyancy has a rather disruptive effect on the surrounding liquid, requiring a two-way coupling approach which is acceptable for dilute bubble concentrations. For particle-laden flow with dense particle concentration, the particle-to-particle interaction must be considered by four-way coupling approach [77, 109].

Several works have applied three-dimensional non-Hydrostatic CFD coupled with biochemical kinetics to investigate ASP in wastewater treatment plants, including

aerator tank and oxidation ditch. Y. Le Moullec et al. [92] explored the hydrodynamics in activated sludge reactors with a RANS-based Eulerian-Eulerian algorithm (EE-RANS). The authors applied an established activated sludge model ASM1 in Eulerian framework to simulate the biological reactions driven by flow dynamics and compared the results with experimental measurements of chemical oxygen demand (COD) and dissolved oxygen concentration (DO) concentration. The comparison on oxygen mass transfer exhibits a remarkable under-prediction due to assuming that the flow field in reactor is steady-state. In order to examine the influence of sludge on the flow properties in ASP, H. Xie et al. [166] used EE-RANS model to study the velocity field induced by the settling of sludge in a full-scale oxidation ditch, where the empirical slip velocity was introduced to characterise the dynamics of sludge. Their results justify that a more accurate treatment of sludge phase is able to enhance the accuracy of numerical model forecasting ASP. By applying EE-RANS coupled with biokinetic models, R. Sánchez et al. [138] investigated activated sludge under aeration and compared different strategies for distributing the aeration device (air diffuser), showing that the efficiency of aeration system is sensitive to the number of blowers and air flow rate in terms of transporting oxygen in liquid. However, their results desire a further validation with experimental measurements with regarding the hydrodynamics of sludge and aeration. A. M. Karpinska et al. [84] applied LES to investigate the hydrodynamics of sludge in an oxidation ditch, where activated sludge in wastewater are described as the suspension of solid particles and modelled by passive Lagrangian markers. The authors compared the residence time distribution simulated by RANS, URANS and LES with experimental work, proving that the LES models have a better capability of predicting the energy consumption of mixing than two RANS models. Moreover, their results expose that the treatment of solid particles lacks the coupling and interaction with the local flow field, particular in the near-wall region where the solid particles leave the ditch. Furthermore, D. Dapele et al. [41] studied the mixing of sludge in aeration tank using a point-

particle Eulerian-Lagrangian algorithm based on RANS (PPL-RANS) model. This work assumes that there are no biochemical reactions during aeration, and while air bubbles are modelled as Lagrangians, sludge is described in the Eulerian framework, incorporating rheology into the definition of the liquid's stress rate. The predicted liquid velocity shows an under-prediction near by the core of buoyant plume and are slightly affected by the mesh size.

Despite the wide application of numerical models to forecast the hydrodynamics and bio-kinetics within ASP, they still face important challenges and shortcomings: the steady-state assumption embedded in RANS models struggles to solve the mass transfer between different phase (i.e. from gas phase to liquid phase); the treatment of sludge is mostly described by concentration field and limited to track the dynamics of sludge and its interaction with the surround fluid (i.e. the turbulence scales induced by sludge and its reaction to the solid wall). In this paper, an in-house PP Eulerian-Lagrangian LES-based solver originally developed by [60] is used to simulate solid-liquid-gas three-phase flow encountered in activated sludge process (ASP). The solver's accuracy for predicting gas-liquid flows has been successfully validated in the past regarding the liquid matrix velocity field, second-order statistics, plume integral properties and buoyancy-induced mixing [60, 59, 30]. The capacity of the solver to forecast particle-laden flows has been validated for the propagation of particle-driven gravity currents, showing a good agreement with the front speed of the current and settlement rate. This work will further extend this model by solving simultaneously the gas-liquid-solid flow present in ASP, incorporating four-way coupling and bio-kinetics model for the oxygen transfer and consumption. The validated model is applied to display a pioneering sludge-bubble-wastewater three-phase flow simulation in environmental engineering, where sludge is firstly expressed by solid particles to mimic its roving within wastewater aerated by air bubbles. And sludge rheology is concurrently examined by relating particles concentration to the viscos-

ity of fluid. Moreover, the model investigates how different setups of the air supply system (solitary diffusers with different spacings) and the impact of selected parameters on the concentration of dissolved oxygen in real case of wastewater treatment plants.

5.2 Experimental Validation of Oxygen Transfer in a Bubble Reactor

The ability of this model to predict oxygen transfer is tested against the experimental measurements performed by [108]. The experiments were carried out in a 0.39 m diameter cylindrical pilot-scale column. The height of liquid is set to 1 m at the beginning of each experiment. The aerators were built on a bubble column reactor and symmetrically drilled with holes of 0.5 mm diameter, forming a 'tree' type which is shown in Fig.5.1. The sparger is located 0.135 m above the bottom of the reactor and has a 2.2% free area that is not covered by the diffusers. The oxygen transfer rate is experimentally measured by adding sodium sulphite in the water and calculating the changes on sulphite concentration over time. More experimental details can be found in [108].

In order to validate the accuracy of the solver on predicting oxygen transfer, numerical simulations are carried out on an analogous setup to the experiment and its details are shown in Table. 5.1. The boundary conditions for the dispersed phase are the prescription of gas velocities ranging between 0.14 and 0.28 m/s. A constant bubble size of $D_P = 5.0\ mm$ was imposed since this was the average bubble diameter of measured in the experiments. A reasonable grid size in Eulerian framework is chosen as 10 mm based on bubble size and Milelli's recommendations. And time step is adopted as 0.001 s. Bubbles are released from the location of the aerator's

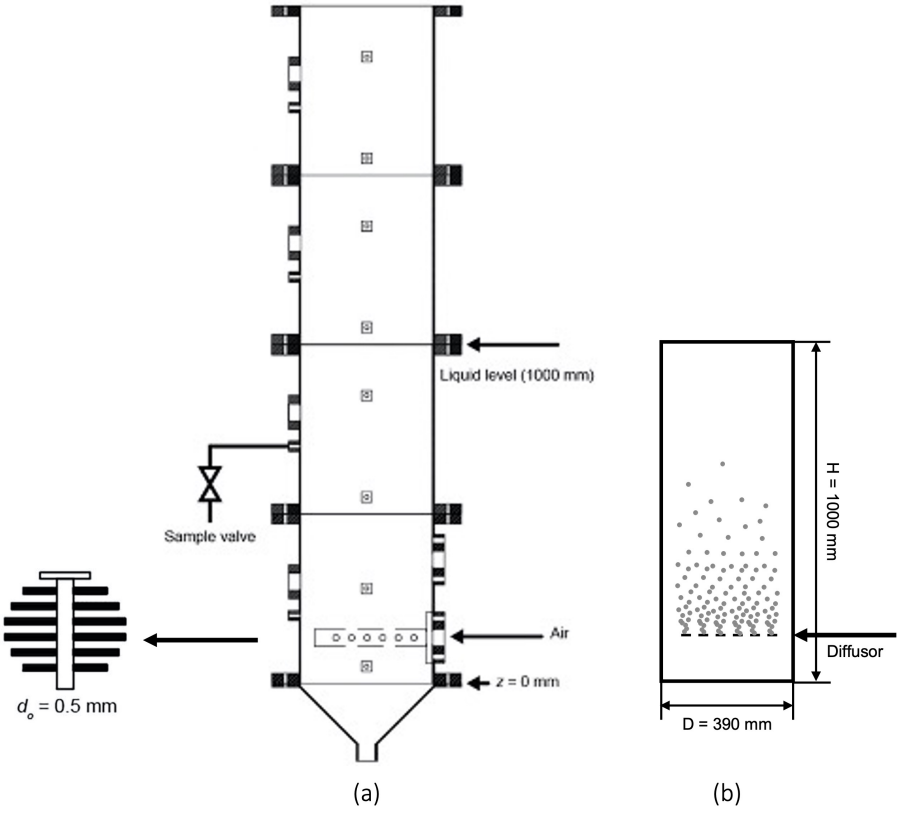

Figure 5.1: Schematic diagram of bubble column: (a) Experimental layout [108]; (b) Numerical setup.

Parameters	Value	Unit
Bubble size	5.0	mm
Diameter of column	0.39	m
Height of column	1.0	m
Water level	1.0	m
Oxygen content in bubble	21	%
Henry constant for oxygen	0.032	-
Mass transfer coefficient for oxygen	0.0004	m/s
Superficial velocity	0.14 to 0.28	m/s
Density of liquid	1040	kg/m^3
Density of air	1.4	kg/m^3
Mesh size	10	mm
Time step	0.001	s

Table 5.1: Numerical setups for validation case

holes and they are removed from the computational domain once they reach the water surface. Boundary conditions for the continuous phase include the use of the no-slip boundary condition at all solid walls and the bottom of the tank and a rigid lid at the water surface with a free slip condition. The initial DO level in the reactor is zero, and the only source are the air bubbles. The PPL algorithm allows tracking the oxygen concentration at each individual bubble and the quantity that is transferred to the water in the cylinder. The DO concentration field across the reactor can be integrated to provide the total Oxygen that has been transferred to the liquid.

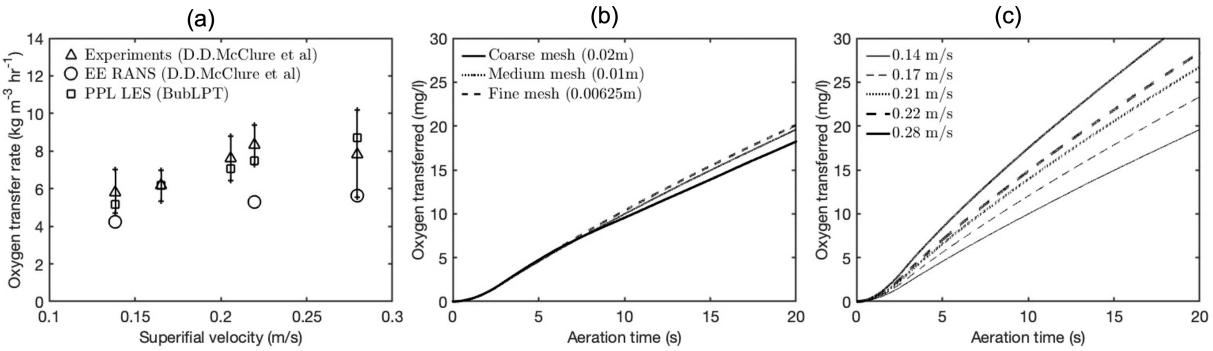

Figure 5.2: Oxygen transfer rate for numerical and experimental data [108]: (a) Experimental validation; (b) Mesh sensitivity analysis; (c) Sensitivity to superficial velocity.

Fig. 5.2 presents the numerical predictions for oxygen transfer rate in bubble column. Fig. 5.2a shows the comparison with experimental results, where triangles represent the oxygen transfer rate measured in the experiments, including a $\pm 20\%$ error range reported by the authors, circles correspond to EE-RANS by [108] and rectangles are our PPL-LES. Our numerical predictions always fall withing the experimental range, and show a consistent agreement throughout the whole parameter range. Fig. 5.2b reveals the time evolution of the oxygen concentration transferred with 0.14 m/s superficial velocity for three grid resolutions, which are 6.25mm, 10mm, 20mm. The results show a remarkable degree of convergence between the medium and finer meshes when it comes to oxygen transfer between gas and liquid. Finally, Fig. 5.2c, shows again the amount of DO transferred versus time. The

Oxygen transfer rate can be obtained from the ratio of final transferred oxygen concentration to aeration time, hence the mean slope of these curves.

5.3 ASP Simulation under Operation Conditions

The previously described LES-based ASP model is tested in a series of three-phase flow simulations to explore ASP in conditions that mimic the setup of an aeration basin in a real-life wastewater facility in the UK.

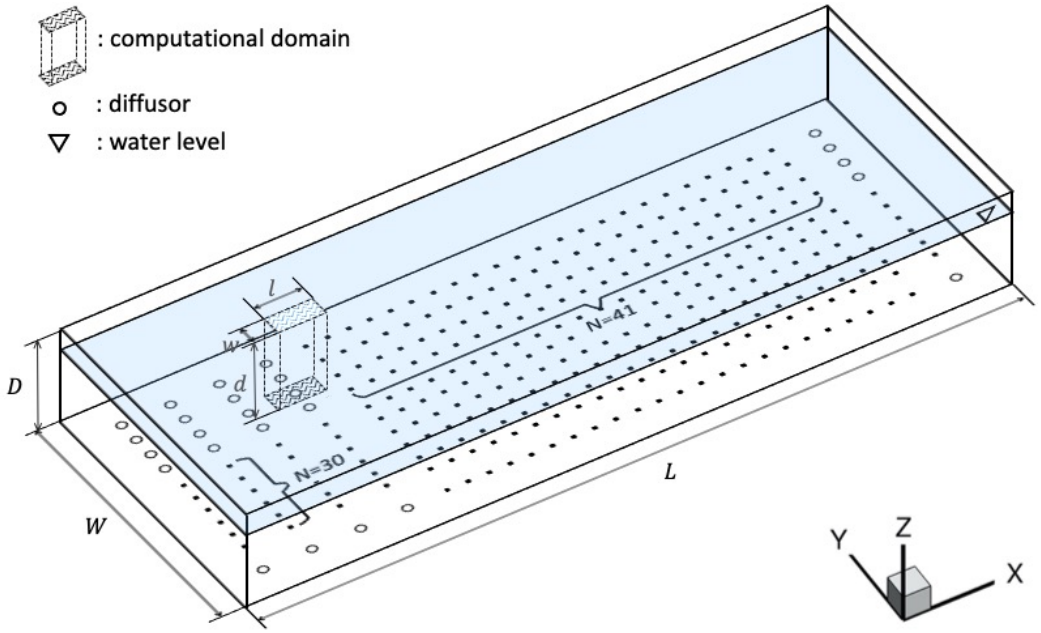

Figure 5.3: Schematic diagram of an ASP basin: L, length of actual tank; W, width of actual tank; D, depth of actual tank; l, length of numerical domain; w, width of numerical domain; d, depth of numerical domain, N, total number of diffusers in horizontal or vertical direction of the tank.

Fig. 5.3 shows our computational domain in the context of a real-size aeration basin for ASP in a wastewater treatment plant. The width/length ratio, depth and air blower distribution and spacing replicate a real basin in a wastewater treatment plant in Wales during normal operation. The tank's depth is 5 m and the average water level is 4m. The diffusers have a diameter of 0.2 m and are located 0.3 m

above the bottom of the tank. Regarding our LES, the computational domain seeks to replicate the surrounding of a single diffuser of such characteristics in a periodic setup. The water depth is 4 m, with 1 m length and 0.5 m width, which corresponds to the distance between diffusers in the real aeration basin. The numerical setup is summarised in Table 5.2. Bubble size is modelled as 5 mm that is the same as validation case. Sludge concentration is chosen as 3400 mg/l falling within the reported range of real sludge in ASP facilities in the UK (3,300 to 4,500). The air gas flow rate was set up to replicate the diffuser's proportional part with respect to the total air conveyed into a real tank (approx. 180,000 l/min). All the lateral boundaries are periodic both for the Eulerian and Lagrangian phases. The solid particles collide with the bottom of tank, where solid particles can settle and accumulate. The top boundary is modelled as water surface in which bubbles are removed from the computational domain once surpassed.

	Computational Domain
Sludge amount	$2e^5$
Sludge concentration (mg/l)	3400
Sludge density (kg/m^3)	1015
Sludge size (mm)	4
Gas flow rate (l/min)	40
Air bubble size (mm)	5.0
Release frequency (bubble/s)	$1e^4$
Side boundaries for CP	Periodic
Free surface boundary for CP	Free-slip
Bottom boundary for CP	No-slip
Side boundaries for DP	Periodic
Free surface oundary for DP	Outlet
Bottom boundary for DP	Wall
Mesh size (mm)	10
Time step (s)	0.001

Table 5.2: Simulation parameters for the base case of the ASP model, based on a real wastewater treatment facility; CP, continuous phase; DP, dispersed phase.

As shown in Fig. 5.4, the sludge composed by discrete 5 mm sized solid particles is initially accumulated at the bottom 25% of the depth of the tank. Fig. 5.4a shows

this initial sludge distribution packed at the bottom of the tank with an incipient burst of particles entrained by the bubble plume (Fig. 5.4b). Two aerator setups are modelled for air injection: a singe plume and a bubble screen consisting of 5 diffusers equally spaced (Fig. 5.4c). These setups were chosen based on preliminary results on optimal mixing induced by buoyant plumes [30]. The blowers in both designs are located along the central spanwise plane. These configurations are tested for the same total constant gas flow rate (i.e., same number of bubbles per unit of time) to test the ASP's performance.

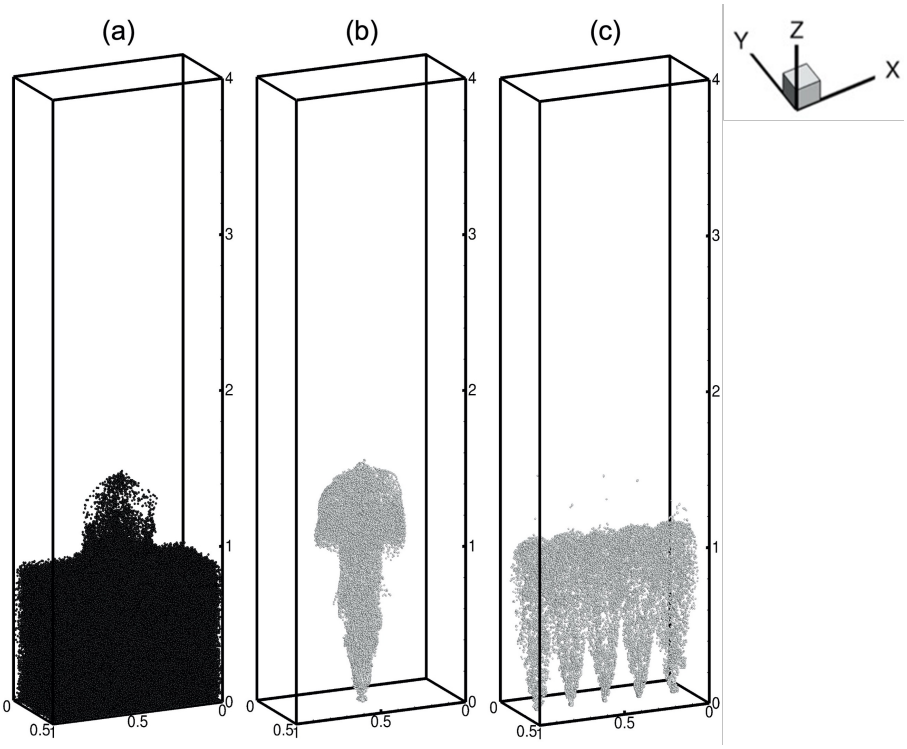

Figure 5.4: Early steps of the ASP LES at the simulation time 0.5: (a) Initial sludge distribution at the bottom for the single-plume case; (b) single plume; (c) bubble screen with 5 sources.

Fig. 5.5 offers a qualitative insight on how the dissolved oxygen (DO) is transferred from air bubbles to water. The results show the contours of DO concentration (a and c) at the central spanwise plane and the overlapped air bubbles colour-coded by their Oxygen fraction (b and d). The initial O_2 level in the bubbles is 23 %, and decreases as they rise due to the transfer to the liquid (Fig. 5.5b and Fig. 5.5d). For

a single plume, the first bubble swarm rising up has to overcome the water's inertia in order to establish the plume. This results in the characteristic mushroom-shaped bubble tip that is observed in Fig. 5.5b. The bubbles in the tip of the plume and, particularly, those that got trapped in the lateral recirculation, have transferred a significant amount of Oxygen (2-3%). In contrast, the bubbles rising in the center of the established plume rise faster and have less exposure to the liquid. For the bubble screen, since each individual diffuser has 20% the flow rate of the single plume, the plumes' centerline velocities are lower and the bubbles rise more slowly and homogeneously. The higher residence time and more homogeneous mixing [30] make the O_2 transfer to the liquid with the bubble screen is more gradual and, overall, more effective than for the single plume case. Similar observations can be made in the instantaneous DO concentrations depicted in Figs. 5.5a and c. The plumes forming the bubble screen loose their individual structure and form an unified swarm from Z=1.4 m on.

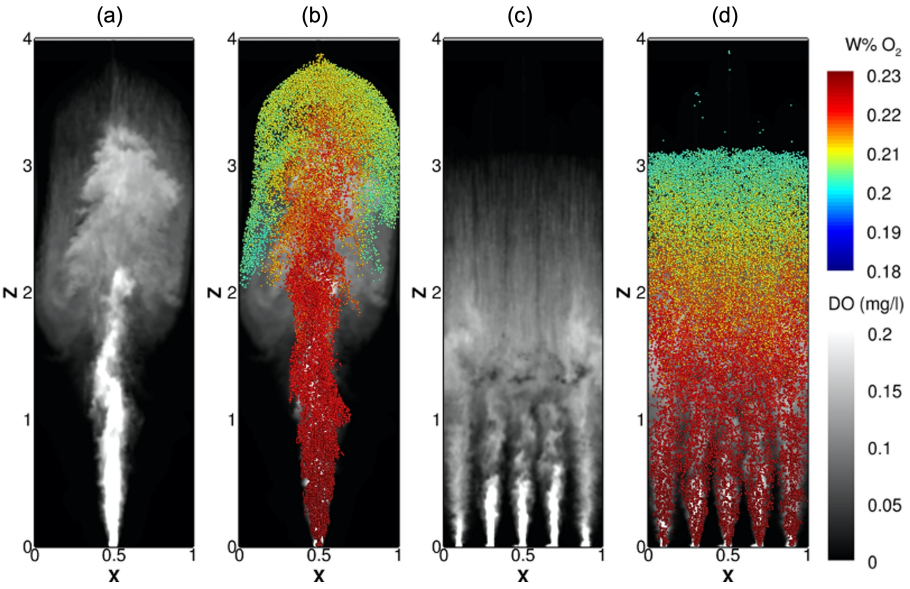

Figure 5.5: Instantaneous snapshots of (a) DO concentration for a single plume; (b) O_2 mass fraction in air bubbles for a single plume; (c) DO concentration for a bubble screen; (d) O_2 mass fraction in air bubbles for a bubble screen at early stages of the aeration.

The solid fraction is missing from Fig. 5.5, since this is concerned with the DO

sources. Fig. 5.6 shows the interaction of both gas (black) and solid (red) dispersed phases in the tank for a single plume and a bubble screen at the same air flow rate. This is illustrated through two instantaneous snapshots at the simulation time 7.5 (Figs. 5.5a) and 20s (Figs. 5.5b). In Fig. 5.6a, the bubble swarm triggers liquid entrainment which drives sludge particles. Only particles located at the core of the plume are driven by the single plume, while the uptake by the bubble screen is rather homogeneous. At 20 s (Fig. 5.6), the sludge particles have been almost completely advected around the tank in both setups. The single plume still exhibits a layer of sludge by the bed and some accumulation in the corners; it is also very clearly illustrated how some of these particles are advected towards the plume's release point. The bubble screen case seems to show less accumulation at the bottom. In both cases, the inertial particles seem to follow the turbulent structures created by the plumes, which are larger for the solitary one.

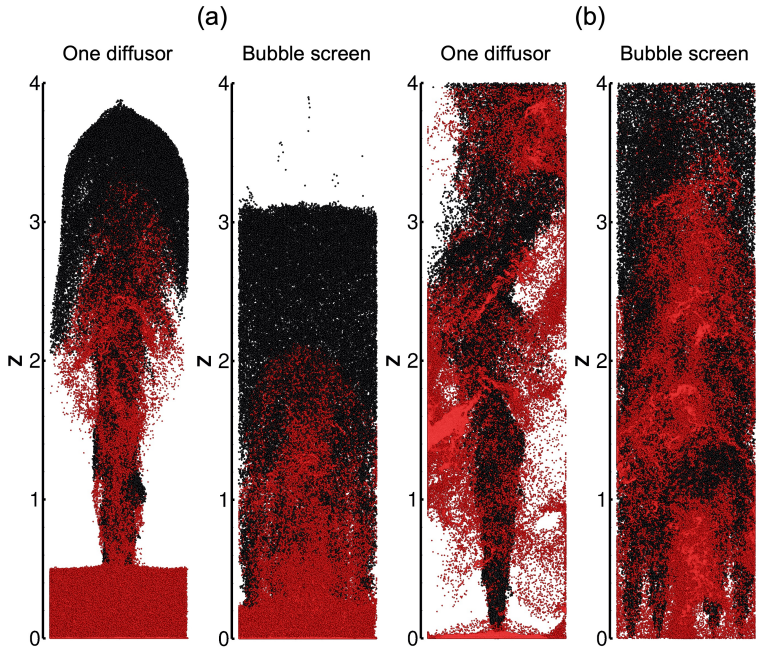

Figure 5.6: Instantaneous Lagrangian fields of sludge particles (red) and air bubbles (black) for a single plume and a bubble screen at (a) 7.5s and (b) 20s into the simulation.

Fig. 5.7 represents the DO concentration and sludge volume fraction against the tank's depth at three different simulation times. The initial DO level is zero.

Fig. 5.7a depicts a comparison between DO levels for clean water (no sludge) and wastewater, in which sludge is consuming Oxygen during its activation. And the maximum DO concentration is found in the area close to the top of the tank, indicating that the oxygen contained in the air can be dissolved into the water from the free surface. At the beginning of aeration, DO is only distributed near by the bottom of the tank, which is gradually produced and mixed by buoyant plume with aeration time, reaching a relatively higher level. In Fig. 5.7b, most of the sludge accumulates at the bottom of the tank in earlier stages of aeration with the higher density than liquid. This figure proves that the aeration is rather effective mixing the sludge particles across the vertical axis. The mixing is not completely homogeneous - the sludge concentration decreases with height due to the plume's buoyancy declining as the bubbles rise up and expand. Interestingly, however, the maximum sludge concentration after the very early stages of aeration is not at the bottom but around 0.75 m after 40 s.

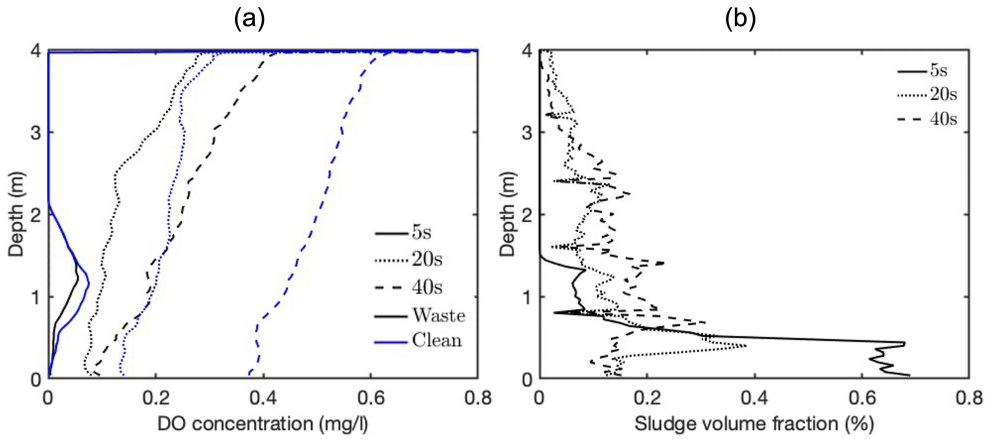

Figure 5.7: DO and sludge volume fraction vertical profiles at three different simulation times (5, 20 and 40s). Black lines: wastewater; blue lines: clean water.

Fig. 5.8 presents the evolution in time of the DO concentration recorded at different locations of the tank, which are compared with the time series in entire tank. The five probes are allocated at the central point of xy plane and their depths are chosen as 0.32 m, 1.12 m, 1.92 m, 2.72 m and 3.52 m. In general, the line for

each probe raises with aeration time and fluctuates among the line referring to the whole tank (thick black line). The DO concentration at the bottom (thin black line) is almost 0 from 0s to 20s since all sludge gathering in the release area consumes the most of DO generated by aeration. With the sludge being pushed upward by buoyant plume, required DO for sludge is smaller than the amount produced by aeration, leading to an increase on DO concentration from 20s to 50s. Comparing to the rest four lines, it can be seen that the line closer to the top experiences a later moment when DO concentration starts increasing since generated DO requires a buoyant plume to be pushed from the bottom to the top. The results offer a possibility of estimating DO level for entire tank in real case based on the recording of probes allocated in the tank.

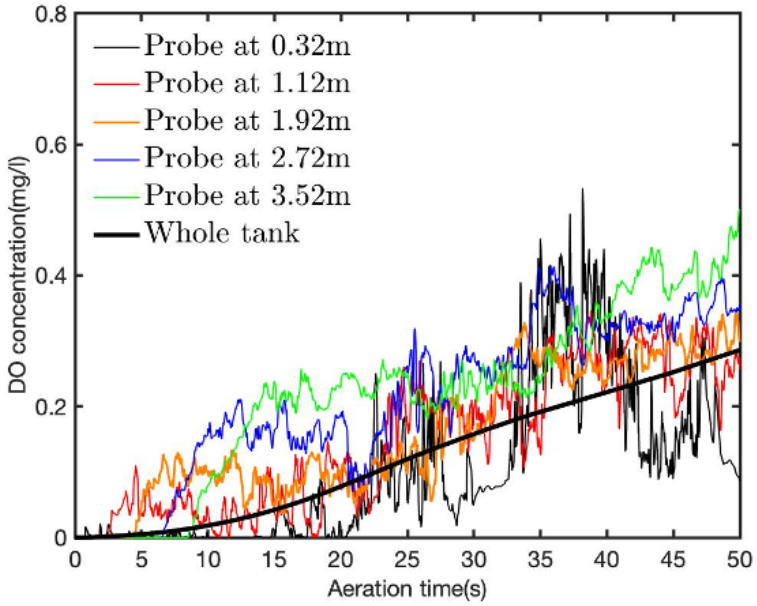

Figure 5.8: Time series of DO concentration at different heights: thinner black line, $z = 0.32m$; red line, $z = 1.12m$; orange line, $z = 1.92m$; blue line, $z = 2.72m$; green line, $z = 3.52m$; thicker black line, whole tank.

5.3.1 Sensitivity analysis of the ASP model

Our LES-based ASP model is used to analyse the impact of several physical parameters on sludge activation. A base scenario is defined in this section for the following discussion, where bubble and sludge size are modelled as 5 mm and 4.5 mm respectively, and the tank shown in Figure.5.3 is aerated by bubble screen with 40 l/min under 1.2 mg/l initial DO level. And the base case is analysed at the simulation time 8s when the bubble plumes reach the top of the tank. Such selected parameters and the values that were tested are specified in Table 5.3: average sludge particle size, average bubble size, air flow rate and initial DO levels. Sludge is tested for three different sizes, 4 mm, 4.5 mm and 5.5 mm, under a total constant sludge concentration 3400 mg/l. The air flow rate constitutes, together with the aeration time, the main operational decision for ASP operators. Three different gas flow rates are examined under a constant bubble size 5 mm to test its impact on sludge activation. Initial DO levels are known to be relevant to ASP's performance, and this is mostly determined by the atmospheric conditions. In very simplified terms, in 'dry' weather there is no oxygen dissolved in the water prior to aeration, since this has been all consumed by the sludge in the tank. However, rainfall ('wet' weather) promotes aeration at the tank's surface and inputs of well oxygenated surface runoff water [98]. Henceforth 'dry' designates zero DO levels in the tank prior to aeration and 'wet' an uniform and homogeneous initial distribution of DO_0=1.2 mg/l, unless stated otherwise. Four different initial DO levels are considered: 0 (dry), 0.6, 1.2 (wet) and 2.4 mg/l. The impact of bubble size on oxygen transfer is also analysed by examining the effect of three different average sizes using monodispersed distributions of 4 mm, 5 mm and 6 mm diameters.

Fig. 5.9 reveals the influence of weather conditions/initial DO levels on sludge activation for the base case. The sludge particle size in the figure is a function

Selected parameters	Value	Unit
Sludge floc (particles) size	4.0, 4.5, 5.5	mm
Bubble size	4.0, 5.0, 6.0	mm
Air flow rate	30.0, 40.0, 50.0	l/min
Initial DO/weather	0.0 0.6, 1.2, 2.4	mg/l

Table 5.3: Parameter range tested with the ASP LES model.

of Oxygen consumption: larger particles have absorbed a larger O_2 content. Wet weather is simulated with an initial uniform DO level of 1.2 mg/l in the tank while for dry weather there is no DO in the tank prior to bubble release. The average particle size is bigger for wet weather. This is particularly notable at the tank's bottom, where the system struggles to bring DO when the initial levels are low.

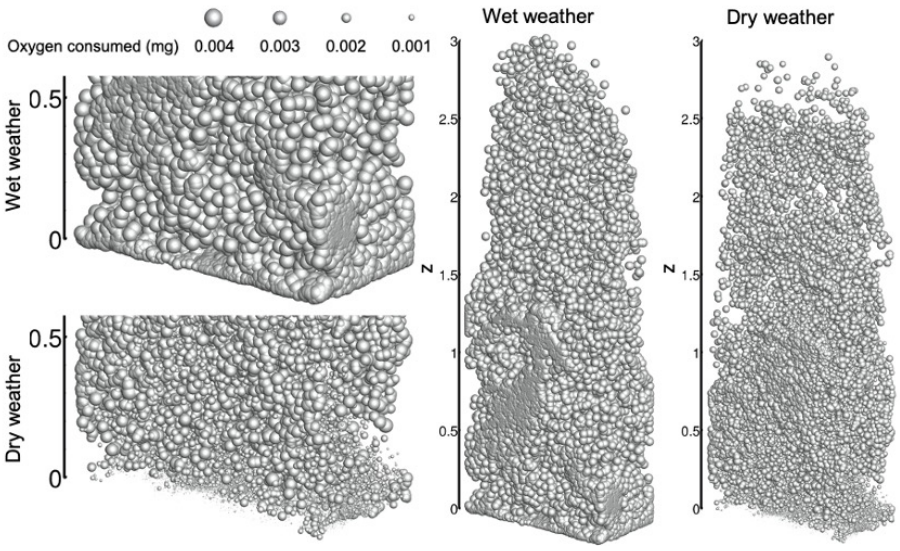

Figure 5.9: Oxygen content of sludge particles at the simulation time 8s in a bubble screen for wet weather (1.2 mg/l initial DO) and dry weather (0 mg/l initial DO).

The liquid phase, solved within the Eulerian framework, acts as the interceder between the dispersed air bubbles and the solid sludge flocs in the Oxygen transfer process. Fig. 5.10 shows isosurfaces of DO concentration at two different heights, Z/H = 0.125 (left) and Z/H = 0.625 (right), for the base case under wet (initial DO level DO_0 =1.2 mg/l) and dry (initial DO level DO_0 =0) conditions. The isosurfaces are colour-coded by the sludge volume fraction. The results demonstrate

that initial DO levels are still critical after a long exposure to aeration. The left part of the figure corresponds to a location close to the bottom of the tank; the differences between 'dry' and 'wet' conditions are remarkable. When DO_0 =0, the input from the bubble screen on the DO levels is revealed by the peaks aligned in the centreline of the computational domain, with the overall DO concentration being around 0.15 mg/l. In comparison, the wet scenario shows an overall slight decrease of the initial DO levels (DO_0 =1.2 mg/l), with higher DO levels at the domain's corners; instead of the peaks observed in the dry case, there are deep cavities aligned with the centreline, that correspond to high concentrations of sludge absorbing the DO. This suggests that the DO levels in the dry case are too low to effectively activate the sludge particles near the bottom (in agreement with 5.9). The picture at z/H =0.625 is rather different, in both cases there is a much more homogeneous mixture. There are still dips in at the centre of the domain for the wet case, although not as profound as near the bottom, revealing that the activation is intense, whereas the low DO levels in the dry case seem to constitute a bottleneck.

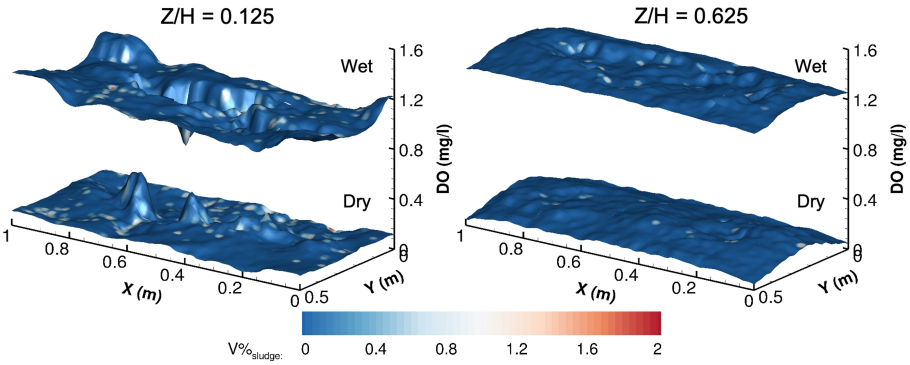

Figure 5.10: Distribution of DO and sludge concentration for different wet (DO_0 =1.2 mg/l) and dry (DO_0 =0 mg/l) conditions: left, slice at Z/H = 0.125; right, slice at Z/H = 0.625.

Fig. 5.11 shows time series of the Oxygen uptake by sludge (a) and Oxygen transfer from bubbles (b) across the entire tank for two different weather conditions and diffuser setups (single plume and screen). The O_2 transfer from bubbles shows the same trends for the examined parameter range. As reasonably expected, more

diffusers and a lower initial DO result in a higher transfer. The analysis of the sludge uptake is more revealing of the mechanisms of activation. The initial DO levels (dry or wet weather) determines the magnitude of sludge activation. Consequently with the previous results, the Oxygen uptake by sludge is almost twice in wet conditions. There is also a different trend between wet and dry simulations at early stages ($t < 20$ s), due to the necessary build up of DO through aeration required under dry conditions to start the activation. The diffuser setup proves to be critical as well. The single plume case show a relaxation on the activation rate after 15 s; this is not observed for the bubble plume case. This can surely be attributed to the more effective mixing [30].

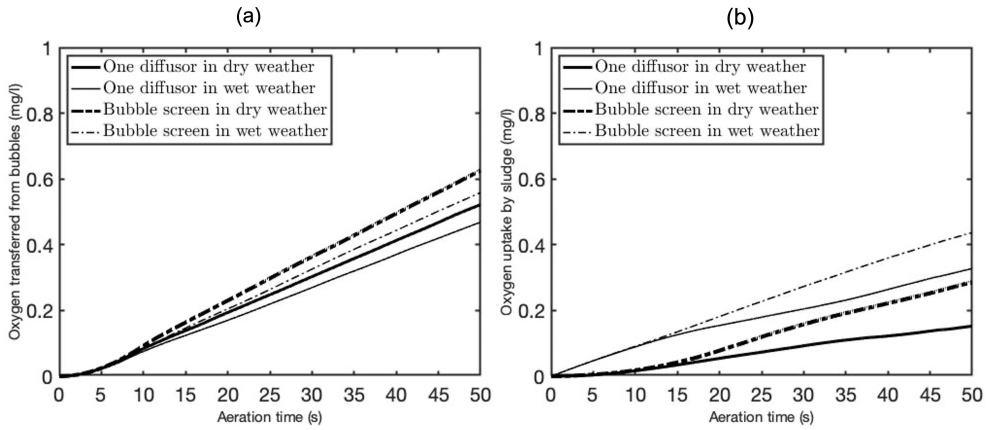

Figure 5.11: Time evolution of oxygen uptake by sludge (a) and time evolution of oxygen transferred from bubbles (b) across the entire volume of the computational domain for a single bubble plume and a bubble screen in wet and dry conditions.

Fig. 5.12 replicates the time evolution analysis of the Oxygen uptake and transfer to examine the effect of sludge size on the activation rates. The bubble screen setup is tested with 4 mm, 4.5 mm and 5.5 mm monodispersed distributions of sludge floc diameters in wet and dry weather. The total solid fraction in the tank was identical in all cases. The overall conclusion is that the sludge particle size has very little effect on these processes, clearly much less relevant than the weather conditions or diffuser setups.

Fig. 5.13 explores further the sensitivity of four different initial DO levels: 0

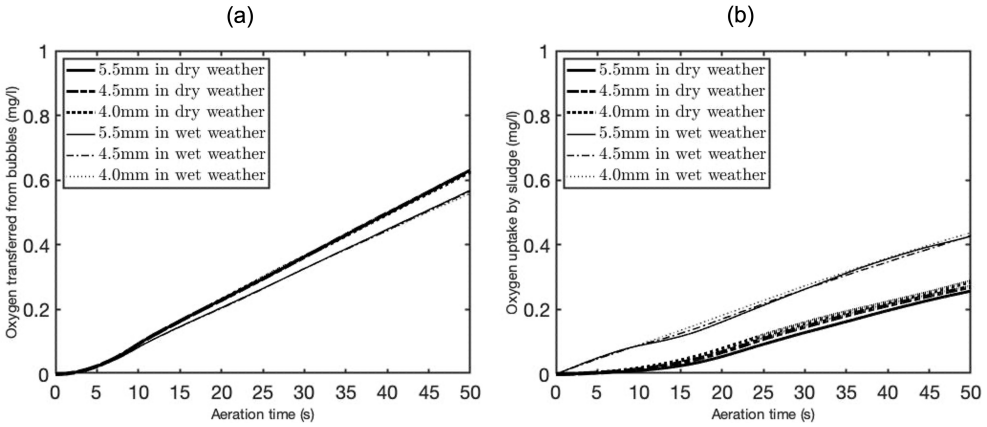

Figure 5.12: Time evolution of oxygen uptake by sludge (a) and time evolution of oxygen transferred from bubbles (b) across the entire volume of the computational domain for three different sludge sizes in wet and dry conditions .

('dry'), 0.6, 1.2 ('wet') and 2.4 mg/l,with and without aeration. The results for aeration cases show that the initial DO level DO_0 has a remarkable influence on the activation rate. However, the impact of DO_0 over the activation is non-linear. While the case with DO_0=0 produces qualitatively worse rates of oxygen uptake by the sludge, the differences between the other three levels are not that remarkable, despite the initial DO levels being increased a 100% between one case and the next. As clearly illustrated by the cases without aeration, the initial DO levels will feed the ASP at early stages (roughly up to 10-15 s in this case), and the aeration takes over from there, hence the flat line for the non-aerated cases. For scenarios with aeration, the lower the initial DO levels, the more impact the transition to having bubbles as the only source of DO will be. Interestingly, this impact seems to be long-lasting.

Fig. 5.14 shows a time series of Oxygen uptake by sludge simulated during 100 s to discuss how operational decisions regarding aeration affect the ASP. In this case, we simulate the effect of stopping the aerators 30 s inside the simulation (represented by the red dashed line). Thick dotted and solid lines represent non-stop aeration for wet and dry weather, respectively. Thin dash and dotted lines designate the alternative strategy which switches aeration off at 30 s for wet and dry, respectively.

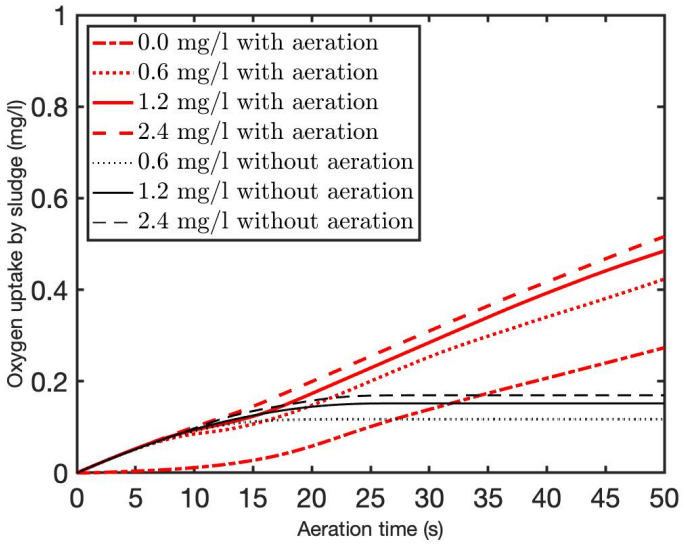

Figure 5.13: Comparison of oxygen uptake by sludge for four different initial dissolved oxygen levels: 0 ('dry'), 0.6, 1.2 ('wet') and 2.4 mg/l. Red thick lines: time evolution with aeration; Black thin lines: time evolution without aeration.

Finally, the thin solid line refers to a case without aeration in wet weather, just for reference (dry weather case was not included since no activation takes place without aeration in that scenario). Comparing to two power strategies, it is noted that the time series line of alternative way continuously follow the line representing full power approach in two weather conditions, which is defined as inertial time in this paper. Comparison of inertial time between wet and dry weather shows that the time in wet weather is approximately 10s that is larger than the time in dry weather (about 2s), exhibiting that wet weather is more applicable for the situation where aerator experiences an unexpected termination in real case.

Fig. 5.15 shows time series of DO concentration recorded by two numerical probes located at 1 and 3.5 m along the central plane of the domain. In wet weather conditions (DO_0=1.2 mg/l), the lower probe reports a DO decline between 5 and 20 s. This corresponds to the time when the sludge particles reach that height and start consuming the available DO. After 20 s, the aerations and activation reach an equilibrium and the DO levels fluctuate around 1.1 mg/l. The upper probe

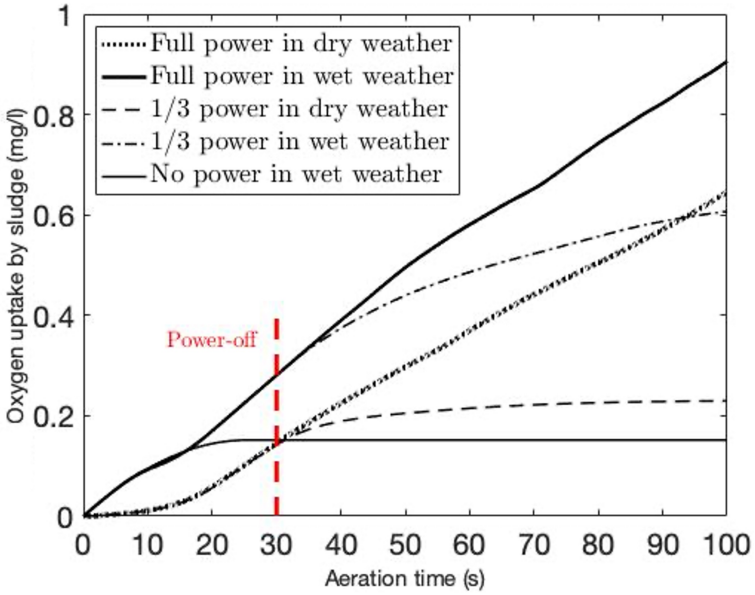

Figure 5.14: Oxygen uptake by sludge with different aeration strategies under two different weather conditions: 1.2 (wet) and 0 mg/l (dry) initial DO. Red line, end of aeration for alternative strategy; dashed line, aerators keep working in dry weather; thick black line, aerators keeping working in wet weather; double dash line, aerators work until power-off in dry weather; dotted line, aerators work until power-off in wet weather, thin black line, aerators do not work in wet weather.

reports a sustained DO increase, due to the lower presence of sludge (see Fig. 5.7) at that height and the inputs from aeration from approx. 10 s onwards. It is worth noting that the proximity to the free surface benefits from the atmospheric input, enhanced by the bubble plume-enhanced mixing. Regarding dry weather, the overall DO concentration is approx. 80% smaller than wet conditions. Within that order of magnitude, the upper probe (3.5 m) exhibits a similar trend to the one reported in the wet case. The lower probe does not measure DO levels increasing until over 20 s have passed either. During that period, the DO peaks thanks to the aeration input are quickly consumed by the sludge. From 20 s onwards, an equilibrium appears to be also found in the dry case, with DO values fluctuating around 0.2 mg/l.

Fig. 5.16 quantitatively compares the integral amount of Oxygen absorbed by activated sludge under a range of conditions after 50 s of activation. Three gas flow rates (30, 40, 50 l/min) and three bubble sizes (4, 5, 6 mm) are examined. The

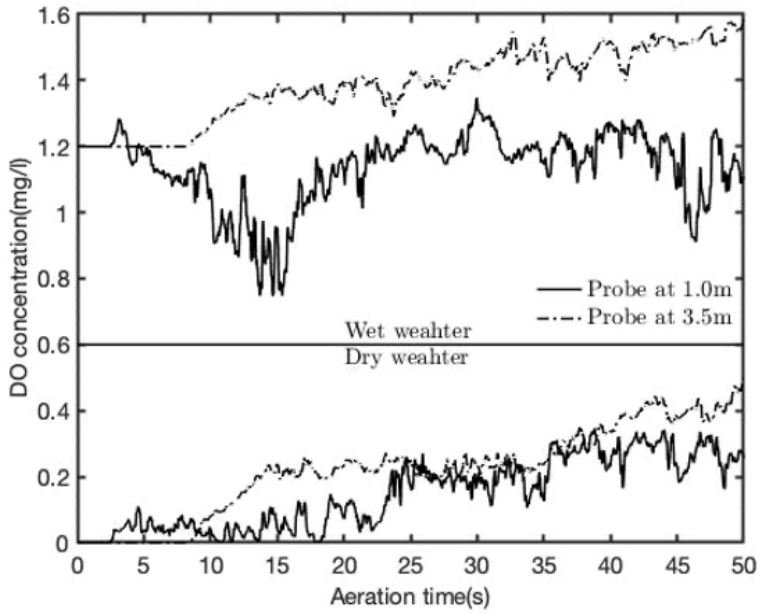

Figure 5.15: Time evolution of DO concentration at two depths with different initial DO levels: 1.2 mg/l (wet) and 0 mg/l (dry). Solid line: $z = 1.0m$; dotted line: $z = 3.5m$.

amount of Oxygen consumed per sludge particle was recorded, and the average μ_{O_2} and standard deviation σ_{O_2} calculated. The ratio μ_{O_2}/σ_{O_2} is used as a quality indicator: a higher value implies higher activation homogeneously distributed throughout the tank, and viceversa. Fig. 5.16a shows a significant gap depending on the initial DO levels, with μ_{O_2}/σ_{O_2} being on average 3 times higher in wet conditions. As expected, higher flow rates lead to higher ratios, and this trend appears to be non-linear. The μ_{O_2}/σ_{O_2} ratio for 50 l/min sees a nearly 40% increase when compared to 40 l/min. Fig. 5.16b shows the ratios for different bubble sizes (always under a constant flow rate), which can be controlled to a degree through the diffusers' design. The differences found are not significant, albeit the 5 mm bubbles provide the best results for the wet case, while 4 mm is better for the dry one, although virtually on pair with 5 mm. A smaller bubble size improves mass transfer by increasing the contact surface between phases, whereas larger bubbles provide wider buoyant plumes [59], promoting a more homogeneous mixing.

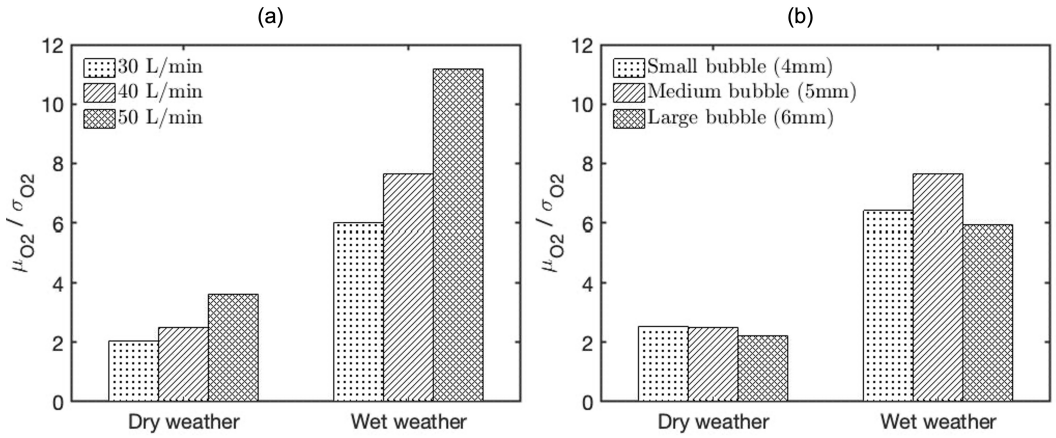

Figure 5.16: Average versus standard deviation for the Oxygen uptake by a individual sludge particles. Results for wet and dry weather conditions (1.2 and 0 mg/l initial DO), 30, 40 and 50 l/min air flow rates (a) and 4, 5 and 6 mm bubble diameters (b).

5.3.2 Comparison with Experimental Data

Fig. 5.17 presents a comparison of Oxygen uptake rate (OUR) between our ASP model numerical predictions (coloured symbols) and recent experimental measurements (circles) provided by [120] for different sludge concentrations. The solid line describes the relation between OUR and sludge concentration (Sc): $OUR = 19.9492 - 0.0018 \times Sc$ discussed in Section. **??**. The base case is examined in this part and compared with single plume set up. The LES-based ASP model is tested bubble screen for a range of initial DO levels and air flow rates. The rate produced by bubble screen perfectly fall within the measurement from the experiment in which the rate is determined by recording the initial and final DO level. These results also reveal that increasing the aeration rate can improve the OUR by 11 %, which is more efficient than increasing the initial DO level with 5 % increment on the OUR.

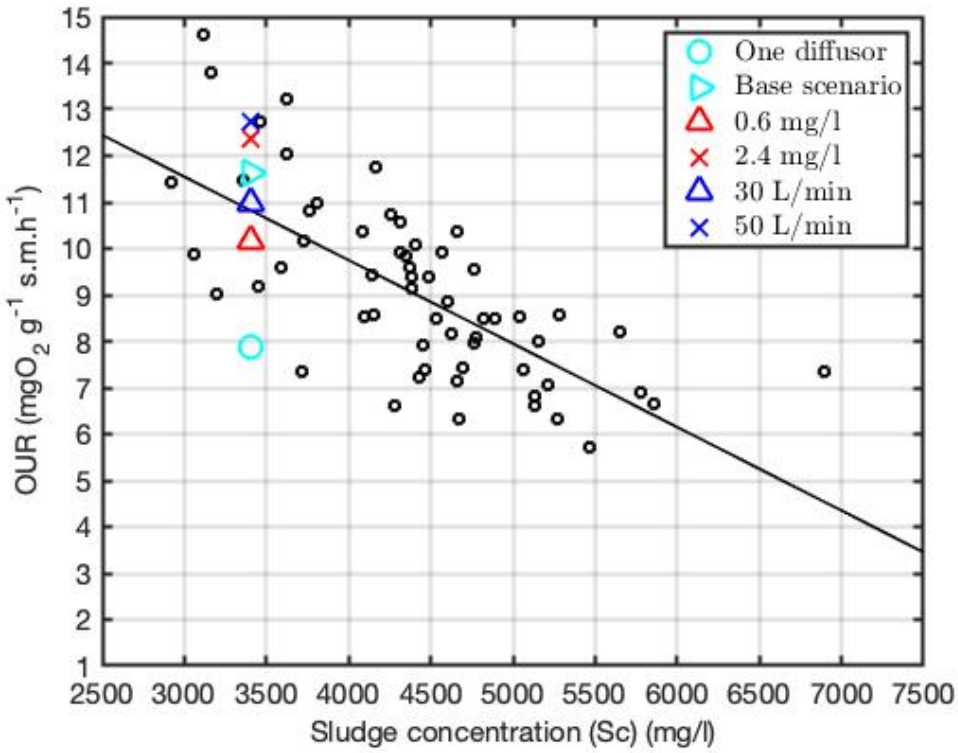

Figure 5.17: Numerical-experimental comparison of sludge's Oxygen uptake rate [120].

5.4 Conclusions

This paper introduced the first three-dimensional LES-based model for sludge activation process (ASP) in wastewater treatment. A point-particle Eulerian-Lagrangian algorithm has been employed to investigate the solid-gas-liquid three-phase flow encountered in ASP. To the authors' knowledge, this work presents the first turbulence-solving ASP simulation, including four-way coupling among the three phases, preserving the discrete nature of bubbles and sludge flocs and tracking the sources and sinks of Dissolved Oxygen (DO) at the particle level. The inertial sludge particles settle naturally and interact between each other following a soft-sphere collision model. Kinetics were implemented to describe Oxygen transfer from air bubbles and uptake by sludge. Once dissolved in the water, Oxygen is transported via advection and diffusion. Sludge affects the viscosity of the surrounding water according to its rheology.

A pilot-scale bubble column was modelled to validate the ability of the solver to predict Oxigen transfer between air bubbles and water versus experimental measurements [108], exhibiting a remarkable agreement at five different superficial velocities. The grid independence of the model is proven by comparing different mesh resolutions. The model was tested establishing a periodic domain with realistic dimensions and boundary conditions for regular aeration basins in wastewater plants. This implied that the order of magnitude of bubbles and sludge particles in the domain was on average 10^4 and 10^5, occurring at the same time. The numerical results provide an insight on the fluid dynamics involved on the interaction between phases, and the key parameters that control the sludge activation process. Two different aerator designs were tested and it was that, while keeping the same air flow rate, more aerators improve the DO mixing and sludge distribution, avoiding the formation of dead anoxic regions by the bottom of the tank. A very sensitive parameter is the initial

DO levels, which mostly depend on weather conditions. Our simulations showed that low DO levels before aeration starts have a long lasting effect. In particular, anoxic conditions (typical in dry weather) act as a bottleneck to the ASP; as initial DO levels increase, the sensitivity decreases as the levels approach saturation (i.e., sludge has all the Oxygen availability it may require). Keeping minimum DO levels when aeration is not active has a more critical impact than increasing the air flow rate of the bubbles or the aeration time. Our results showed also that, under constant flow rate and/or sludge concentration, bubble and sludge average size have not critical impact on the results, since changes on both induce mechanisms that affect the process in contradicting ways.

Acknowledgements

The computational works described in this paper were performed using the University of Birmingham's BlueBEAR HPC service and the Athena at HPC Midlands+ which was funded by the EPSRC. The authors are grateful for the facility and support provided by the University.

Chapter 6

Conclusions and Future Work

In this research, a numerical investigation on turbulent dispersed multiphase flows is carried out to understand the fluid dynamics of multiphase flow systems and apply its content to engineering applications. An extensive literature review has been performed to characterise and describe a wide range of numerical approaches to simulate multiphase flows (two-phase [163, 164, 162, 25, 23]and three-phase [127, 133, 9, 42]flow systems). The critical analysis compares both Eulerian and Lagrangian descriptions of the dispersed phase, highlighting that Lagrangian algorithms have well capable of capturing the different scales of motion induced by the particles (solid particles, bubbles and droplets) [53, 118, 82, 84]. The review also discusses the energy usage in realistic scenarios involved by multiphase flow systems (chemical reactor and wastewater treatment plants) in order to perform an intelligent control of fluid dynamics for saving energy and net zero strategy. Accordingly, the importance of treating the continuous and dispersed phase as well as the interaction between the two has been highlighted in this study. The outcome of this work contributes to an accurate, yet rapid, computational methodology to provide reliable simulation of multiphase flows in real scenarios.

An in-house point-particle Eulerian-Lagrangian LES solver is further developed and provides a predictive tool to optimise aeration systems, save energy and improve water quality in environments and ultimately, people's lives. A transient, three-dimensional, finite difference method is adopted in the solver to simulate viscous, incompressible flows on structured grids. The developed flow solver has been validated by previous research in terms of the hydrodynamics of the bubble plume [60, 59, 126, 30]. Thus, this work initially further validates the solver's ability to predict mixing time in a bubble reactor with various types of aerators, exhibiting a close agreement with the experimental measurements. The validated numerical framework is applied to reduce the energy consumption of aeration systems and determine the optimal design for the systems in chemical and environmental engineering. Considering the influence of inertial particles on multiphase flow system, the study moves to the next stage with a focus on implementing the algorithm of computing particle-to-particle interaction in the solver and validate its accuracy by the laboratory data [1]. The resulting code solver contributes to a four-way coupling approach to simulate particle-laden flows, which can be further applied in evaluating sedimentation transport in river engineering. The main focus is the description of the mechanisms of propagation of particle-driven or turbidity currents, for which a point-particle Eulerian-Lagrangian algorithm is developed, introducing a soft-sphere collision model. In order to optimise the energy usage in activated sludge process in wastewater treatment plants, the work integrates the first two implementations in the solver and takes account into the mass transfer among the different phases, which is validated by the experimental measurement carried out in a pilot-scale bubble column. The integrated framework adopts the particles with different densities to represent the sludge and air bubbles in wastewater, where the oxygen contained in each phase is transported based on the content gradient. The results discuss the optimal aeration strategy for facilitating the activation of sludge in wastewater and analyse its sensitivity to different weather condition. Based on the the afore-

mentioned three parts, several main conclusions are reached by the validated code solver in terms of understanding the fluid mechanisms (turbulent mixing by buoyant plume, particle-laden flows and three-phase flows) and engineering applications (bubble reactors and wastewater treatment plants),

- Bubble screens are able to provide superior mixing efficiency for a given gas flow rate than the individual plume, which is found to save at least 20% of energy for aeration systems [30].

- Implementing a bubble screen-based layout is more effective with regarding energy consumption than increasing the gas flow rate.

- Turbidity currents are significantly slower than gravity currents, they are less persistent and develop increased multi-scale and asymmetric loft-and-cleft structures.

- Fast removal of the gate has a critical effect in increasing the kinetic energy at the beginning of the simulation and triggering water intrusion in the lock region. This influence is mostly relevant in the early stages of development of the current, albeit non-negligible long-term effects on the agitation were observed along its propagation.

- For activated sludge process, air bubbles not only provide a source of oxygen, but also trigger turbulent mixing that is extremely effective redistributing sludge within the domain.

- The initial dissolved oxygen levels in the tank controls the activation's rate, whereas the diffuser distribution rules its evolution in time.

- Low dissolved oxygen levels before aeration starts have a long lasting effect, acting as a limiting factor for activated sludge process.

- High dissolved oxygen levels increase by at least 100% the overall activated sludge process performance when compared to anoxic conditions.

The following ongoing works can be implemented for further investigation,

- The proposed four-way coupling approach should be further applied and evaluated in different realistic scenarios associated with particle-laden flows (i.e., sludge transport in a baffled tank, aerosols transmission in a ventilated room and micro-plastic transport in wastewater [113]).

- The efficiency of computing particle-to-particle interaction should be examined and optimised when dealing with a large number of particles (i.e., distributing the particles only by MPI blocks and performing hybrid MPI-OpenMP parallelisation [123, 23]).

- It might be interesting to reproduce more physical properties of the bubble plume in the solver (i.e., thermal buoyant plume that potentially enhances the performance of aeration system in wastewater treatment plants under extreme cold weather conditions [53]).

- Rheology modelling of particles (sludge) should be further developed and investigated with a focus on the influence of sludge on the viscosity of non-newtonian fluids [32].

- A data-driven model (Artificial intelligence surrogate models) can be developed and incorporated with the proposed multiphase code solver in order to account for particle-induced turbulence (which is currently a challenge in resolving particle-laden flows [12, 165]).

- The database associated with activated sludge process in this study should be incorporated with artificial intelligence in order to formulate a predictive tool for practical engineering design (i.e., uncertainty qualification for aeration system and optimisation of placing sensor for real measurement).

- The ongoing research can benefit from the experimental data in real case of wastewater treatment plants and perform data assimilation to minimise the difference between numerical and experimental measurements [158].

Bibliography

[1] C. Adduce, G. Sciortino, and S. Proietti. Gravity currents produced by lock exchanges: experiments and simulations with a two-layer shallow-water model with entrainment. *Journal of Hydraulic Engineering*, 138(2):111–121, 2012.

[2] M. F. Ali, J. Gan, X. Chen, G. Yu, Y. Zhang, M. Ellahi, and A. A. Abdeltawab. Hydrodynamic modeling of ionic liquids and conventional amine solvents in bubble column. *Chemical Engineering Research and Design*, 129:356–375, 2018.

[3] E. Alméras, C. Plais, F. Euzenat, F. Risso, V. Roig, and F. Augier. Scalar mixing in bubbly flows: Experimental investigation and diffusivity modelling. *Chemical Engineering Science*, 140:114–122, 2016.

[4] E. Alméras, C. Plais, V. Roig, F. Risso, and F. Augier. Mixing mechanisms in a low-sheared inhomogeneous bubble column. *Chemical Engineering Science*, 186:52–61, 2018.

[5] E. Alméras, F. Risso, V. Roig, S. Cazin, C. Plais, and F. Augier. Mixing by bubble-induced turbulence. *Journal of Fluid Mechanics*, 776:458–474, 2015.

[6] S. An, P. Y. Julien, and S. K. Venayagamoorthy. Numerical simulation of particle-driven gravity currents. *Environmental fluid mechanics*, 12(6):495–513, 2012.

[7] J. D. Anderson and J. Wendt. *Computational fluid dynamics*, volume 206. Springer, 1995.

[8] B. Andersson, R. Andersson, L. Håkansson, M. Mortensen, R. Sudiyo, and B. Van Wachem. *Computational fluid dynamics for engineers*. Cambridge University Press, 2011.

[9] H. Azargoshasb, S. Mousavi, T. Amani, A. Jafari, and M. Nosrati. Three-phase CFD simulation coupled with population balance equations of anaerobic syntrophic acidogenesis and methanogenesis reactions in a continuous stirred bioreactor. *Journal of Industrial and Engineering Chemistry*, 27:207–217, 2015.

[10] M. C. Baker, B. Kong, J. Capecelatro, O. Desjardins, and R. O. Fox. Direct comparison of Eulerian–Eulerian and Eulerian–Lagrangian simulations for particle-laden vertical channel flow. *AIChE Journal*, 66(7):e16230, 2020.

[11] S. Balachandar and J. K. Eaton. Turbulent dispersed multiphase flow. *Annual review of fluid mechanics*, 42:111–133, 2010.

[12] S. Balachandar, W. Moore, G. Akiki, and K. Liu. Toward particle-resolved accuracy in Euler–Lagrange simulations of multiphase flow using machine learning and pairwise interaction extended point-particle (PIEP) approximation. *Theoretical and Computational Fluid Dynamics*, 34(4):401–428, 2020.

[13] J. B. Bell, P. Colella, and H. M. Glaz. A second-order projection method for the incompressible Navier-Stokes equations. *Journal of computational physics*, 85(2):257–283, 1989.

[14] M. Bini and W. Jones. Large-eddy simulation of particle-laden turbulent flows.

[15] R. T. Bonnecaze, H. E. Huppert, and J. R. Lister. Particle-driven gravity currents. *Journal of Fluid Mechanics*, 250:339–369, 1993.

[16] M. C. Boufadel, S. Socolofsky, J. Katz, D. Yang, C. Daskiran, and W. Dewar. A review on multiphase underwater jets and plumes: Droplets, hydrodynamics, and chemistry. *Reviews of Geophysics*, 58(3):e2020RG000703, 2020.

[17] J. Bridgeman. Computational fluid dynamics modelling of sewage sludge mixing in an anaerobic digester. *Advances in Engineering Software*, 44(1):54–62, 2012.

[18] W. L. Briggs, V. E. Henson, and S. F. McCormick. *A multigrid tutorial*. SIAM, 2000.

[19] C. Brouckaert and C. Buckley. The use of computational fluid dynamics for improving the design and operation of water and wastewater treatment plants. *Water Science and Technology*, 40(4-5):81–89, 1999.

[20] V. V. Buwa, D. S. Deo, and V. V. Ranade. Eulerian–Lagrangian simulations of unsteady gas–liquid flows in bubble columns. *International journal of multiphase flow*, 32(7):864–885, 2006.

[21] V. V. Buwa and V. V. Ranade. Mixing in bubble column reactors: role of unsteady flow structures. *The Canadian Journal of Chemical Engineering*, 81(3-4):402–411, 2003.

[22] M. I. Cantero, S. Balachandar, and M. H. Garcia. An Eulerian–Eulerian model for gravity currents driven by inertial particles. *International Journal of Multiphase Flow*, 34(5):484–501, 2008.

[23] J. Capecelatro and O. Desjardins. An Euler–Lagrange strategy for simulating particle-laden flows. *Journal of Computational Physics*, 238:1–31, 2013.

[24] J. Capecelatro and O. Desjardins. Eulerian–Lagrangian modeling of turbulent liquid–solid slurries in horizontal pipes. *International journal of multiphase flow*, 55:64–79, 2013.

[25] J. Capecelatro, O. Desjardins, and R. O. Fox. Numerical study of collisional particle dynamics in cluster-induced turbulence. *Journal of Fluid Mechanics*, 747, 2014.

[26] K. Carlberg, M. Barone, and H. Antil. Galerkin v. least-squares Petrov–Galerkin projection in nonlinear model reduction. *Journal of Computational Physics*, 330:693–734, 2017.

[27] M. Cevheri and T. Stoesser. Large-eddy simulation of a jet in crossflow using local mesh refinement. *Progress in Computational Fluid Dynamics, an International Journal*, 18(3):137–149, 2018.

[28] Y. J. Chan, M. F. Chong, C. L. Law, and D. Hassell. A review on anaerobic–aerobic treatment of industrial and municipal wastewater. *Chemical Engineering Journal*, 155(1-2):1–18, 2009.

[29] E. P. Chassignet, C. Cenedese, and J. Verron. *Buoyancy-driven flows*. Cambridge University Press, 2012.

[30] B. Chen, B. Fraga, and H. Hemida. Large-Eddy Simulation of Enhanced Mixing with Buoyant Plumes. *Chemical Engineering Research and Design*, 2021.

[31] S. Chen and G. D. Doolen. Lattice Boltzmann method for fluid flows. *Annual review of fluid mechanics*, 30(1):329–364, 1998.

[32] R. P. Chhabra and J. F. Richardson. *Non-Newtonian flow and applied rheology: engineering applications*. Butterworth-Heinemann, 2011.

[33] Y.-J. Chou, S.-H. Gu, and Y.-C. Shao. An Euler–Lagrange model for simulating fine particle suspension in liquid flows. *Journal of Computational Physics*, 299:955–973, 2015.

[34] R. Ciuryło and J. Szudy. Speed-dependent pressure broadening and shift in the soft collision approximation. *Journal of Quantitative Spectroscopy and Radiative Transfer*, 57(3):411–423, 1997.

[35] G. Constantinescu. LES of lock-exchange compositional gravity currents: a brief review of some recent results. *Environmental Fluid Mechanics*, 14(2):295–317, 2014.

[36] A. J. Crespo, J. M. Domínguez, B. D. Rogers, M. Gómez-Gesteira, S. Longshaw, R. Canelas, R. Vacondio, A. Barreiro, and O. García-Feal. DualSPHysics: Open-source parallel CFD solver based on Smoothed Particle Hydrodynamics (SPH). *Computer Physics Communications*, 187:204–216, 2015.

[37] C. Crowe, M. Sommerfeld, Y. Tsuji, et al. *Multiphase Flows with.* Ž, 1998.

[38] C. T. Crowe, M. P. Sharma, and D. E. Stock. The particle-source-in cell (PSI-CELL) model for gas-droplet flows. 1977.

[39] P. A. Cundall and O. D. Strack. A discrete numerical model for granular assemblies. *geotechnique*, 29(1):47–65, 1979.

[40] W. B. Dade and H. E. Huppert. A box model for non-entraining, suspension-driven gravity surges on horizontal surfaces. *Sedimentology*, 42(3):453–470, 1995.

[41] D. Dapelo, F. Alberini, and J. Bridgeman. Euler-Lagrange CFD modelling of unconfined gas mixing in anaerobic digestion. *Water research*, 85:497–511, 2015.

[42] D. Dapelo and J. Bridgeman. Euler-Lagrange Computational Fluid Dynamics simulation of a full-scale unconfined anaerobic digester for wastewater sludge treatment. *Advances in Engineering Software*, 117:153–169, 2018.

[43] D. Darmana, N. Deen, and J. Kuipers. Detailed modeling of hydrodynamics, mass transfer and chemical reactions in a bubble column using a discrete bubble model. *Chemical engineering science*, 60(12):3383–3404, 2005.

[44] A. W. Date. *Introduction to computational fluid dynamics*. Cambridge university press, 2005.

[45] F. De Rooij and S. Dalziel. Time-and space-resolved measurements of deposition under turbidity currents. *Particulate gravity currents*, pages 207–215, 2001.

[46] N. G. Deen, M. van Sint Annaland, and J. Kuipers. Multi-scale modeling of dispersed gas–liquid two-phase flow. *Chemical engineering science*, 59(8-9):1853–1861, 2004.

[47] M. Dhotre, N. Deen, B. Niceno, Z. Khan, and J. Joshi. Large eddy simulation for dispersed bubbly flows: a review. *International Journal of Chemical Engineering*, 2013, 2013.

[48] M. T. Dhotre, B. Niceno, B. L. Smith, and M. Simiano. Large-eddy simulation (LES) of the large scale bubble plume. *Chemical Engineering Science*, 64(11):2692–2704, 2009.

[49] K. Ekambara and J. Joshi. CFD simulation of mixing and dispersion in bubble columns. *Chemical engineering research and design*, 81(8):987–1002, 2003.

[50] S. Elghobashi. On predicting particle-laden turbulent flows. *Applied scientific research*, 52(4):309–329, 1994.

[51] N. Eshtiaghi, F. Markis, S. D. Yap, J.-C. Baudez, and P. Slatter. Rheological characterisation of municipal sludge: a review. *Water research*, 47(15):5493–5510, 2013.

[52] L. Espath, L. Pinto, S. Laizet, and J. Silvestrini. High-fidelity simulations of the lobe-and-cleft structures and the deposition map in particle-driven gravity currents. *Physics of Fluids*, 27(5):056604, 2015.

[53] A. Fabregat, W. K. Dewar, T. M. Özgökmen, A. C. Poje, and N. Wienders. Numerical simulations of turbulent thermal, bubble and hybrid plumes. *Ocean Modelling*, 90:16–28, 2015.

[54] F. Fernández, M. Castro, M. Rodrigo, and P. Cañizares. Reduction of aeration costs by tuning a multi-set point on/off controller: A case study. *Control Engineering Practice*, 19(10):1231–1237, 2011.

[55] J. Ferry and S. Balachandar. A fast Eulerian method for disperse two-phase flow. *International journal of multiphase flow*, 27(7):1199–1226, 2001.

[56] J. H. Ferziger, M. Perić, and R. L. Street. *Computational methods for fluid dynamics*, volume 3. Springer, 2002.

[57] C. F. Forster. The rheological and physico-chemical characteristics of sewage sludges. *Enzyme and Microbial Technology*, 30(3):340–345, 2002.

[58] C. F. Forster. *Wastewater treatment and technology*. Thomas Telford, 2003.

[59] B. Fraga and T. Stoesser. Influence of bubble size, diffuser width, and flow rate on the integral behavior of bubble plumes. *Journal of Geophysical Research: Oceans*, 121(6):3887–3904, 2016.

[60] B. Fraga, T. Stoesser, C. C. Lai, and S. A. Socolofsky. A LES-based Eulerian–Lagrangian approach to predict the dynamics of bubble plumes. *Ocean modelling*, 97:27–36, 2016.

[61] E. Francisco, L. Espath, S. Laizet, J. Silvestrini, and V. M. Calo. Direct numerical simulations of intrusive density-and particle-driven gravity currents. *Physics of Fluids*, 34(4):045116, 2022.

[62] E. P. Francisco, L. Espath, and J. Silvestrini. Direct numerical simulation of bidisperse particle-laden gravity currents in the channel configuration. *Applied Mathematical Modelling*, 49:739–752, 2017.

[63] L. Fu. A low-dissipation finite-volume method based on a new TENO shock-capturing scheme. *Computer Physics Communications*, 235:25–39, 2019.

[64] J.-C. Gabelle, F. Augier, A. Carvalho, R. Rousset, and J. Morchain. Effect of tank size on kLa and mixing time in aerated stirred reactors with non-newtonian fluids. *The Canadian Journal of Chemical Engineering*, 89(5):1139–1153, 2011.

[65] L. Gemello, V. Cappello, F. Augier, D. Marchisio, and C. Plais. CFD-based scale-up of hydrodynamics and mixing in bubble columns. *Chemical Engineering Research and Design*, 136:846–858, 2018.

[66] A. N. Georgoulas, P. B. Angelidis, T. G. Panagiotidis, and N. E. Kotsovinos. 3D numerical modelling of turbidity currents. *Environmental fluid mechanics*, 10(6):603–635, 2010.

[67] C. Gladstone, J. Phillips, and R. Sparks. Experiments on bidisperse, constant-volume gravity currents: propagation and sediment deposition. *Sedimentology*, 45(5):833–843, 1998.

[68] C. Gladstone and A. W. Woods. On the application of box models to particle-driven gravity currents. *Journal of fluid mechanics*, 416:187–195, 2000.

[69] M. Gresch, M. Armbruster, D. Braun, and W. Gujer. Effects of aeration patterns on the flow field in wastewater aeration tanks. *Water research*, 45(2):810–818, 2011.

[70] C. Gualtieri, A. Angeloudis, F. Bombardelli, S. Jha, and T. Stoesser. On

the values for the turbulent Schmidt number in environmental flows. *Fluids*, 2(2):17, 2017.

[71] T. C. Harris, A. J. Hogg, and H. E. Huppert. Polydisperse particle-driven gravity currents. *Journal of Fluid Mechanics*, 472:333–371, 2002.

[72] L. He and D. Tafti. Variation of drag, lift and torque in a suspension of ellipsoidal particles. *Powder Technology*, 335:409–426, 2018.

[73] L. He and D. K. Tafti. A supervised machine learning approach for predicting variable drag forces on spherical particles in suspension. *Powder technology*, 345:379–389, 2019.

[74] X. He and L.-S. Luo. Theory of the lattice Boltzmann method: From the Boltzmann equation to the lattice Boltzmann equation. *Physical review E*, 56(6):6811, 1997.

[75] B. Hoomans, J. Kuipers, W. J. Briels, and W. P. M. van Swaaij. Discrete particle simulation of bubble and slug formation in a two-dimensional gas-fluidised bed: a hard-sphere approach. *Chemical Engineering Science*, 51(1):99–118, 1996.

[76] J. Horwitz and A. Mani. Accurate calculation of Stokes drag for point–particle tracking in two-way coupled flows. *Journal of Computational Physics*, 318:85–109, 2016.

[77] D. Hryb, M. Cardozo, S. Ferro, and M. Goldschmit. Particle transport in turbulent flow using both Lagrangian and Eulerian formulations. *International Communications in Heat and Mass Transfer*, 36(5):451–457, 2009.

[78] G. Hu and I. Celik. Eulerian–Lagrangian based large-eddy simulation of a partially aerated flat bubble column. *Chemical Engineering Science*, 63(1):253–271, 2008.

[79] Y. Huang, C. Yang, C. Wen, and G. Wen. S-type dissolved oxygen distribution along water depth in a canyon-shaped and algae blooming water source reservoir: reasons and control. *International journal of environmental research and public health*, 16(6):987, 2019.

[80] H. E. Huppert and J. E. Simpson. The slumping of gravity currents. *Journal of Fluid Mechanics*, 99(4):785–799, 1980.

[81] R. Inghilesi, C. Adduce, V. Lombardi, F. Roman, and V. Armenio. Axisymmetric three-dimensional gravity currents generated by lock exchange. *Journal of Fluid Mechanics*, 851:507–544, 2018.

[82] A. M. Karpinska and J. Bridgeman. CFD-aided modelling of activated sludge systems–A critical review. *Water research*, 88:861–879, 2016.

[83] A. M. Karpinska and J. Bridgeman. Towards a robust CFD model for aeration tanks for sewage treatment–a lab-scale study. *Engineering Applications of Computational Fluid Mechanics*, 11(1):371–395, 2017.

[84] A. M. Karpinska, M. M. Dias, R. A. Boaventura, and R. J. Santos. Modeling of the hydrodynamics and energy expenditure of oxidation ditch aerated with hydrojets using CFD codes. *Water Quality Research Journal of Canada*, 50(1):83–94, 2015.

[85] A. Kartushinsky, S. Tisler, J. G. Oliveira, and C. Van der Geld. Eulerian-Eulerian modelling of particle-laden two-phase flow. *Powder Technology*, 301:999–1007, 2016.

[86] A. R. Khojasteh, S. Laizet, D. Heitz, and Y. Yang. Lagrangian and Eulerian dataset of the wake downstream of a smooth cylinder at a Reynolds number equal to 3900. *Data in brief*, 40:107725, 2022.

[87] D. Kim, D.-I. Kim, J.-H. Kim, and T. Stoesser. Large eddy simulation of flow and tracer transport in multichamber ozone contactors. *Journal of Environmental Engineering*, 136(1):22–31, 2010.

[88] C. Lai, B. Fraga, W. Chan, and M. Dodd. Energy cascade in a homogeneous swarm of bubbles rising in a vertical channel. *Proceedings of the Summmer Program*, 2018.

[89] S. Laizet, S. Lardeau, and E. Lamballais. Direct numerical simulation of a mixing layer downstream a thick splitter plate. *Physics of Fluids*, 22(1):015104, 2010.

[90] S. Laizet and N. Li. Incompact3d: A powerful tool to tackle turbulence problems with up to O (105) computational cores. *International Journal for Numerical Methods in Fluids*, 67(11):1735–1757, 2011.

[91] S. Laizet and J. C. Vassilicos. DNS of fractal-generated turbulence. *Flow, turbulence and combustion*, 87(4):673–705, 2011.

[92] Y. Le Moullec, C. Gentric, O. Potier, and J. Leclerc. CFD simulation of the hydrodynamics and reactions in an activated sludge channel reactor of wastewater treatment. *Chemical Engineering Science*, 65(1):492–498, 2010.

[93] G. Li, X. Yang, and G. Dai. CFD simulation of effects of the configuration of gas distributors on gas–liquid flow and mixing in a bubble column. *Chemical Engineering Science*, 64(24):5104–5116, 2009.

[94] X.-F. Liang, H. Pan, Y.-H. Su, and Z.-H. Luo. CFD-PBM approach with modified drag model for the gas–liquid flow in a bubble column. *Chemical Engineering Research and Design*, 112:88–102, 2016.

[95] R. Lindken and W. Merzkirch. A novel PIV technique for measurements in

multiphase flows and its application to two-phase bubbly flows. *Experiments in fluids*, 33(6):814–825, 2002.

[96] J. Link, L. Cuypers, N. Deen, and J. Kuipers. Flow regimes in a spout–fluid bed: A combined experimental and simulation study. *Chemical Engineering Science*, 60(13):3425–3442, 2005.

[97] M. C. Lippert and A. W. Woods. Experiments on the sedimentation front in steady particle-driven gravity currents. *Journal of Fluid Mechanics*, 889, 2020.

[98] Y. Liu, J. Du, P. Hu, M. Ma, and D. Hu. Microtopographic modification conserves urban wetland water quality by increasing the dissolved oxygen in the wet season. *Journal of Environmental Sciences*, 87:71–81, 2020.

[99] J. Lu, A. Fernández, and G. Tryggvason. The effect of bubbles on the wall drag in a turbulent channel flow. *Physics of Fluids*, 17(9):095102, 2005.

[100] B. Magolan, N. Lubchenko, and E. Baglietto. A quantitative and generalized assessment of bubble-induced turbulence models for gas-liquid systems. *Chemical Engineering Science: X*, 2:100009, 2019.

[101] M. Maktabifard, E. Zaborowska, and J. Makinia. Achieving energy neutrality in wastewater treatment plants through energy savings and enhancing renewable energy production. *Reviews in Environmental Science and Bio/Technology*, 17(4):655–689, 2018.

[102] D. Malik and L. Pakzad. Experimental investigation on an aerated mixing vessel through electrical resistance tomography (ERT) and response surface methodology (RSM). *Chemical Engineering Research and Design*, 129:327–343, 2018.

[103] P. Mantz. Cohesionless, fine graded, flaked sediment transport by water. *Nature Physical Science*, 246(149):14–16, 1973.

[104] N. Margenberg, D. Hartmann, C. Lessig, and T. Richter. A neural network multigrid solver for the Navier-Stokes equations. *Journal of Computational Physics*, 460:110983, 2022.

[105] M. Masterov, M. Baltussen, and J. Kuipers. Numerical simulation of a square bubble column using Detached Eddy Simulation and Euler–Lagrange approach. *International Journal of Multiphase Flow*, 107:275–288, 2018.

[106] M. R. Maxey and J. J. Riley. Equation of motion for a small rigid sphere in a nonuniform flow. *The Physics of Fluids*, 26(4):883–889, 1983.

[107] D. D. McClure, N. Aboudha, J. M. Kavanagh, D. F. Fletcher, and G. W. Barton. Mixing in bubble column reactors: experimental study and CFD modeling. *Chemical Engineering Journal*, 264:291–301, 2015.

[108] D. D. McClure, Z. Liu, G. W. Barton, D. F. Fletcher, and J. M. Kavanagh. Oxygen transfer in pilot-scale contactors: An experimental and computational investigation into the effect of contactor design. *Chemical Engineering Journal*, 344:173–183, 2018.

[109] M. Mehrabadi, J. Horwitz, S. Subramaniam, and A. Mani. A direct comparison of particle-resolved and point-particle methods in decaying turbulence. *Journal of Fluid Mechanics*, 850:336–369, 2018.

[110] E. Meiburg, S. Radhakrishnan, and M. Nasr-Azadani. Modeling gravity and turbidity currents: computational approaches and challenges. *Applied Mechanics Reviews*, 67(4), 2015.

[111] R. N. Meroney and P. Colorado. CFD simulation of mechanical draft tube mixing in anaerobic digester tanks. *Water research*, 43(4):1040–1050, 2009.

[112] M. Milelli, B. Smith, and D. Lakehal. Large-eddy simulation of turbulent shear flows laden with bubbles. In *Direct and Large-Eddy Simulation IV*, pages 461–470. Springer, 2001.

[113] L. Morawska, J. W. Tang, W. Bahnfleth, P. M. Bluyssen, A. Boerstra, G. Buonanno, J. Cao, S. Dancer, A. Floto, F. Franchimon, et al. How can airborne transmission of COVID-19 indoors be minimised? *Environment international*, 142:105832, 2020.

[114] M. Motarjemi and G. Jameson. Mass transfer from very small bubbles—the optimum bubble size for aeration. *Chemical Engineering Science*, 33(11):1415–1423, 1978.

[115] M. Nasr-Azadani, B. Hall, and E. Meiburg. Polydisperse turbidity currents propagating over complex topography: comparison of experimental and depth-resolved simulation results. *Computers & Geosciences*, 53:141–153, 2013.

[116] M. Nasr-Azadani and E. Meiburg. Turbidity currents interacting with three-dimensional seafloor topography. *Journal of Fluid Mechanics*, 745:409–443, 2014.

[117] F. Necker, C. Härtel, L. Kleiser, and E. Meiburg. High-resolution simulations of particle-driven gravity currents. *International Journal of Multiphase Flow*, 28(2):279–300, 2002.

[118] F. Necker, C. Härtel, L. Kleiser, and E. Meiburg. Mixing and dissipation in particle-driven gravity currents. *Journal of Fluid Mechanics*, 545:339–372, 2005.

[119] A. W. Nienow, M. F. EDWARDS, and N. Harnby. *Mixing in the process industries*. Butterworth-Heinemann, 1997.

[120] E. Nowobilska-Majewska and P. Bugajski. The Impact of Selected Parameters on the Condition of Activated Sludge in a Biologic Reactor in the Treatment Plant in Nowy Targ, Poland. *Water*, 12(10):2657, 2020.

[121] J. E. Olsen, P. Skjetne, and S. T. Johansen. VLES turbulence model for an Eulerian–Lagrangian modeling concept for bubble plumes. *Applied mathematical modelling*, 44:61–71, 2017.

[122] S. K. Ooi, G. Constantinescu, and L. Weber. Numerical simulations of lock-exchange compositional gravity current. *Journal of Fluid Mechanics*, 635:361–388, 2009.

[123] P. Ouro, B. Fraga, U. Lopez-Novoa, and T. Stoesser. Scalability of an Eulerian-Lagrangian large-eddy simulation solver with hybrid MPI/OpenMP parallelisation. *Computers & Fluids*, 179:123–136, 2019.

[124] P. Ouro, B. Fraga, N. Viti, A. Angeloudis, T. Stoesser, and C. Gualtieri. Instantaneous transport of a passive scalar in a turbulent separated flow. *Environmental Fluid Mechanics*, 18(2):487–513, 2018.

[125] M. D. Patterson, J. Simpson, S. Dalziel, and N. Nikiforakis. Numerical modelling of two-dimensional and axisymmetric gravity currents. *International Journal for Numerical Methods in Fluids*, 47(10-11):1221–1227, 2005.

[126] I. Paul, B. Fraga, M. S. Dodd, and C. Lai. The role of breakup and coalescence in fine-scale bubble-induced turbulence. I. Dynamics. *Physics of Fluids*, 34(8):083321, 2022.

[127] G. Pozzetti and B. Peters. A multiscale DEM-VOF method for the simulation of three-phase flows. *International Journal of Multiphase Flow*, 99:186–204, 2018.

[128] V. Pryamitsyn and V. Ganesan. Mechanisms of steady-shear rheology in polymer-nanoparticle composites. *Journal of Rheology*, 50(5):655–683, 2006.

[129] Y.-X. Ren, H. Zhang, et al. A characteristic-wise hybrid compact-WENO scheme for solving hyperbolic conservation laws. *Journal of Computational Physics*, 192(2):365–386, 2003.

[130] J. Rensink and H. Donker. The effect of contact tank operation on bulking sludge and biosorption processes. *Water Science and Technology*, 23(4-6):857–866, 1991.

[131] L. Rieger, J. Alex, W. Gujer, and H. Siegrist. Modelling of aeration systems at wastewater treatment plants. *Water science and technology*, 53(4-5):439–447, 2006.

[132] W. Rodi, G. Constantinescu, and T. Stoesser. *Large-eddy simulation in hydraulics*. Crc Press London, 2013.

[133] G. Roshani, E. Nazemi, and M. Roshani. Intelligent recognition of gas-oil-water three-phase flow regime and determination of volume fraction using radial basis function. *Flow Measurement and Instrumentation*, 54:39–45, 2017.

[134] J. W. Rottman and J. E. Simpson. Gravity currents produced by instantaneous releases of a heavy fluid in a rectangular channel. *Journal of Fluid Mechanics*, 135:95–110, 1983.

[135] C. Sadino-Riquelme, R. E. Hayes, D. Jeison, and A. Donoso-Bravo. Computational fluid dynamic (CFD) modelling in anaerobic digestion: General application and recent advances. *Critical Reviews in Environmental Science and Technology*, 48(1):39–76, 2018.

[136] B. Sajjadi, A. A. A. Raman, and R. Parthasarathy. Fluid dynamic analysis of non-Newtonian flow behavior of municipal sludge simulant in anaerobic

digesters using submerged, recirculating jets. *Chemical Engineering Journal*, 298:259–270, 2016.

[137] R. Samstag, J. Ducoste, A. Griborio, I. Nopens, D. Batstone, J. Wicks, S. Saunders, E. Wicklein, G. Kenny, and J. Laurent. CFD for wastewater treatment: an overview. *Water Science and Technology*, 74(3):549–563, 2016.

[138] F. Sánchez, H. Rey, A. Viedma, F. Nicolás-Pérez, A. Kaiser, and M. Martínez. CFD simulation of fluid dynamic and biokinetic processes within activated sludge reactors under intermittent aeration regime. *Water research*, 139:47–57, 2018.

[139] M. Sánchez-Monedero, M. Aguilar, R. Fenoll, and A. Roig. Effect of the aeration system on the levels of airborne microorganisms generated at wastewater treatment plants. *Water Research*, 42(14):3739–3744, 2008.

[140] R. Sander. Compilation of Henry's law constants (version 4.0) for water as solvent. *Atmospheric Chemistry and Physics*, 15(8):4399–4981, 2015.

[141] C. Santarelli and J. Fröhlich. Direct numerical simulations of spherical bubbles in vertical turbulent channel flow. *International Journal of Multiphase Flow*, 75:174–193, 2015.

[142] O. E. Sequeiros. Estimating turbidity current conditions from channel morphology: A Froude number approach. *Journal of Geophysical Research: Oceans*, 117(C4), 2012.

[143] M. Shringarpure, M. I. Cantero, and S. Balachandar. Dynamics of complete turbulence suppression in turbidity currents driven by monodisperse suspensions of sediment. *Journal of Fluid Mechanics*, 712:384–417, 2012.

[144] H. Siegrist and M. Tschui. Interpretation of experimental data with regard to the activated sludge model no. 1 and calibration of the model for municipal

wastewater treatment plants. *Water Science and Technology*, 25(6):167–183, 1992.

[145] J. E. Simpson. *Gravity currents: In the environment and the laboratory*. Cambridge university press, 1999.

[146] H. S. Smith. *Oxygen uptake in a completely mixed activated sludge system*. PhD thesis, 1963.

[147] S. A. Socolofsky and E. E. Adams. Liquid volume fluxes in stratified multiphase plumes. *Journal of Hydraulic Engineering*, 129(11):905–914, 2003.

[148] S. A. Socolofsky and E. E. Adams. Role of slip velocity in the behavior of stratified multiphase plumes. *Journal of hydraulic engineering*, 131(4):273–282, 2005.

[149] A. Sokolichin, G. Eigenberger, A. Lapin, and A. Lübert. Dynamic numerical simulation of gas-liquid two-phase flows Euler/Euler versus Euler/Lagrange. *Chemical engineering science*, 52(4):611–626, 1997.

[150] M. Sommerfeld. Numerical methods for dispersed multiphase flows. In *Particles in flows*, pages 327–396. Springer, 2017.

[151] G. Sridhar and J. Katz. Drag and lift forces on microscopic bubbles entrained by a vortex. *Physics of Fluids*, 7(2):389–399, 1995.

[152] M. Terashima, R. Goel, K. Komatsu, H. Yasui, H. Takahashi, Y. Li, and T. Noike. CFD simulation of mixing in anaerobic digesters. *Bioresource technology*, 100(7):2228–2233, 2009.

[153] U. Trottenberg, C. W. Oosterlee, and A. Schuller. *Multigrid*. Elsevier, 2000.

[154] M. Ungarish. *An introduction to gravity currents and intrusions*. CRC press, 2009.

[155] S. O. Unverdi and G. Tryggvason. A front-tracking method for viscous, incompressible, multi-fluid flows. *Journal of computational physics*, 100(1):25–37, 1992.

[156] J. Vila. On particle weighted methods and smooth particle hydrodynamics. *Mathematical models and methods in applied sciences*, 9(02):161–209, 1999.

[157] K. Vui Chua, B. Fraga, T. Stoesser, S. Ho Hong, and T. Sturm. Effect of bridge abutment length on turbulence structure and flow through the opening. *Journal of Hydraulic Engineering*, 145(6):04019024, 2019.

[158] Z. Wang, D. Xiao, F. Fang, R. Govindan, C. C. Pain, and Y. Guo. Model identification of reduced order fluid dynamics systems using deep learning. *International Journal for Numerical Methods in Fluids*, 86(4):255–268, 2018.

[159] P. Wesseling. Introduction to multigrid methods. Technical report, 1995.

[160] B.-M. Wilén and P. Balmér. Short term effects of dissolved oxygen concentration on the turbidity of the supernatant of activated sludge. *Water science and technology*, 38(3):25–33, 1998.

[161] B.-M. Wilén and P. Balmér. The effect of dissolved oxygen concentration on the structure, size and size distribution of activated sludge flocs. *Water Research*, 33(2):391–400, 1999.

[162] B. Wu. CFD prediction of mixing time in anaerobic digesters. *Transactions of the ASABE*, 53(2):553–563, 2010.

[163] B. Wu. CFD simulation of gas and non-Newtonian fluid two-phase flow in anaerobic digesters. *Water research*, 44(13):3861–3874, 2010.

[164] B. Wu. CFD simulation of gas mixing in anaerobic digesters. *Computers and electronics in agriculture*, 109:278–286, 2014.

[165] D. Xiao, F. Fang, C. Pain, and G. Hu. Non-intrusive reduced-order modelling of the Navier–Stokes equations based on RBF interpolation. *International Journal for Numerical Methods in Fluids*, 79(11):580–595, 2015.

[166] H. Xie, J. Yang, Y. Hu, H. Zhang, Y. Yang, K. Zhang, X. Zhu, Y. Li, and C. Yang. Simulation of flow field and sludge settling in a full-scale oxidation ditch by using a two-phase flow CFD model. *Chemical Engineering Science*, 109:296–305, 2014.

[167] X. Yang, X. Zhang, Z. Li, and G.-W. He. A smoothing technique for discrete delta functions with application to immersed boundary method in moving boundary simulations. *Journal of Computational Physics*, 228(20):7821–7836, 2009.

[168] L. Yu, J. Ma, and S. Chen. Numerical simulation of mechanical mixing in high solid anaerobic digester. *Bioresource technology*, 102(2):1012–1018, 2011.

[169] Z. Yujie, L. Mingyan, X. Yonggui, and T. Can. Three-dimensional volume of fluid simulations on bubble formation and dynamics in bubble columns. *Chemical engineering science*, 73:55–78, 2012.

[170] H. Zhang, J. Baeyens, and T. Tan. The bubble-induced mixing in starch-to-ethanol fermenters. *Chemical Engineering Research and Design*, 90(12):2122–2128, 2012.

[171] J. Zhou and S. K. Venayagamoorthy. Impact of ambient stable stratification on gravity currents propagating over a submerged canopy. *Journal of Fluid Mechanics*, 898, 2020.

[172] Z. Zhou, T. Huang, W. Gong, Y. Li, Y. Liu, S. Zhou, and M. Cao. Water Quality Responses during the Continuous Mixing Process and Informed Management of a Stratified Drinking Water Reservoir. *Sustainability*, 11(24):7106, 2019.